Contents

Chapter 1

Introduction

Cerebral circulation in the human being, including the arterial inputs channels to and the venous outflow mechanisms from the skull, plays a key role in the regulation of the brain physiology [15, 33]. It is known from literature that cerebral autoregulation works to maintain blood flow to the brain quite constant at the requested rate, despite pressure changes or structural variation of the basal vasculature [1, 79]. Many biophysical factors affect brain circulation, so that it is difficult to gain a satisfactory understanding of its behavior both for physiological and pathological conditions. Being the proper functioning of brain critically dependent on the values of cerebral blood inflow and outflow [90], it is important to recognize and understand their governing laws.

Within the complex problem of brain physiology, the study of cerebral outflow system is fundamental because it seems to play an important role in the occurence of diseases of the central nervous system [23, 66, 120]. While the current consensus of neurological diseases etiology is autoimmune, a vascular hypothesis, known as chronic cerebrospinal venous insufficiency (CCSVI), has been recently suggested by the research group of the Vascular Diseases Center of the University of Ferrara. This research group for the first time hypothesized an association of CCSVI with neurodegenerative disorders [66, 120]. They postulate that intracranial and extracranial venous structures, coupled with flow abnormalities in the form of reduced or refluxed flow may induce neurological symptoms [97, 118].

Therefore, the interest in understanding the hemodynamics of the brain and its drainage is arising. Unfortunately, experimental access to cerebral circulation dynamics is limited. Indeed, cranial and extracranial veins form an intricate network of vessels (which contains 75% of the body's circulating blood [33]), stressed by complex phenomena involving postural changes and the gravity field, which affect the dynamics of circulating blood [90]. In particular the internal jugular veins (IJVs), which are the dominant outflow vein from the brain [116], are two collapsible vessels characterized by marked changes in their cross sectional area, depending on transmural pressure on the vessel wall [36, 55]. Section changes, in turn, affect their conductance. The overall phenomenon is influenced by the hydrostatic pressure gradient during the transition from the supine to sitting position, and vice versa [7, 21]. Indeed, one of the major regulators of cerebral venous outflow is posture [90, 111]. In the upright position, a hydrostatic gradient exists between the cerebral parenchymal veins and the heart [41]. When a subject lies in the supine position, the absence of any gravitational

gradient causes the blood to be evenly distributed throughout the system. However, when upright, the distribution changes, and approximately 70% of the blood volume becomes located below the diaphragmatic line, due to the action of gravity [33].
It is difficult to gain an accurate quantitative understanding of these biophysical factors, and so of the clinical implications of their alteration to brain circulation. Initial CCSVI research used Doppler ultrasound and catheter venography to quantify flow and visualize vascular anatomy, respectively. Since then, several studies have been conducted in an attempt to validate the initial findings with mixed results. Lack of standardized image modalities, analysis methods, as well as small sample sizes may be the cause for the varied conclusions [46, 92]. Magnetic resonance imaging (MRI), an operator independent imaging method, is generally used to detect lesions in the brain parenchyma to assess neurological diseases. The advantages of MRI, in addition to lesion detection, are the ability to rapidly generate a 3D map of the vasculature using venography, and quantify blood flow in large and small extracranial blood vessels using phase contrast flow quantification. More recently, it has been used to detect vascular and flow abnormalities in the IJV within a subset of patients with neurological diseases [30, 31, 45, 92, 93].
There is a lot of literature that shows comparisons between blood flows in the main drainage ducts, with mixed results about correlation between such flow redistributions and the onset of neurological diseases [71,106,127,130]. Therefore, there is still a lot of research on the field of blood circulation and the diseases associated to CCSVI.
This dissertation presents two results of the scientific work developed by the medical physics group of the University of Ferrara (Department of Physics and Earth Sciences). A new mathematical model for the simulation of cerebral and extracerebral blood circulation is the subject of Chapter 2 and 3, while Chapter 4 and 5 focus on a new device to measure variations of the human circulatory system in different conditions.
Chapter 2 shows how the mathematical model for the study of cerebral and extracerebral flows and pressures is developed [37, 38, 64]. The basic idea is to obtain a simple tool for improving the understanding of a complex system. The main features of the model are that:

- it includes a validated submodel for the simulation of the intracranial circulation and the related autoregulation mechanisms [39, 108, 110];
- it includes a submodel of the cerebral venous outflow system that accounts for the dependence of the hydraulic properties of the IJVs with respect to the gravity field [37, 38, 98];
- it includes a detailed submodel of the main arteries of the human arterial system [64].

The intracranial and venous part of the model (i.e. the 0D part) has been built in collaboration with the Department of Electrical, Electronic and Information Engineering of the University of Bologna (Bologna, Italy), while the arterial 1D part in collaboration with the Institute of Nuclear Physics, Polish Academy of Sciences (Kraków, Poland). These features make it an useful tool for the study of the correlations between extracranial blood redistributions and changes in the intracranial environment. The model is built as a 0D-1D system of differential equations. So, it is composed by a 0D model of the cerebral and brain drainage circulation [37–39, 108, 110] and a comprehensive 1D model of the arterial vasculature [64],

respectively. The intracranial part of the model is an anatomically detailed 0D simulator of the intracranial hemodynamics, which incorporates the autoregulation mechanisms of cerebral blood flow (CBF) [39,108,109]. It is connected to the arterial 1D model and to a second 0D model for the simulation of cerebral drainage pathways, such as IJVs, vertebral, azygos and collateral systems [29, 33, 36, 78, 90, 91, 119]. With the latter, we can simulate some important phenomena affecting the extracranial venous system, such as the posture change or the presence of jugular obstructions (stenosis) [120, 128]. The arterial model consists of a network of transmission lines developed to simulate propagation of the pulse waves in human arteries [64]. Through a system of differential equations, it takes into account the pulse-wave transmission properties of the 55 main arteries, together with the principal hydraulic mechanisms that ensure the proper blood supply of the brain and other organs. Results from the arterial 1D model are used as input to the 0D models to simulate several pressure variations due to periodic perturbations like heartbeat, movements such as cycling, or to the occurence of vascular diseases like tachycardia. The contribution to venous pressure due to respiration is also added to simulate the effect of the thoracic pump on the drainage system.
In Chapter 3 we performed simulations of the effect of posture change from supine to upright on pressures and blood flows, first with basal drainage and then assuming a lack of conductance of some particular vessel tract. In vivo measurements performed in both healthy subjects and individuals with venous obstructions are provided to validate the model (detailed experimental flow data from both healthy and stenotic subjects are available thanks to the cooperation with the MRI Institute for Biomedical Research (Detroit, Michigan), and the Vascular Diseases Center of the University of Ferrara). Indeed, we tuned model parameters to reproduce magnetic resonance and echo-color Doppler data of average blood flow. Results show that the model is able to reproduce the physiological behavior of the IJV, vertebral, and cerebral ducts, with values in good agreement with literature and experimental data. In addition to that, the model is able to give information about flows in different points of the IJV ducts, so taking into account the amount of blood coming from the anastomotic connections. Moreover, we can easily use it to verify how the blood redistribution due to change of posture or changes in the arterial and/or venous system affects the pressures in specific points of the system.
Since the gravitational gradient is the major component to face when considering the physiology of venous return [7, 36, 41, 77, 111], there is a growing interest in understanding how the mechanisms ensuring proper heart filling and circulation change in the absence of gravity. This kind of research is also very important for what concern the arising projects about long term space missions, to ensure safety of astronauts. Indeed, one of the most serious problems produced by microgravity is a fluid shift from lower to upper body. This cephalad fluid shift may change the hemodynamics in the brain [10]. It has been also suggested that venous congestion in the head and neck may contribute to intracranial pressure elevation in microgravity [47]. Drain Brain is a project that aimed to develop a plethysmography device to be used by a crew member during an experiment on the International Space Station. The purpose of the Drain Brain experiment [72], sponsored by the Italian Space Agency, was to monitor the venous return of the astronaut during the space mission, so as to study the compensatory mechanisms that facilitate this essential physiological action in subjects living in a microgravity environment. The knowledge of CBF variations might be used to prevent

astronauts' risk to develop pathologies directly related to physiologic alterations in space. Moreover, the study of CBF in a microgravitational environment can be used to better understand its basic mechanisms and then help earth-based research we are conducting with patients affected by vascular diseases [66, 120]. As said before, there are findings, confirmed by several studies around the world, that neurological diseases could be potentially affected by CCSVI. The development of this novel plethysmography system could then become an ideal screening tool, with immediate benefits to the population.
In Chapter 4 we will describe the electronic device and the experimental protocol we performed during experiments on Earth and in microgravity.
Results of the plethysmography sessions during the preflight, inflight and postflight experiments are presented and discussed in Chapter 5 together with the mathematical tools used for data analysis.

Chapter 2

Mathematical model of cerebral and extracerebral blood circulation

The purpose of this chapter is to describe the new mathematical model for the study of cerebral and extracerebral blood flows and pressures in humans [37, 38].
Such model was developed in collaboration with several scientific groups and research centers. The main idea of the project, together with ultrasound data for experimental validation, arises from the collaboration with the Vascular Diseases Center of the University of Ferrara (Ferrara, Italy). The intracranial and venous part of the model (i.e. the 0D part) has been built in collaboration with the Department of Electrical, Electronic and Information Engineering of the University of Bologna (Bologna, Italy), while the arterial 1D part in collaboration with the Institute of Nuclear Physics, Polish Academy of Sciences (Kraków, Poland). Finally, to validate the model, detailed experimental flow data from both healthy and stenotic subjects are available thanks to the cooperation with the MRI Institute for Biomedical Research (Detroit, Michigan).
Details of the model are presented here, while simulations and comparisons with literature and experimental results are reported in Chapter 3.

2.1 Introduction

There are recent studies concerning the relations among the main cerebral arterial and venous routes, their disorders, and the occurrence of neurological diseases [30, 53, 68, 105, 107, 113]. Due to the complexity of the relationships involved, and the large variability in the anatomical parameters, it is extremely difficult to understand the effect of alterations in the extracranial circulation on brain in simple terms. In general, the study of a real process like cerebral circulation, and of its implications in healthy and diseased conditions, can largely benefit from the use of computational models describing a complex behavior using a system of equations [41, 77, 82]. So far, most models of the cerebral circulation only focused on intracranial segments and related control mechanisms, by providing just a very simplified description of arterial inflow and extracranial venous return.
The aim of the present study is to develop and validate a comprehensive original model of the cerebral and extracerebral inflow and outflow systems. Indeed, this model allows sim-

ulation of the blood flows and pressures in the main vessels and collateral routes of the cerebral and extracerebral circulation. With this model it is possible to study how blood flow changes from supine to upright position, and the correlation among posture variations, vessel conductances (normal or abnormal), muscle movement, heartbeat, and the consequent pressure changes (see Chapter 3 Section 3.3). This may have a great impact toward a deeper understanding of pathological disorders involving abnormalities of the cerebral inflow and outflow. For example, it can be used to easily assess which alterations in the extracranial venous outflow may be in relation with central nervous system disorders [19, 30, 86, 122, 126]. Simulation results are validated by using magnetic resonance imaging (MRI) and echo-color Doppler (ECD) experimental blood flow data in humans (see Chapter 3 Section 3.2).

The present model includes accurate submodels of the arterial tree (Sections 2.3.2 and 2.4.2) and the intracranial circulation (Sections 2.3.1 and 2.4.1), which incorporates the autoregulation of cerebral blood flow (CBF) [39, 108, 110]. They provide a correct value of CBF to the venous part of the model, allowing a quantitative analysis of the effect of alterations in the venous pathways on intracranial quantities, such as intracranial pressure, venous sinuses pressure, capillary pressure, and cerebrospinal fluid (CSF) circulation. A sophisticated description of the collateral pathways, including not only the vertebral plexus but also other anastomoses leading blood to the downstream sections of the jugular veins [19, 105, 122, 127], is also given.

When imaging with the current diagnostic methods multiple stenotic patterns or flow abnormalities in the major extracranial and extraspinal veins, which are typical of chronic cerebrospinal venous insufficiency (CCSVI), it is difficult to confidently assign their hemodynamic significance for the intracranial circulation. It has been recently emphasized that the main issue to be investigated in this field is the definition of the hemodynamic impact in the intracranial venous system of obstruction/narrowing of the extracranial veins [131]. Since, at this time, there is no established invasive or noninvasive diagnostic imaging modality capable to assess intracranial and/or parenchymal circulatory parameters in relation to extracranial brain outflow [132], the clinical application of the present model seems highly desirable. We focused our attention on changes in conductances in the venous pathways. For instance, in the present study we tested our model on four clinical patterns of extracranial venous obstruction, clinically detected in patients by means of catheter venography [120]. Each conductance under examination was varied from the baseline value, that is representative of physiological condition, to zero value that simulates total absence of drainage from a section of the network; simulations of posture variation were performed in both situations. Analysis of the correlation between conductances and posture variation and the subsequent pressures and flows changes might give information about the parameters that have greater impact on intracranial hemodynamics (and then on related disorders). From our particular point of view, analysis of the results before and after the variation of a conductance is meaningful, since it provides information on how the closure of a particular drainage tract affects important physiological parameters, such as venous sinuses pressure P_{vs} (and so intracranial pressure P_{ic} and cerebral circulation).

2.2 Anatomy and physiology of the cerebral drainage system

The part of the venous tree responsible for the brain drainage (see Figure 2.1) represents an important determinant of the intracranial physiology, but its role in the pathology of the central nervous system (CNS) is not fully understood yet [15, 90].

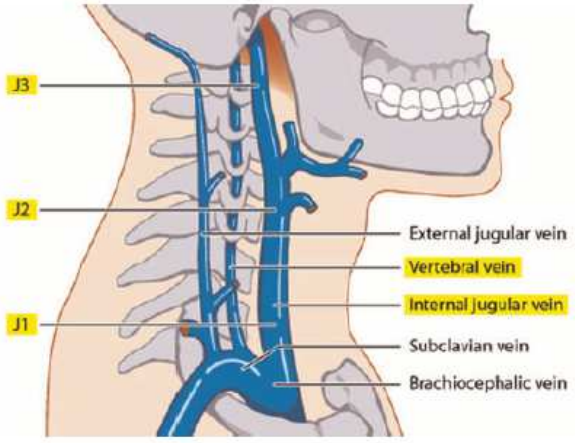

Figure 2.1: Schematic representation of the main vessels of the brain drainage system.

It is recognized that, in supine position, internal jugular veins (IJVs) represent the main outflow route for the cerebral circulation [7, 19, 89, 116, 119], being able to carry most of blood flow from the brain and from other extracerebral territories [91,111,128]. However, the jugular venous system exhibits important flow limitation during upright posture changes, because IJVs tend to collapse as a consequence of the decrease of transmural pressure due to the gravitational field, causing a significant increase in their resistance [14, 21, 36, 41, 90]. Indeed, IJVs are collapsible blood vessels characterized by marked changes in their cross sectional configuration depending on transmural pressure [90] that is affected by hydrostatic pressure gradient during a posture change [21]. In the absence of other routes for extracranial outflow, this flow limitation would have dramatic effects on the cerebral circulation, since, apart from brief transient time intervals, the average cranial arterial inflow is expected to be equal to the cranial venous outflow for the mass conservation. As a consequence, large attention has been devoted to the venous circulation in the upright state, in an effort to understand which alternative routes can carry the brain venous outflow. It has long been postulated that the vertebral venous system may provide an important alternative route for venous outflow when standing or sitting. This was first demonstrated with the use of animals [29] and subsequently measured in humans with the Doppler and MRI technique [7, 19, 21, 89, 111, 119]. Results show that the hydrostatic pressure gradient does not significantly affect the lumen of the vertebral veins.

Accordingly, a classical model of the cerebral venous outflow [41] assumes the existence of two main alternative routes (see Figure 2.1):

- the IJVs, with smaller resistance in supine condition;
- a parallel vertebral route with higher resistance.

In upright condition, when the first route collapses, blood flow is diverted to the second one. As depicted in Figure 2.1, anatomically speaking IJVs are commonly divided in three segments, as recently established by a scientific consensus [123]:

- left and right lower segments (J1) correspond to the point close to the junction of the IJVs with the subclavian vein, at the confluence with the brachiocephalic vein trunk;
- the middle segments (J2) correspond to the point where IJVs are in an anatomical relationship with the more lateral contour of the thyroid gland;
- the upper segments (J3) correspond to the point before the passage through the jugular foramen into the skull.

Such elements collapse according to the tube law [14, 36].
Beside that, other aspects related to IJV and cerebral venous outflow system are still problematic. First of all, cerebral autoregulation maintains blood flow to the brain quite constant, despite pressure changes, as already said [1, 79]. Moreover, using the ECD technique, it is observed that blood flow along IJVs is not longitudinally constant but increases progressively when the measurement site is moved from the upper sections (close to the jugular foramen into the skull, J3) to the downstream sections (close to the subclavian vein, J1) [19, 105, 125, 127]. The first aspect means that the discrepancy in the jugular blood flow (much greater than that measured in the vertebral system) must be carried out in the upright state. This implies that other routes significantly contribute to the orthostatic venous outflow.
The second observation supports the idea that additional anastomotical routes carry part of the cranial blood flow to the IJVs even in upright position, bypassing the upstream more collapsed sections. In fact, as a consequence of the different effect of gravity, only the higher portions of the IJVs are probably fully collapsed, whereas the downstream sections are opened. We are aware of anatomical presence of intra- and extra-cranial connection but their anatomical assessment and physiological contribution to brain circulation is not fully understood yet [119]. All these aspects must be taken into account for a proper modelization of the system.

2.3 Description of the model

The model reproduces physiological behavior of the arterial, cerebral, IJV, and extrajugular ducts in terms of pressures and flows. To do that, it includes a validated 0D submodel for the simulation of the intracranial circulation [39, 108, 110], a validated 0D submodel of the cerebral drainage system that accounts for the dependence of the hydraulic properties of the IJVs with respect to the gravity field [37, 38] (Sections 2.3.1 and 2.4.1), and a validated 1D submodel for the simulation of pulse waves in arteries [64] (Sections 2.3.2 and 2.4.2). In the following the model with its parameters is described.
The model was built starting from the intracranial 0D part, already developed by the Department of Electrical, Electronic and Information Engineering of the University of Bologna (Bologna, Italy) [39, 108, 110]. First, we added to it the jugular and extrajugular drainage pathways to connect brain to vena cava, as depicted in Figure 2.2 [37, 38]. After that, we added the arterial system (thanks to the cooperation with the Institute of Nuclear Physics,

Polish Academy of Sciences (Kraków, Poland) [64] to expand the system in its current form (Figure 2.4).

2.3.1 Description of the 0D submodel (intracranial and venous model)

The hemodynamic model for the intracranial compartment [39,108,110] is represented in the top box (BRAIN) of Figure 2.2.

This part of the model simulates:

- the hemodynamics of the arterial, arteriolar and venous cerebrovascular bed;
- the cerebral arterioles regulation mechanisms;
- the CSF production and reabsorption processes;
- the Starling resistor mechanism for the cerebral veins;
- the nonlinear pressure-volume relationship of the craniospinal compartment.

The conductance of the intracerebral arterioles is subjected to autoregulatory mechanisms, which work to maintain quite a constant cerebral blood flow despite moderate changes in cerebral perfusion pressure [108]. Equations for a proper simulation of mechanisms such as cerebrospinal circulation and cerebral veins behavior are also inserted in the model. Details of all the parameters and how they are connected to save mass conservation at all the nodes of the circuit, together with all the equations and how they are linked to extracranial parts of the model are reported in Section 2.4.

Cerebral venous system plays an important role within the system that regulate cerebral hemodynamics. However, it is difficult to deal with modeling of extracranial network of veins that drains head and brain, because this vascular tree is quite intricate, and stressed by several phenomena involving respiration, postural changes and the gravity field. These phenomena deeply act on the dynamics of blood flowing toward the heart [33,90]. The venous model [37,38] (represented as IJV, vertebral, and azygos blocks in Figure 2.2) is able to:

- simulate the average pressures and flows in different points of the IJV and extrajugular ducts;
- take into account the amount of blood coming from the anastomotic connections;
- simulate how the blood redistribution due to change of posture affects flows and pressures in specific points of the system;
- simulate redistributions due to stenotic patterns.

Cerebral blood flow Q is the total blood volume entering the cranial cavity per unit time. At the exit from the skull, it is drained by IJV, vertebral and collateral veins, with IJVs that contribute to drain the main part of blood only in supine position. Therefore, the main part of the model is composed of two venous ducts to simulate left and right IJV. Such veins are the main outflow vessels from the brain [116]. They are modeled by dividing them into three segments (J3, J2, and J1, starting from the upper segment, see Figure 2.1) [123] with different

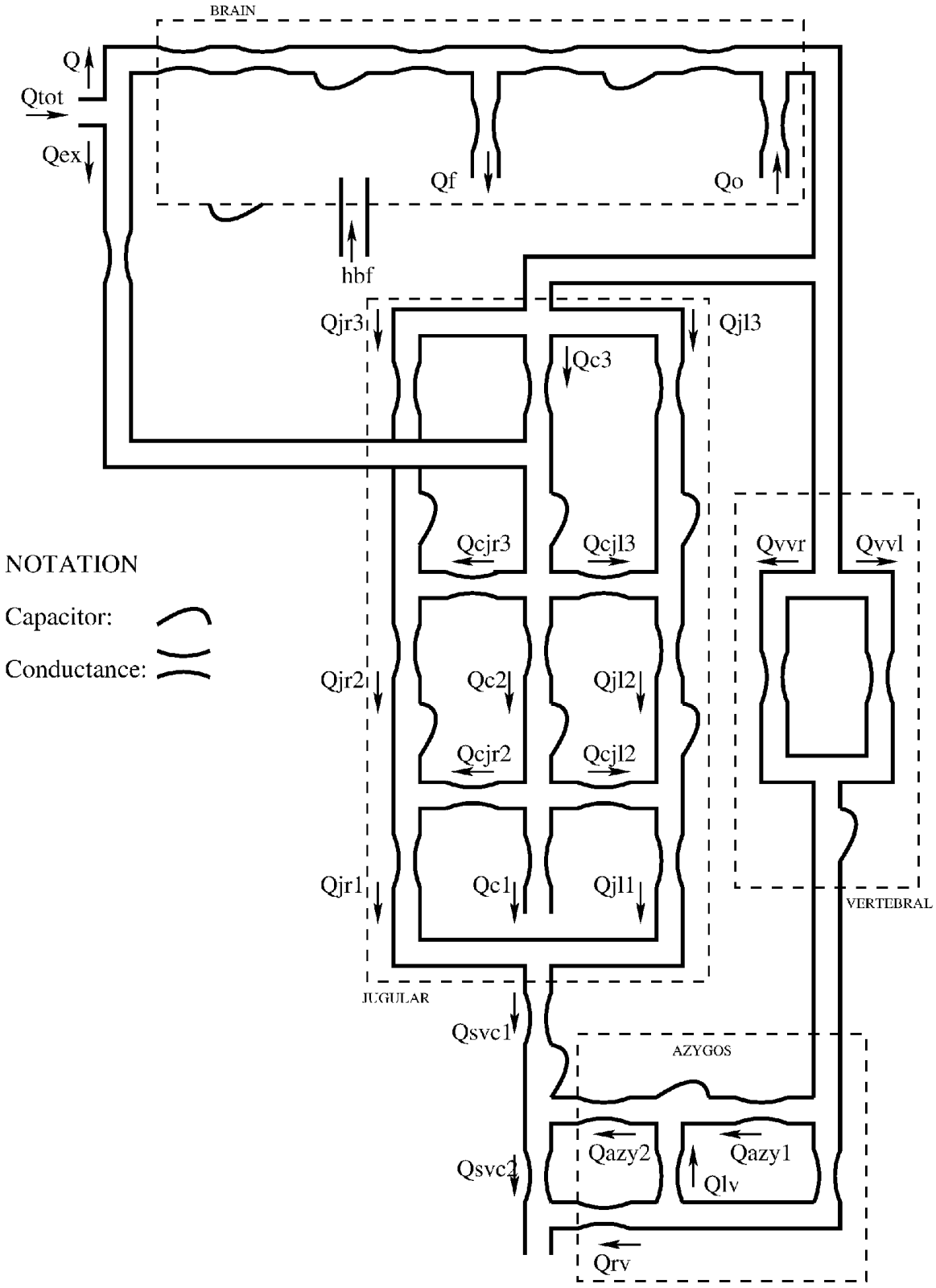

Figure 2.2: Scheme of the hemodynamic parameter model for the study of cerebral venous outflow [37, 38]. Box on the top part (BRAIN) is the submodel for the intracranial circulation [39, 108, 110]. Out of the BRAIN box the 0D submodel for the cerebral drainage system is depicted.

conductive and capacitive values, to better implement the different biomechanical properties of these vessels along their length and to better simulate the effect of hydrostatic pressure gradient in upright position [37]. Transmural pressure easily acts on cross sectional area of collapsible tubes, and so on conductances. Hydrostatic pressure gradient acts on transmural pressure of the collapsible veins of the neck changing the hydraulic properties of the vessels from the supine to sitting position [7, 21]. Indeed, the biomechanical properties of the IJVs change along their lengths, because in the upright position they act like collapsible tubes interacting with the hydrostatic pressure gradient. This phenomenon must not be neglected in a solid and detailed model of the cerebral circulation. Therefore, they are modeled as collapsible vessels with conductances that are deeply affected by transmural pressure on the vessels wall [7, 21, 36, 55].

Moreover, for a complete model it is necessary to take into account the other drainage routes beside the IJVs, like verterbral and collateral pathways, that lead blood out of the brain when conductances of IJVs decreases after postural changes or onset of venous obstructions. These alternative routes (supposed to not suffer the hydrostatic pressure gradient and so to not vary the conductance with posture changes) drain venous flow from the brain into IJVs with several connections called anastomoses, or directly to vena cava [19,105,125,127]. To account for the growth of blood flow from J3 to J1 [19, 26, 30, 105, 111, 125, 127], we must consider that a quota of the head inflow is conveyed into the IJVs more caudally with respect to the J3 position, through intra- and extracranial anastomosis. To account for this experimental evidence, the model is developed so that the two jugular veins are linked by a network of eight constant conductances and two constant capacitors that simulate the presence of collaterals and anastomotic connections. The segmentation of IJVs also makes the model a good tool to easily simulate differences on blood redistribution on the left and right sides (there is experimental evidence that blood flow is not the same in the right and left part of the jugular system) [19, 120, 127]. This collateral network also allows the drainage of the extracranial venous blood, i.e., of that part of blood coming from the two external arteries to serve the head organs and tissues out of the braincase [127]. Moreover, a basic submodel of six constant conductances and three constant capacitors is implemented in the main model to describe the lumbo-azygos system, which links jugular and vertebral pathways at the level of superior vena cava [116].

Respiration is the other major effect involved on brain drainage. The thoracic pump [125] produces an additional periodic variation on venous conductances and compliances that is accounted in the model. To simulate effects due to respiration we make use of the following pressure profile as input to the pressure P_{cv} [57,60,81], i.e. at the end of the venous pathway (Figure 2.3).

2.3.2 Description of the 1D submodel (arterial model)

The hemodynamic model for the simulation of the arterial compartment [64] is represented in the left part of Figure 2.4, where the current version of the system (comprehensive of both 1D arterial and 0D intracranial and venous submodels) is depicted.

One dimensional modeling of the blood flow in deformable vessels has proven to be a simple and effective approach to simulations of the hemodynamics in the larger arteries of the body [13, 49].

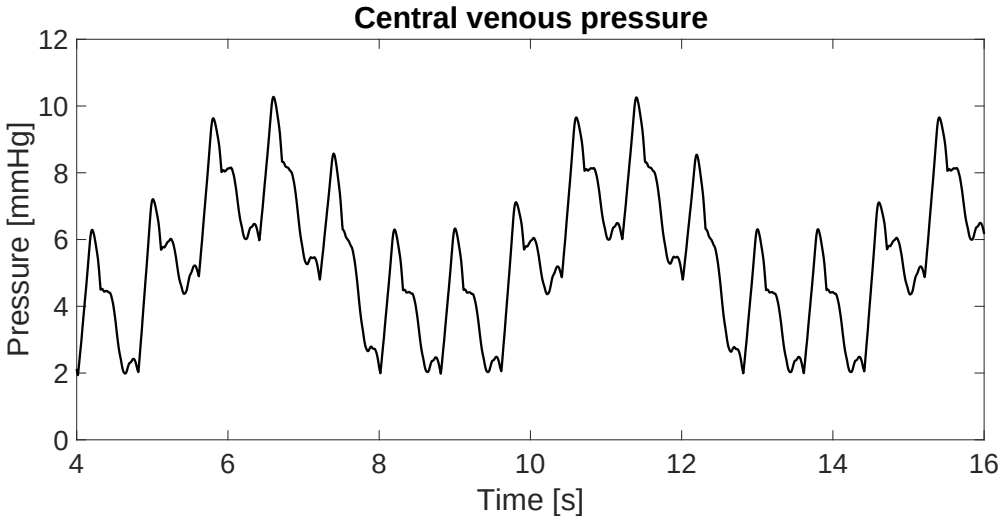

Figure 2.3: Pressure profile of the central venous pressure P_{cv} (simulation of two complete respiratory cycles are reported). The duration time of one respiratory cycle is 4.8 s, corresponding to six heart beats with no tachycardiac effects.

An anatomically detailed model consisting of a network of electric transmission lines is used here to simulate propagation of the pulse waves in humans. It is a new numerical simulation method that allows one to predict the time dependence (waveform) of pressure at any location of the arterial system in humans [64]. This kind of models are particularly effective in the description of large scale properties of the entire arterial system and of its response to some lesions and/or external hazards. Starting from experimental data collected at rest [6], the 1D model can simulate blood pressure during rest and exercise condition, changes in the heart rate, basal properties of left ventricle valve and its disfunctions.
The input data include the geometry and the elastic properties of the arteries as well as the rheological parameters of blood [74]. Thus, the method can account for individual anatomic details of the subject examined. In its simplest realization the model involves lengths and topology of the arterial segments as well as the propagation parameters: the phase velocity and the characteristic impedance of each segment. This allows the reflection and transmission coeffcients to be calculated at each bifurcation [2, 87]. The elasticity of vessel walls is at the origin of the wave-like character of blood flow in arteries. In principle the number of propagation modes is infinite [28, 51], but the most significant effect belongs to the Young mode easily palpable at wrist. Restricting the attention to this mode allows one to treat the vessels as monomode 1D waveguides.
From our purposes, we need to properly reproduce the arterial pressure in external, internal and vertebral arteries so that to give such pressures as input to braincase and head circulation. To simulate heart rate we make use of the pressure profile in the left ventricle depicted in Figure 2.5.

The duration of every heartbeat is 0.8 s, while minimum and maximum pressure are 27.0 and 60.7 mmHg, respectively. Boundary conditions to the propagation of this disturbance are the geometrical and mechanical properties of the vessel tree and the presence of the aortic valve.
Literature data about geometrical and mechanical properties of the arterial ducts are used to calculate all the necessary parameters to close the system of differential equations (see Table

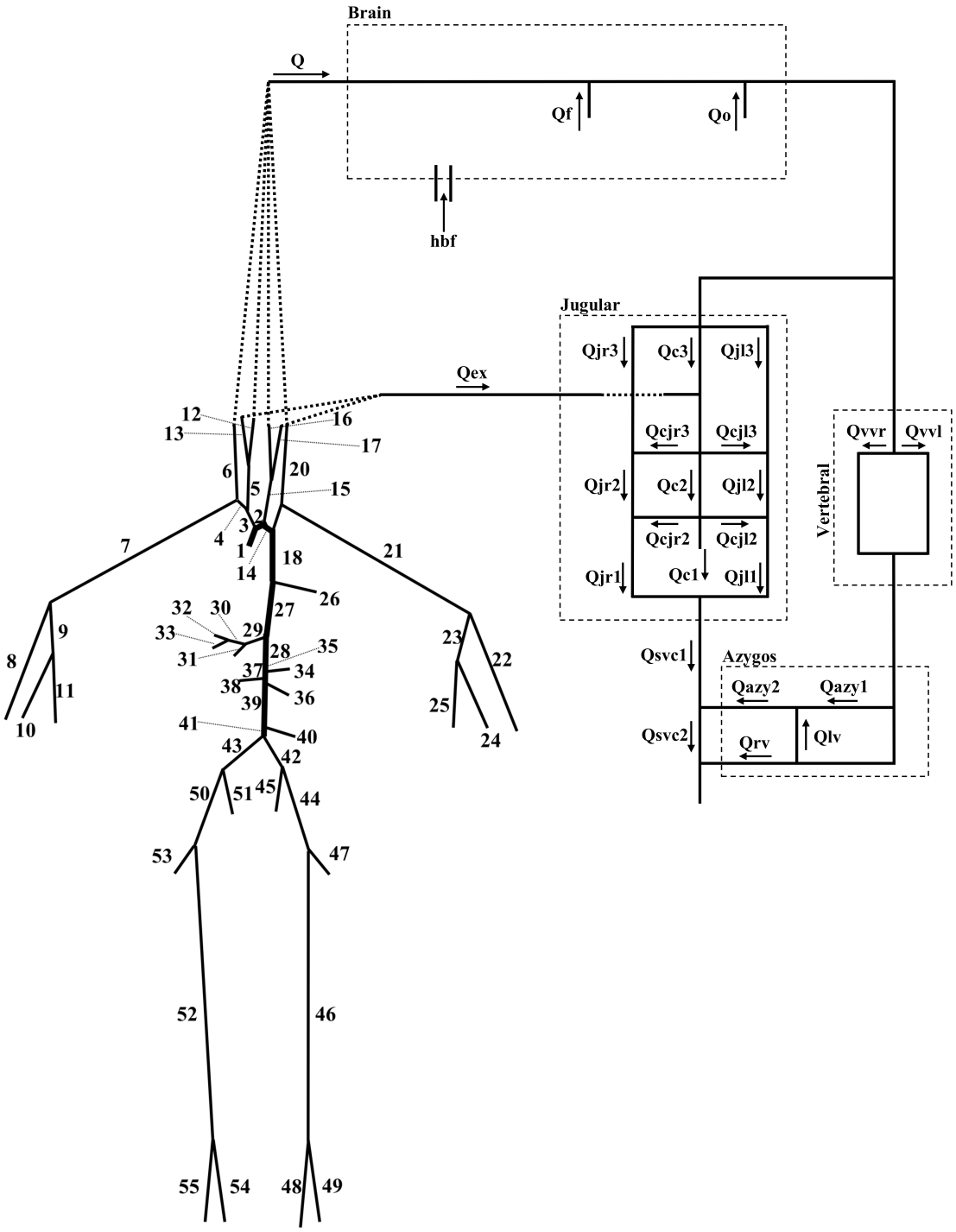

Figure 2.4: Mathematical model for the study of the cerebral and extracerebral circulation. Box on the top part is the scheme of the intracranial 0D submodel. Right part is the representation of the 0D submodel for the cerebral drainage system, while in the left part the 1D submodel for the human arterial tree is depicted.

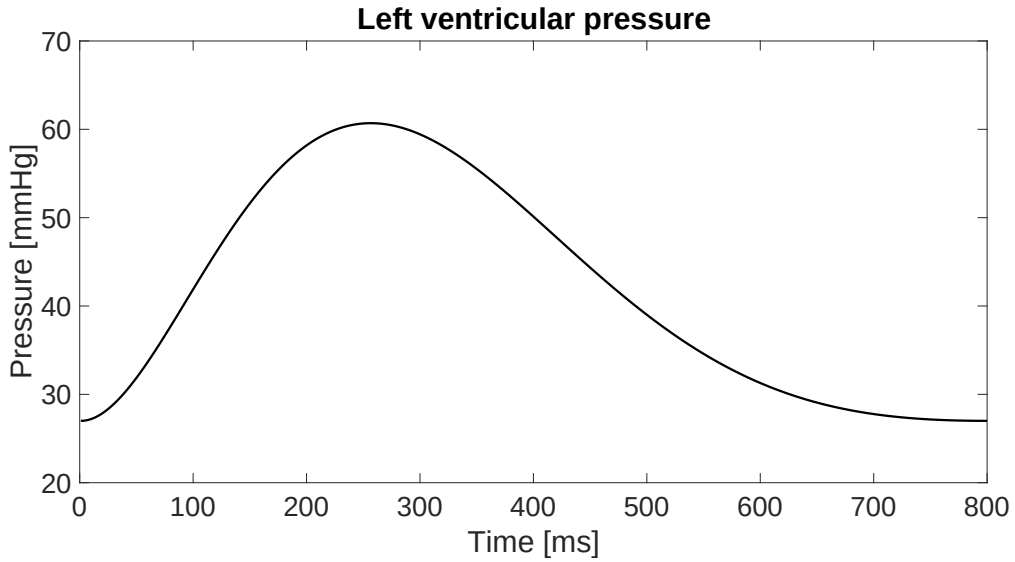

Figure 2.5: Pressure waveform at the level of left ventricle. The duration time is 800 ms, minimum pressure is 27.0 mmHg (at $t = 0$ ms), while maximum pressure is 60.7 mmHg (at $t = 257$ ms) [74].

2.8). A time dependent reflection coefficient, R_v, is defined to simulate the aortic valve. We have $R_v > 1$ (more pressure is reflected than it comes in) when the aortic valve is open and $R_v = 1$ (total reflection) when it is closed [4] (Figure 2.6).

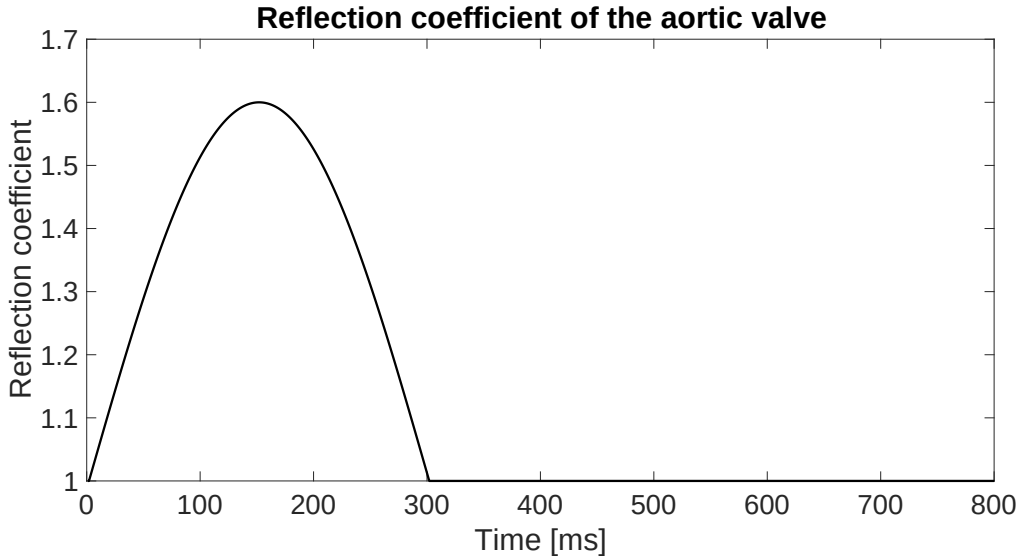

Figure 2.6: Reflection coefficient of the heart valve. The duration time is 800 ms, with $R_v > 1$ from $t = 0$ ms to $t = 301$ ms (maximum value $R_v = 1.6$ at $t = 152$ ms) and $R_v = 1$ from $t = 302$ ms to $t = 800$ ms.

Pressure waveform at the level of left ventricle is then transmitted throughout all the arterial tree and produces pressure oscillations in all the segments. We are interested in the pressure behavior of left and right vertebral artery (segment 20 and 6 of Figure 2.4), left and right internal carotid artery (segment 16 and 12) and left and right external carotid artery (segment 17 and 13). Vertebral arteries supply blood to the upper spinal cord, brainstem, cerebellum, and posterior part of brain. Internal carotid arteries arise from the common carotid arteries where these bifurcate into the internal and external carotid arteries at cervical vertebral level 3 or 4. The internal carotid arteries supply the brain, while the external carotid

arteries supply portions of the head, such as face, scalp, skull, and meninges [33, 44, 78]. We use the sum of pressures carried by vertebral and internal carotid arteries as input to the 0D intracranial model (arterial pressure P_a), and sum of pressures carried by external carotid arteries as input to the extracerebral duct (external pressure P_{ex}). These pressures are the basic arterial inputs to the brain and venous part of the model, i.e. to the 0D model.
In addition to that, we choose to simulate cycling exercise and tachycardia. To simulate effects due to legs exercise (cycling) we choose to alternatively produce the pressure profile of Figure 2.7 at the level of segment 44 (left external iliac artery) simultaneous to 52 (right femoral artery), and segment 50 (right external iliac artery) simultaneous to 46 (left femoral artery), as extra input of the arterial model.

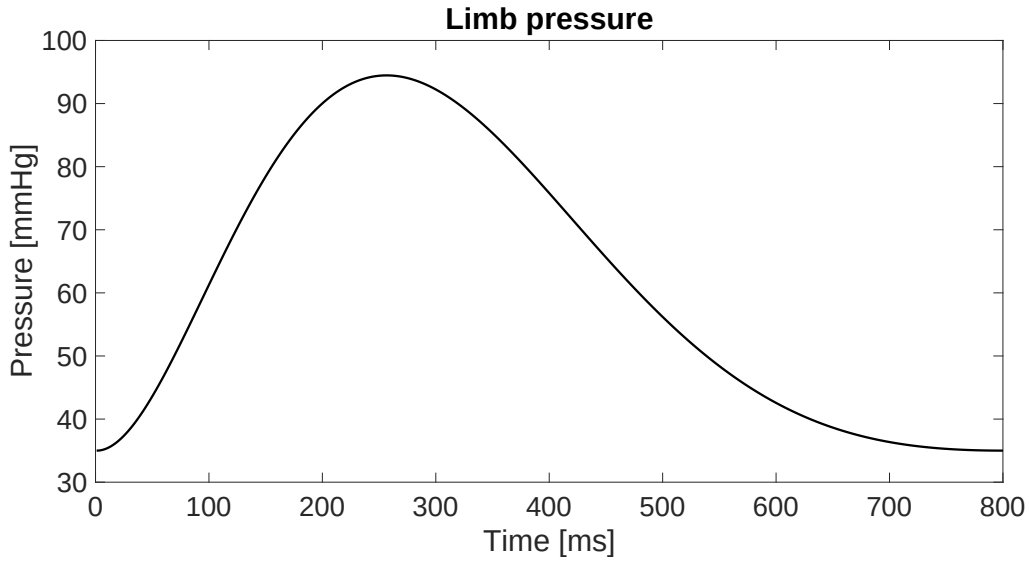

Figure 2.7: Pressure waveform at the level of legs (segment 44 and 46 for the left leg, and 50 and 52 for the right leg) to simulate cycling exercise. The duration time is 800 ms, minimum pressure is 35.0 mmHg (at $t = 0$ ms), while maximum pressure is 94.5 mmHg (at $t = 257$ ms).

To simulate effects due to tachycardia we make use of the same pressure profile in the left ventricle depicted in Figure 2.5, but with double frequency (i.e. the duration time of one heartbeat is 400 ms).

2.4 Equations of the model

The model is made up of several differential equations. We adjusted every parameter value in search of agreement between model simulations and measurements that can be obtained from experimental or literature results. All the model equations are presented in the following.

2.4.1 Equations of the 0D submodel (intracranial and venous system of equations)

For what concern the cerebral and venous submodels, every equation links together the elements representative of a specific point x (i.e., pressure P_x, conductance G_x, and capacity C_x) with the elements representative of the other segments of the system to account for mass

conservation and to include effects due to posture changes [7,21,36,55]. We refer to resistance of a given tract R_x as the inverse of the conductance G_x of the same tract. Table 2.1 provides a glossary of terms.

The mathematical model of the cerebral hemodynamics has been fully developed and validated [39, 108, 110]. It simulates the hemodynamics of the arteriovenous cerebrovascular bed and the related mechanisms [90], such as:

- regulation activity of cerebral arterioles;
- CSF production and reabsorption processes;
- Starling resistor mechanism for the cerebral veins.

A thorough justification of all the parameters concerning the intracranial circulation can be found in literature [108, 110]. Briefly, intracranial vascular resistances and capacities were assigned on the basis of physiological and anatomical data on brain hemodynamics in a normal subject. The autoregulation gain and time constants were given to simulate the typical autoregulation response of an healthy individual who exhibits mild CBF changes despite cerebral perfusion pressure changes (see Figure 2.8).

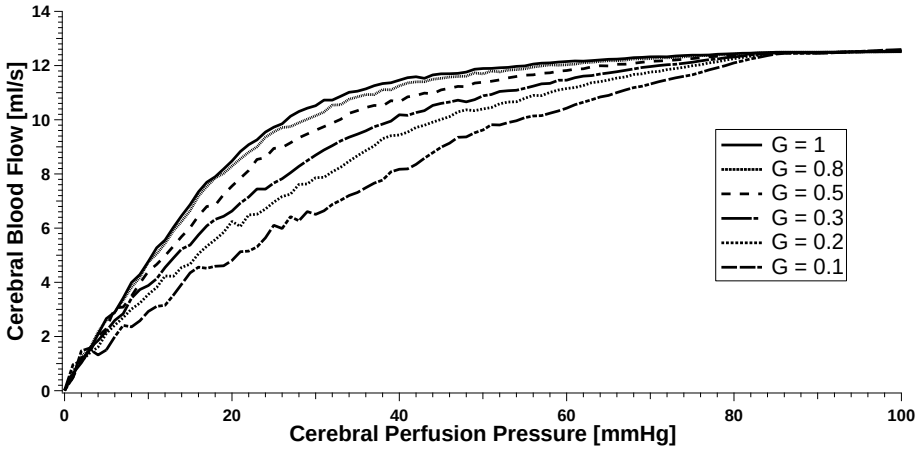

Figure 2.8: Curves of the cerebral blood flow vs. cerebral perfusion pressure for maximum ($G_{aut} = 1$) and progressive impaired autoregulation gain.

Parameters summarizing the CSF circulation and intracranial compliance were set to establish a normal hydrodynamics, as derived from infusion tests in the neurological literature. All the intracranial basal parameters are summarized in Table 2.2.

Mathematical equations for intracranial blood dynamics and CSF circulation have been written by imposing the mass conservation principle at all the circuit nodes. Mass conservation at the node of pial arterioles *pa* implies the following equation:

$$\frac{d\left(P_{pa} - P_{ic}\right)}{dt} = \frac{1}{C_{pa}}\left[\frac{P_a - P_{pa}}{R_{la} + R_{pa}/2} - \frac{P_{pa} - P_c}{R_{pa}/2} - \frac{dC_{pa}}{dt}\left(P_{pa} - P_{ic}\right)\right] \tag{2.1}$$

Capillary pressure P_c is given by:

$$P_c = \left(\frac{P_v}{R_{pv}} + \frac{P_{pa}}{R_{pa}/2} + \frac{P_{ic}}{R_f}\right) / \left(\frac{1}{R_{pv}} + \frac{1}{R_{pa}/2} + \frac{1}{R_f}\right) \tag{2.2}$$

Table 2.1: Glossary of terms related to the 0D part of the model.

Symbol	*Quantity*
A	Parameter related to the resistance of the jugular segments to collapse
AZY	Lumbo-azygos system
$azy1$	Distal azygos
$azy2$	Proximal azygos
$c3$	Upper segment of the collateral network
CBF	Cerebral blood flow
$cj2$	Lower anastomoses
$cj3$	Upper anastomoses
C_{azy}	Capacity of the azygos system
C_{c2}	Capacity of the middle segment of the collateral network
C_{c3}	Capacity of the upper segment of the collateral network
C_{ic}	Intracranial capacity
C_{jl2}	Capacity of the middle segment of the left internal jugular vein
C_{jl3}	Capacity of the upper segment of the left internal jugular vein
C_{jr2}	Capacity of the middle segment of the right internal jugular vein
C_{jr3}	Capacity of the upper segment of the right internal jugular vein
C_{pa}	Capacity of the pial arterioles
C_{pan}	Basal capacity of the pial arterioles
CSF	Cerebrospinal fluid
C_{svc}	Capacity of the superior vena cava
C_{vi}	Capacity of the intracranial veins
C_{vs}	Capacity of the terminal intracranial veins
C_{vv}	Capacity of the vertebral veins
C_x	Capacity of the generic segment x of the circulatory system
ΔC_{pa}	Amplitude of the curve of the pial arterioles capacity
ΔC_{pa1}	Value of the capacity of the pial arterioles during vasodilation simulation
ΔC_{pa2}	Value of the capacity of the pial arterioles during vasoconstriction simulation
g	Gravity acceleration
G_0	Conductance of the cerebrospinal fluid outflow tract
G_{aut}	Gain of the autoregulation mechanism related to CBF variations
G_{azy1}	Conductance of the distal azygos
G_{azy2}	Conductance of the proximal azygos
G_{c1}	Conductance of the lower segment of the collateral network
G_{c2}	Conductance of the middle segment of the collateral network
G_{c3}	Conductance of the upper segment of the collateral network
G_{cjl2}	Conductance of the lower anastomotic connection (left side)
G_{cjl3}	Conductance of the upper anastomotic connection (left side)
G_{cjr2}	Conductance of the lower anastomotic connection (right side)
G_{cjr3}	Conductance of the upper anastomotic connection (right side)
G_{ex}	Conductance of the external carotid arteries
G_{jl1}	Conductance of the lower segment of the left internal jugular vein
G_{jl2}	Conductance of the middle segment of the left internal jugular vein
G_{jl3}	Conductance of the upper segment of the left internal jugular vein
G_{jr1}	Conductance of the lower segment of the right internal jugular vein
G_{jr2}	Conductance of the middle segment of the right internal jugular vein
G_{jr3}	Conductance of the upper segment of the right internal jugular vein
G_{lv}	Conductance of the lumbar vein
G_{svc1}	Conductance of the upper segment of the superior vena cava (jugular confluence)
G_{svc2}	Conductance of the lower segment of the superior vena cava
G_{vs}	Conductance of the terminal intracranial veins
G_{vv2}	Conductance of the lower part of the vertebral vein
G_{vvl}	Conductance of the left vertebral vein
G_{vvr}	Conductance of the right vertebral vein
G_x	Conductance of the generic segment x of the circulatory system
h	Length of a jugular segment
hbf	Mock cerebrospinal fluid possibly injected into or subtracted from the cranial cavity
IJV	Internal jugular vein
$J1$	Lower segment of the internal jugular veins
$J2$	Middle segment of the internal jugular veins
$J3$	Upper segment of the internal jugular veins
$jr3$	Upper segment of the right jugular vein
kC_{pa}	Parameter for the capacity of the pial arterioles
k_E	Intracranial elastance coefficient
k_{jl1}	Parameter for the basal conductance of the lower segment of the left internal jugular vein
k_{jl2}	Parameter for the basal conductance of the middle segment of the left internal jugular vein
k_{jl3}	Parameter for the basal conductance of the upper segment of the left internal jugular vein
k_{jr1}	Parameter for the basal conductance of the lower segment of the right internal jugular vein
k_{jr2}	Parameter for the basal conductance of the middle segment of the right internal jugular vein

k_{jr3}	Parameter for the basal conductance of the upper segment of the right internal jugular vein
k_R	Parameter for the resistance of pial arterioles
k_{ven}	Parameter for the intracranial venous capacity
k_x	Parameter for the basal conductance of internal jugular and vertebral veins
pa	Pial arterioles
P_a	Arterial pressure
P_{azy}	Pressure in the azygos system
P_c	Pressure in the intracranial capillaries
P_{c2}	Pressure in the middle segment of the collateral network
P_{c3}	Pressure in the upper segment of the collateral network
P_{cv}	Pressure in the vena cava
P_{ic}	Intracranial pressure
P_{icn}	Basal intracranial pressure
P_{j1ext}	Pressure outside the lower segment of the internal jugular veins
P_{j2ext}	Pressure outside the middle segment of the internal jugular veins
P_{j3ext}	Pressure outside the upper segment of the internal jugular veins
P_{jl2}	Pressure in the middle segment of the left internal jugular vein
P_{jl3}	Pressure in the upper segment of the left internal jugular vein
P_{jr2}	Pressure in the middle segment of the right internal jugular vein
P_{jr3}	Pressure in the upper segment of the right internal jugular vein
P_{lv}	Pressure in the lumbar vein
P_{pa}	Pressure in the pial arterioles
P_{svc}	Pressure in the lower segment of the superior vena cava
P_{svc1}	Pressure in the upper segment of the superior vena cava (jugular confluence)
P_v	Pressure in the cerebral veins
P_{v1}	Transmural pressure value at which cerebral veins collapse
P_{vs}	Pressure in the venous sinuses
P_{vv}	Pressure in the vertebral veins
P_x	Pressure in the generic segment x of the internal jugular veins
P_{xext}	External pressure of the x segment of the internal jugular veins
P_{xint}	Internal pressure of the x segment of the internal jugular veins
Q	Cerebral blood flow
Q_0	Cerebrospinal fluid outflow rate
Q_{azy1}	Flow in the distal azygos
Q_{c1}	Flow in the lower segment of the collateral network
Q_{c2}	Flow in the middle segment of the collateral network
Q_{c3}	Flow in the upper segment of the collateral network
Q_{cjl2}	Flow in the lower anastomotic connection (left side)
Q_{cjl3}	Flow in the upper anastomotic connection (left side)
Q_{cjr2}	Flow in the lower anastomotic connection (right side)
Q_{cjr3}	Flow in the upper anastomotic connection (right side)
Q_{ex}	Flow in the external carotid arteries (flow to face and neck)
Q_f	Cerebrospinal fluid formation rate
Q_{j1}	Total flow in the lower segments of the internal jugular veins
Q_{j2}	Total flow in the middle segments of the internal jugular veins
Q_{j3}	Total flow in the upper segments of the internal jugular veins
Q_{jl1}	Flow in the lower segment of the left internal jugular vein
Q_{jl2}	Flow in the middle segment of the left internal jugular vein
Q_{jl3}	Flow in the upper segment of the left internal jugular vein
Q_{jr1}	Flow in the lower segment of the right internal jugular vein
Q_{jr2}	Flow in the middle segment of the right internal jugular vein
Q_{jr3}	Flow in the upper segment of the right internal jugular vein
Q_{lv}	Flow in the lumbar vein
Q_n	Basal cerebral blood flow
Q_{rv}	Flow in the renal vein
Q_{svc1}	Flow in the upper segment of the superior vena cava (jugular confluence)
Q_{tot}	Total inflow
Q_{totout}	Total outflow
Q_{vv}	Total flow in the vertebral veins
Q_{vvl}	Flow in the left vertebral vein
Q_{vvr}	Flow in the right vertebral vein
R_0	Resistance to the cerebrospinal fluid outflow
R_f	Resistance to the cerebrospinal fluid formation
R_x	Resistance of the generic segment x of the circulatory system
ρ	Blood density
R_{la}	Resistance of the basal intracranial arteries
R_{pa}	Resistance of the pial arterioles
R_{pv}	Resistance of the proximal intracranial veins
R_{vs}	Resistance of the terminal intracranial veins
R_{vs1}	Terminal intracranial vein resistance when P_{ic} is equal to P_{vs}
t	Time

τ_{aut}	Time constant of the autoregulation mechanism related to cerebral flow variations
vi	Cerebral veins
VV	Vertebral vein
x	Generic segment of the circuit
x_{aut}	State variable of the autoregulation mechanism related to cerebral flow variations

Table 2.2: Basal values of quantities related to the intracranial circuit (supine condition).

Quantity	*Value*
C_{pan}	$0.205\ mlmmHg^{-1}$
ΔC_{pa1}	$2.87\ mlmmHg^{-1}$
ΔC_{pa2}	$0.164\ mlmmHg^{-1}$
G_{aut}	3
k_E	$0.077\ ml^{-1}$
k_R	$13.1 \cdot 10^3\ mmHg^3sml^{-1}$
k_{ven}	$0.155\ ml^{-1}$
P_a	$100\ mmHg$
P_{icn}	$9.5\ mmHg$
P_{pa}	$58.9\ mmHg$
P_v	$14.1\ mmHg$
P_{v1}	$-2.5\ mmHg$
P_{vs}	$6\ mmHg$
Q_n	$12.5\ mls^{-1}$
R_0	$526.3\ mmHgsml^{-1}$
R_f	$2.38 \cdot 10^3\ mmHgsml^{-1}$
R_{la}	$0.6\ mmHgsml^{-1}$
R_{pv}	$0.880\ mmHgsml^{-1}$
R_{vs1}	$0.366\ mmHgsml^{-1}$
τ_{aut}	$20\ s$
x_{aut}	$2.16 \cdot 10^{-4}$

The left term of Equation 2.1 is the variation of transmural pressure in time at the node of pial arterioles. It depends on the blood flow entering and leaving the node (the first 2 terms in the brackets at the right side) and on the active changes in arterial capacity C_{pa} over time (the last term in brackets). The value of C_{pa} at the denominator accounts for the ability of the duct to store blood without variations of transmural pressure: the higher the value of C_{pa} the lower the change in pressure over time. All other mass conservation equations have a similar meaning.

Mass conservation at the node of cerebral veins vi implies the following equation:

$$\frac{d\left(P_v - P_{ic}\right)}{dt} = \frac{1}{C_{vi}}\left[\frac{P_c - P_v}{R_{pv}} - \frac{P_v - P_{vs}}{R_{vs}}\right] \tag{2.3}$$

The relationship between C_{vi} and pressure is given by the following equation:

$$C_{vi} = \frac{1}{k_{ven}\left(P_v - P_{ic} - P_{v1}\right)} \tag{2.4}$$

Control mechanisms work at the level of the arteriolar cerebrovascular bed by modifying R_{pa} and C_{pa}. Autoregulation activated by relative changes in Q is given by the following equation:

$$\frac{dx_{aut}}{dt} = \left(\frac{1}{\tau_{aut}}\right)\left[-x_{aut} + G_{aut}\left(\frac{Q - Q_n}{Q_n}\right)\right] \tag{2.5}$$

where the minus sign of x_{aut} simulates the fact that a fall in blood flow causes a rapid dilatation of resistance vessels, whereas a rise in blood pressure causes vasoconstriction.

The existence of maximal limits for the vascular response (total vasodilation and maximal vasoconstriction) is simulated by a sigmoidal relationship with upper and lower saturation

levels acting on pial arteries capacity C_{pa}, so that:

$$C_{pa} = \frac{\left(C_{pan} - \frac{\Delta C_{pa}}{2}\right) + \left(C_{pan} + \frac{\Delta C_{pa}}{2}\right) exp\left[\frac{-x_{aut}}{kC_{pa}}\right]}{1 + exp\left[\frac{-x_{aut}}{kC_{pa}}\right]} \tag{2.6}$$

The sigmoidal curve cannot be symmetrical because the increase in blood volume induced by vasodilation is higher than the blood volume decrease induced by vasoconstriction. Hence, two different values must be chosen for the parameter ΔCpa, depending on whether vasodilation or vasoconstriction is considered. We have

$$if\ x_{aut} < 0\ then\ \Delta C_{pa} = \Delta C_{pa1}\ and\ kC_{pa} = \Delta C_{pa1}/4 \tag{2.7}$$

for the vasodilation simulation, and

$$if\ x_{aut} > 0\ then\ \Delta C_{pa} = \Delta C_{pa2}\ and\ kC_{pa} = \Delta C_{pa2}/4 \tag{2.8}$$

for the vasoconstriction simulation.
The value of pial arterioral resistance is given by the formula:

$$R_{pa} = \frac{k_R C_{pan}^2}{\left[\left(P_{pa} - P_{ic}\right) C_{pa}\right]^2} \tag{2.9}$$

The following equations account for cerebrospinal fluid formation rate Q_f and outflow rate Q_0

$$Q_f = \frac{P_c - P_{ic}}{R_f}\ if\ P_c > P_{ic},\ else\ Q_f = 0 \tag{2.10}$$

$$Q_0 = \frac{P_{ic} - P_{vs}}{R_0}\ if\ P_{ic} > P_{vs},\ else\ Q_0 = 0 \tag{2.11}$$

An expression for the resistance of the terminal intracranial veins R_{vs} is computed as follows:

$$R_{vs} = \frac{P_v - P_{vs}}{P_v - P_{ic}} R_{vs1}\ if\ P_v > P_{vs},\ else\ R_{vs} = R_{vs1} \tag{2.12}$$

Application of mass conservation at the intracranial volume leads to the following equations:

$$\frac{dP_{ic}}{dt} = \frac{1}{C_{ic}}\left[\frac{d\left(P_{pa} - P_{ic}\right)}{dt} C_{pa} + \frac{d\left(P_v - P_{ic}\right)}{dt} C_{vi} + \frac{dC_{pa}}{dt}\left(P_{pa} - P_{ic}\right) + Q_f - Q_0 + hbf\right] \tag{2.13}$$

and

$$C_{ic} = \frac{1}{k_E P_{ic}} \tag{2.14}$$

This formula states that the variation in time of the intracranial pressure is the result of several factors. The first and the second term in brackets at the right side of Equation 2.13 refer to changes in transmural pressure at the level of arterioles and cerebral veins, the third term refers to change on pial artery capacity, while the other terms refer to CSF inflow or

outflow. Intracranial capacity C_{ic} at the denominator accounts for the ability of the skull to store volume.
The structure of the cerebral venous outflow model has been developed starting from a recent work [127]. It is build by using two types of equations. Equations from 2.15 to 2.24 are the state equations of the model and implement the mass conservation at all the circuit nodes. We can see how the pressure at a given point (e.g. $jr3$ in Equation 2.16) is related to capacity, conductances, and drops of pressure.

$$\begin{aligned}\frac{dP_{vs}}{dt} = \frac{1}{C_{vs}}[&(P_v - P_{vs})\,G_{vs} - (P_{vs} - P_{ic})\,G_0 - (P_{vs} - P_{jr3})\,G_{jr3} - (P_{vs} - P_{jl3})\,G_{jl3} \\ &- (P_{vs} - P_{c3})\,G_{c3} - (P_{vs} - P_{vv})\,G_{vvl} - (P_{vs} - P_{vv})\,G_{vvr}]\end{aligned} \tag{2.15}$$

$$\frac{dP_{jr3}}{dt} = \frac{1}{C_{jr3}}\left[(P_{vs} - P_{jr3})\,G_{jr3} - (P_{jr3} - P_{c3})\,G_{cjr3} - (P_{jr3} - P_{jr2})\,G_{jr2}\right] \tag{2.16}$$

$$\frac{dP_{jr2}}{dt} = \frac{1}{C_{jr2}}\left[(P_{jr3} - P_{jr2})\,G_{jr2} - (P_{jr2} - P_{c2})\,G_{cjr2} - (P_{jr2} - P_{svc1})\,G_{jr1}\right] \tag{2.17}$$

$$\frac{dP_{jl3}}{dt} = \frac{1}{C_{jl3}}\left[(P_{vs} - P_{jl3})\,G_{jl3} - (P_{jl3} - P_{c3})\,G_{cjl3} - (P_{jl3} - P_{jl2})\,G_{jl2}\right] \tag{2.18}$$

$$\frac{dP_{jl2}}{dt} = \frac{1}{C_{jl2}}\left[(P_{jl3} - P_{jl2})\,G_{jl2} - (P_{jl2} - P_{c2})\,G_{cjl2} - (P_{jl2} - P_{svc1})\,G_{jl1}\right] \tag{2.19}$$

$$\begin{aligned}\frac{dP_{c3}}{dt} = \frac{1}{C_{c3}}[&(P_{vs} - P_{c3})\,G_{c3} + (P_{jr3} - P_{c3})\,G_{cjr3} + (P_{jl3} - P_{c3})\,G_{cjl3} + (P_a - P_{c3})\,G_{ex} \\ &- (P_{c3} - P_{c2})\,G_{c2}]\end{aligned} \tag{2.20}$$

$$\frac{dP_{c2}}{dt} = \frac{1}{C_{c2}}[(P_{c3} - P_{c2})\,G_{c2} + (P_{jr2} - P_{c2})\,G_{cjr2} + (P_{jl2} - P_{c2})\,G_{cjl2} - (P_{c2} - P_{cv})\,G_{c1}] \tag{2.21}$$

$$\frac{dP_{svc}}{dt} = \frac{1}{C_{svc}}\left[(P_{svc1} - P_{svc})\,G_{svc1} + (P_{azy} - P_{svc})\,G_{azy2} - (P_{svc} - P_{cv})\,G_{svc2}\right] \tag{2.22}$$

$$\frac{dP_{vv}}{dt} = \frac{1}{C_{vv}}[(P_{vs} - P_{vv})\, G_{vvl} + (P_{vs} - P_{vv})\, G_{vvr} - (P_{vv} - P_{azy})\, G_{azy1} - (P_{vv} - P_{lv})\, G_{vv2}] \tag{2.23}$$

$$\frac{dP_{azy}}{dt} = \frac{1}{C_{azy}}\left[(P_{vv} - P_{azy})\, G_{azy1} + (P_{lv} - P_{azy})\, G_{lv} - (P_{azy} - P_{svc})\, G_{azy2}\right] \tag{2.24}$$

To include dynamics due to posture changes from supine to upright in the gravity field, conductances in the IJVs are modeled using a nonlinear relation (Equation from 2.25 to 2.30) with switch-like properties so that for negative or low transmural pressure $P_{xint} - P_{xext}$ at a given point x, the related vessel conductance G_x is low, while for high transmural pressure, vessel conductance approaches a maximum value [41].

$$G_{jr3} = k_{jr3}\left[1 + \left(\frac{2}{\pi}\right) arctan\left(\frac{P_{vs} - P_{j3ext}}{A}\right)\right]^2 \tag{2.25}$$

$$G_{jl3} = k_{jl3}\left[1 + \left(\frac{2}{\pi}\right) arctan\left(\frac{P_{vs} - P_{j3ext}}{A}\right)\right]^2 \tag{2.26}$$

$$G_{jr2} = k_{jr2}\left[1 + \left(\frac{2}{\pi}\right) arctan\left(\frac{P_{jr3} - P_{j2ext}}{A}\right)\right]^2 \tag{2.27}$$

$$G_{jl2} = k_{jl2}\left[1 + \left(\frac{2}{\pi}\right) arctan\left(\frac{P_{jl3} - P_{j2ext}}{A}\right)\right]^2 \tag{2.28}$$

$$G_{jr1} = k_{jr1}\left[1 + \left(\frac{2}{\pi}\right) arctan\left(\frac{P_{jr2} - P_{j1ext}}{A}\right)\right]^2 \tag{2.29}$$

$$G_{jl1} = k_{jl1}\left[1 + \left(\frac{2}{\pi}\right) arctan\left(\frac{P_{jl2} - P_{j1ext}}{A}\right)\right]^2 \tag{2.30}$$

Starting from the work on the intracranial circuit [108], we moved around several experimental data to choose the right inputs for the jugular-extrajugular network, adopting reasonable criteria to determine parameters not available from literature. The values of all conductances in the extracranial circulation (reported in Table 2.3) were assigned starting from physiological values of pressures (Table 2.4) to reproduce the supine average flows and supine to upright percentage flow variations in each portion of the model (Tables 2.5 and 2.6, see Section 3.2 for experimental details).

Conductances that must be changed to reproduce differences among normal and stenotic subjects are listed in Table 2.3 part A, while unchanged conductances are listed in Table 2.3, part B.

Table 2.5 summarizes the calculated average blood flows Q, Q_{ex}, Q_{jr3}, Q_{jl3}, Q_{jr2}, Q_{jl2}, and Q_{vv}, with corresponding standard deviations (SDs), for every subgroup.

Average blood flows Q, Q_{j3}, Q_{j2}, Q_{j1}, and Q_{vv} of 10 NST volunteers, measured by using the ECD technique, are reported in Table 2.6 with corresponding SDs.

Table 2.3: List of the conductance values to reproduce the average flow data reported in Table 2.5 and the flow percentage variations reported in Table 2.6.

$G\ [mls^{-1}mmHg^{-1}]$	NST	LL-R ST	UL-L ST
A)			
G_{vv1}	0.60	3.90	7.70
k_{jl3}	6.00	6.00	0.86
k_{jr2}	16.00	2.30	16.00
B)			
G_{c2}	11.00		
G_{c3}	21.43		
G_{cjl2}	6.67		
G_{cjl3}	16.00		
G_{azy1}	1.33		
G_{azy2}	1.78		
G_{c1}	1.18		
G_{cjr2}	6.67		
G_{cjr3}	21.00		
G_{ex}	0.03		
G_{lv}	0.89		
G_{rv}	0.41		
G_{svc1}	78.50		
G_{svc2}	81.17		
G_{vv2}	0.83		
k_{jl1}	7.27		
k_{jl2}	8.00		
k_{jr1}	7.27		
k_{jr3}	13.00		

Table 2.4: Basal values of pressures related to the jugular-vertebral circuit (supine condition).

Pressure	*Symbol*	*Value* $[mmHg]$
At the collateral (superior tract)	P_{c3}	6.00
At the right IJV (superior tract)	P_{jr3}	5.85
At the left IJV (superior tract)	P_{jl3}	5.85
At the collateral (middle tract)	P_{c2}	5.85
At the vertebral vein	P_{vv}	5.80
At the right IJV (middle tract)	P_{jr2}	5.70
At the left IJV (middle tract)	P_{jl2}	5.70
At the azygos vein	P_{azy}	5.50
At the superior vena cava (superior tract)	P_{svc1}	5.40
At the superior vena cava (inferior tract)	P_{svc}	5.20
At the right atrium (central venous pressure)	P_{cv}	5.00
External at J3 and J2	P_{xext}	0
External at J1	P_{xext}	-6.50

Table 2.5: MRI average data of flows related to cerebral, external, IJV, and vertebral circuits in the supine condition. Flow values are reported in ml/s with SDs.

MRI	n	Q	Q_{ex}	Q_{jr3}	Q_{jl3}	Q_{jr2}	Q_{jl2}	Q_{vv}
NST	38	10.6 ± 1.6	2.8 ± 1.2	5.6 ± 2.1	3.1 ± 1.8	7.1 ± 2.4	4.4 ± 1.9	0.5 ± 0.6
LL-R ST	20	10.7 ± 1.8	3.0 ± 1.1	3.5 ± 2.5	4.0 ± 2.1	3.6 ± 2.7	4.7 ± 2.6	1.8 ± 1.6
UL-L ST	49	10.6 ± 1.8	3.2 ± 1.2	6.1 ± 2.5	0.8 ± 0.9	7.5 ± 2.1	2.1 ± 1.7	2.0 ± 1.6

Table 2.6: ECD average data of flow related to cerebral, IJV, and vertebral circuits in the NST condition. Flow values are reported in ml/s with SDs.

ECD	Q	Q_{j3}	Q_{j2}	Q_{j1}	Q_{vv}
Supine	10.6 ± 1.9	6.0 ± 2.6	8.9 ± 3.4	22.0 ± 10.3	1.1 ± 0.7
Upright	10.6 ± 1.9	4.1 ± 2.0	5.2 ± 3.3	20.4 ± 12.5	2.3 ± 1.2
Variation (%)	0	-32	-42	-7	109

The absolute values reported in Table 2.6 may be affected by a proportional error, typical of the ECD technique, when moving from one tract to the next. Hence, we focused attention only on the percentage variations within each column. The supine to upright percentage variations detected with the ECD technique reported in Table 2.6 were used to assign conductance to the anastomoses not directly involved in supine conditions. As shown in Table 2.4, we assumed a progressive pressure reduction from the venous sinuses to the right atrium (i.e., the central venous pressure), assuming normal values as large as 6 and 5 mmHg, respectively. Typical average values reported in Table 2.4 are assigned as basal values to the pressure of the superior tract of collateral P_{c3}, of venous sinuses pressure P_{vs} [108], and of central venous pressure P_{cv} [41]. Intermediate basal pressure values (P_{jr3}, P_{jr2}, etc ...) are assigned to simulate a homogeneous pressure drop along the whole circuit from the exit of venous sinuses to the vena cava. External pressure P_{xext} to the upper sections of the jugular veins J3 and J2 is set to zero, while at the lower segments J1 is set to the average thoracic pressure during a complete respiratory cycle [65].
Looking at the basal flows shown in Table 2.5, cerebral blood flow Q is the total blood volume entering the cranial cavity per unit time. At the exit from the skull, it is drained by jugular, vertebral and collateral veins, with the two IJVs that contribute to drain the main part of blood only in supine position (see Section 2.2). Q_{ex} is the flow through left and right external carotid arteries. Part of it is directed to every IJV via the anastomotic connections, while the remaining blood is drained down through the middle collateral. Finally, part of the vertebral flow enters in the azygos vein, while the remaining is divided between lumbar and renal vein duct.
The values of the capacities in the extracranial circulation (Table 2.7) have been determined using the following considerations:

- capacities in the IJV tracts and in the vertebral veins have been computed from the values of transmural pressures, lengths, and areas reported in the literature [111] and assuming a negligible unstressed volume;

- capacity of the azygos veins are assumed comparable to the capacity of the vertebral veins;

- capacities of the collateral tracts have been computed, in the absence of clear geometrical data, by assuming that they are approximately proportional to the square root of conductances and using the capacities of the IJV tracts as a reference;

- a small value has been given to the capacity of the venous sinuses, since most of these vessels are surrounded by the dura mater;

- we checked that, with the previous choices, the overall capacity of the venous outflow circulation is close to the value reported in literature [109] for the capacity of the cerebral venous vascular bed (10.7 ml/mmHg).

To complete the determination of model parameters, we need to assign a value to A and k_x in the equations describing the conductance of the IJVs (Equation from 2.25 to 2.30). These values have been given to address two major requirements:

Table 2.7: Capacities related to the jugular-vertebral circuit (supine condition).

Capacity	*Symbol*	$Value\ [mlmmHg^{-1}]$
At the venous sinuses	C_{vs}	0.5
At the right internal jugular (superior tract)	C_{jr3}	1.0
At the left internal jugular (superior tract)	C_{jl3}	1.0
At the right internal jugular (middle tract)	C_{jr2}	2.5
At the left internal jugular (middle tract)	C_{jl2}	2.5
At the central collateral (superior tract)	C_{c3}	0.7
At the central collateral (middle tract)	C_{c2}	1.4
At the superior vena cava (lower tract)	C_{svc}	20.0
At the azygos vein	C_{azy}	0.5
At the vertebral vein	C_{vv}	0.5

- in supine position, conductances must assume a constant value in accordance with the linear relationship between drops of pressure and flows and in accordance with the values reported in Tables 2.4 and 2.5;
- in upright position, the conductance changes induced by venous collapse (consequence of the hydrostatic pressure gradient) determine a redistribution of blood flow from IJVs to the vertebral-azygos complex and the collateral route. These changes have been assigned to simulate percentage variations of IJV blood flow and vertebral blood flow reported in Table 2.6.

It is worth noting that the last criterion is the only a posteriori information that we used in assigning parameters. All other information was set a priori, i.e. was independent of the results obtainable during posture changes. However, we did not use an automatic procedure to assign these parameters but just a manual adjustment to verify reasonable agreement between model blood flow changes and data.

2.4.2 Equations of the 1D submodel (arterial system of equations)

We simulate the 55 main arteries as depicted in Figure 2.4. The radii, curvatures and elastic parameters of the vessels are available in literature [2, 13, 49, 87, 103, 115]. These parameters are usually not constant along the segments. Table 2.8 shows the number of the vessel in the reduced model, its name, length, mean value of the velocity, characteristic impedance, time delay and reflection coefficient of the peripherals.

A practical method to obtain the electric parameters from the detailed anatomical data is presented below.

The method of obtaining 1D equation of motion in a distensible vessel of varying cross section has been developed in [6, 80, 94]. The governing equations involve conservation of mass and the momentum balance in a control volume of the 1D vessel [80, 94]. The volumetric flow $Q(x,t) = AU$, as a function of space x and time t, relates the cross section area A and the average axial velocity U tethered in longitudinal direction. The pressure P is assumed constant across the section, whereas the radial and azimuthal components of velocity are neglected. For what concerns the arterial part of the model, gravitational effects on pressure are ignored. The system of equations is:

$$\begin{cases} \frac{\partial A}{\partial t} + \frac{\partial Q}{\partial x} = 0 \\ \frac{\partial Q}{\partial t} + \frac{\partial}{\partial x}\left(\alpha \frac{Q^2}{A}\right) + \frac{A}{\rho}\frac{\partial P}{\partial x} = \frac{f}{\rho} \end{cases}$$

Table 2.8: Parameters of the arterial model. *No.* is the vessel number in the model, L is the length of the vessel, c is the mean velocity, Z_0 is the characteristic impedance, t_d is the time delay, and R_f is the reflection coefficient of the peripherals.

No.	*Vessel*	L $[m]$	c $[ms^{-1}]$	Z_0 $[\Omega]$	t_d $[s]$	R_f
1	Ascending aorta	0.0400	5.3400	8.4935e+06	0.0075	-
2	Aortic arch A	0.0200	5.4708	1.4576e+07	0.0037	-
3	Brachiocephalic artery	0.0340	5.9351	5.1604e+07	0.0057	-
4	Subclavian (R)	0.0680	6.4731	1.3522e+08	0.0105	-
5	Common carotid (R)	0.1880	6.5757	1.6054e+08	0.0286	-
6	Vertebral (R)	0.1480	10.9677	1.0154e+09	0.0135	0.3583
7	Brachial artery (R)	0.2350	7.1998	3.6688e+08	0.0326	-
8	Radial artery (R)	0.2340	11.6832	1.5253e+09	0.0200	0.4740
9	Ulnar artery (R)	0.1520	23.0143	2.0393e+09	0.0066	-
10	Interossea artery (R)	0.0790	17.7770	7.3352e+09	0.0044	0.7068
11	Ulnar artery (R)	0.0850	11.0889	1.0266e+09	0.0077	0.3535
12	Internal carotid (R)	0.1180	11.8060	1.8018e+09	0.0100	0.9487
13	External carotid (R)	0.1180	11.9252	1.7714e+09	0.0099	0.5150
14	Aortic arch B	0.0390	5.4901	1.6027e+07	0.0071	-
15	Common carotid (L)	0.2090	6.5757	1.6054e+08	0.0318	-
16	Internal carotid (L)	0.1180	11.8060	1.8018e+09	0.0100	0.9487
17	External carotid (L)	0.1180	11.9252	1.7714e+09	0.0099	0.5150
18	Thoracic aorta A	0.0520	5.5203	1.8450e+07	0.0094	-
19	Subclavian (L)	0.0680	6.4731	1.3522e+08	0.0105	-
20	Vertebral (L)	0.1480	10.9677	1.0154e+09	0.0135	0.3583
21	Brachial artery (L)	0.2350	7.1998	3.6688e+08	0.0326	-
22	Radial artery (L)	0.2340	11.6832	1.5253e+09	0.0200	0.4740
23	Ulnar artery (L)	0.1520	23.0143	2.0393e+09	0.0066	-
24	Interossea artery (L)	0.0790	17.7770	7.3352e+09	0.0044	0.7068
25	Ulnar artery (L)	0.0850	11.0889	1.0266e+09	0.0077	0.3535
26	Intercostals	0.0920	5.1642	1.6054e+08	0.0178	0.5353
27	Thoracic aorta B	0.0520	5.5685	2.0622e+07	0.0093	-
28	Abdominal aorta A	0.0530	5.9701	6.1414e+07	0.0089	-
29	Coeliac artery A	0.0100	6.4555	1.4185e+08	0.0015	-
30	Coeliac artery B	0.0100	6.4555	1.4185e+08	0.0015	-
31	Hepatic artery	0.0660	7.5207	5.1934e+08	0.0088	0.3944
32	Gastric artery	0.0710	7.9679	8.2193e+08	0.0089	0.5290
33	Splenic artery	0.0630	6.9332	2.9557e+08	0.0091	0.2132
34	Superior mesenteric	0.0590	6.3835	1.1539e+08	0.0092	0.1696
35	Abdominal aorta B	0.0530	5.9701	6.1414e+07	0.0089	-
36	Renal artery (L)	0.0320	7.1949	3.5573e+08	0.0044	0.2656
37	Abdominal aorta C	0.0530	5.9701	6.1414e+07	0.0089	-
38	Renal artery (R)	0.0320	7.1949	3.5573e+08	0.0044	0.2656
39	Abdominal aorta D	0.0530	5.9701	6.1414e+07	0.0089	-
40	Inferior mesenteric	0.0500	8.2613	1.0786e+09	0.0061	0.5970
41	Abdominal aorta E	0.0530	5.9701	6.1414e+07	0.0089	-
42	Common iliac (L)	0.0580	6.0922	7.5303e+07	0.0095	-
43	Common iliac (R)	0.0580	6.0922	7.5303e+07	0.0095	-
44	External iliac (L)	0.0830	6.9399	2.7580e+08	0.0120	-
45	Internal iliac (L)	0.0500	14.2533	1.1910e+09	0.0035	0.1903
46	Femoral artery (L)	0.1270	10.2865	5.9687e+08	0.0123	-
47	Deep Femoral artery (L)	0.1270	10.2865	5.9687e+08	0.0123	0.1717
48	Posterior tibial artery (L)	0.3220	15.9357	1.6439e+09	0.0202	0.2376
49	Anterior tibial artery (L)	0.3250	15.3211	4.3267e+09	0.0212	0.7324
50	External iliac (R)	0.0830	6.9399	2.7580e+08	0.0120	-
51	Internal iliac (R)	0.0500	14.2533	1.1910e+09	0.0035	0.1903
52	Femoral artery (R)	0.1270	10.2865	5.9687e+08	0.0123	-
53	Deep Femoral artery (R)	0.1270	10.2865	5.9687e+08	0.0123	0.1717
54	Posterior tibial artery (R)	0.3220	15.9357	1.6439e+09	0.0202	0.2376
55	Anterior tibial artery (R)	0.3250	15.3211	4.3267e+09	0.0212	0.7324

where ρ is the blood density, $f(x,t)$ is the frictional force per unit length and $\alpha(x,t) = \frac{1}{AU^2}\int_A u^2 d\sigma$ is a non dimensional profile shape factor (also called the Coriolis coefficient) that accounts for the non linearity of the sectional integration of the velocity $\mathbf{u} = (\mathbf{x}; t)$. Here, we will use the approximate value $\alpha \approx 1$ in the convective acceleration term of the system above. Blood density ρ and viscosity μ of the blood are assumed to be constant at 37°C so that $\rho = 1050\ kgm^{-3}$ and $\mu = 4.0\ mPas$ [6]. The system above can be derived by integrating the incompressible Navier-Stokes equations over a generic cross section of a cylindrical domain [17, 49, 50, 84, 99, 112].

In 1D modelling the velocity profile is commonly assumed to be constant in shape and axisymmetric. A typical profile satisfying the no-slip condition ($u|_{r=R} = 0$) is [49, 99]:

$$u\left(x,r,t\right) = U\frac{\xi+2}{\xi}\left[1-\left(\frac{r}{R}\right)^{\xi}\right] \tag{2.31}$$

where r is the radial coordinate, $R(x,t)$ is the radius of the lumen (assumed to be circular) and $\xi = \frac{2-\alpha}{\alpha-1}$ is a constant.

An explicit algebraic relationship between P and A (the tube law) is also required to close the system. The tube law is determined by the viscoelastic properties of the vessel walls [48]. Voigt-type visco-elastic laws reproduce, in the first approximation, the main effects of the walls properties on the blood flow in large arteries, including hysteresis and creep [5, 11, 12, 18, 24, 88]. An example of this type of law that neglects the effects of wall inertia and longitudinal pre-stress [34] is given by [5]:

$$P = P_e\left(A,x\right) + \frac{\Gamma(x)}{A_0\left(x\right)\sqrt{A}}\frac{\partial A}{\partial t} \tag{2.32}$$

$$P_e\left(A,x\right) = P_{ext} + \frac{\beta\left(x\right)}{A_0\left(x\right)}\left(\sqrt{A} - \sqrt{A_0\left(x\right)}\right) \tag{2.33}$$

$$\beta\left(x\right) = \frac{4}{3}\sqrt{\pi}E\left(x\right)h\left(x\right) \tag{2.34}$$

$$\Gamma\left(x\right) = \frac{2}{3}\sqrt{\pi}\varphi h\left(x\right) \tag{2.35}$$

where P_e is the elastic component of pressure, $h\left(x\right)$ is the wall thickness, $\beta\left(x\right)$ is related to the wall elasticity whereas $E\left(x\right)$ and $\Gamma\left(x\right)$ to the wall viscosity $\varphi\left(x\right)$, both independent of the transmural pressure. The reference area $A_0\left(x\right)$ is the vessel area when $P = P_{ext}$ and $\frac{\partial A}{\partial t} = 0$, which are typical initial conditions for numerical analysis. Therefore, the local cross sectional area $A(x,t)$ will depend on the shape of the artery given by $A_0\left(x\right)$ and the mechanical properties of the wall, which may change with x.

In the 1D formulation the nodes connecting the arterial segments are treated as discontinuities, which is consistent with the long wavelength approximation. Detailed 3D calculation of flow at arterial bifurcations show that the flow is generally very complex with the possibility of transient separation and the development of secondary flows [6]. Most of these flow features are confined to the region near the bifurcation and the long wave approximation allows one to neglect their effects on the pulse wave in the 1D formulation.

The linearization of the governing equations yields an analogy with a transmission line, where

resistance R, inductance L, and capacitance C are calculated per unit length of vessel as follows:

$$R = \frac{2\,(\xi + 2)\,\pi\mu}{A_0^2} \tag{2.36}$$

$$L = \frac{\rho}{A_0} \tag{2.37}$$

$$C = \frac{2A_0^{3/2}}{\beta} \tag{2.38}$$

Equations 2.36 to 2.38 allows us to determine the wave speed $c = \sqrt{\frac{1}{CL}}$ and the characteristic impedance $Z = \frac{\rho c}{A_0}$ for every segment of a given artery (see Table 2.8) [6].
The linearized system of governing equations yields an analytical solution for wave reflection and transmission where the physical properties of the arteries change. At a splitting and merging junction, the reflection coefficients R_f^a, R_f^b and R_f^c for wave propagating in the parent a and two daughter, vessels b and c respectively can be defined as the ratio of the pressure amplitude in the reflected wave to the pressure amplitude in the incident wave. They can be expressed as a function of the characteristic impedance of each segment:

$$R_f^a = \frac{(Z_0^a)^{-1} - \left(Z_0^b\right)^{-1} - (Z_0^c)^{-1}}{(Z_0^a)^{-1} + \left(Z_0^b\right)^{-1} + (Z_0^c)^{-1}} \tag{2.39}$$

The transmission coefficients T_a, T_b and T_c for waves propagating in the parent vessel a, and daughters vessels b and c, can be defined as the ratio of the pressure perturbation transmitted to the other two vessels to the pressure perturbation in the vessel where the initial wave is propagated:

$$T^j = 1 + R_f^j, j = a, b, c \tag{2.40}$$

The outlet of each terminal branch is assumed to be coupled to a single resistance R_1 [3], so that the corresponding reflection coefficient is:

$$R_f = \frac{R_1 - Z_0}{R_1 + Z_0} \tag{2.41}$$

Putting $R_1 = 0$ yields spurious wave reflections and $R_1 = Z_0$ corresponds to complete absorption of any incoming wave [3], where Z_0 is the characteristic impedance of the peripheral segment. We use the latter assumption in all the terminal branches of the model. At the aortic valve we define a time-dependent reflection coefficient, R_v. As showed in Section 2.3.2), we set $R_v > 1$ (more pressure is reflected than it comes in) when the aortic valve is open and $R_v = 1$ (total reflection) when it is closed [4].

Chapter 3

Experimental validation of the mathematical model

3.1 Equation solver

During the first part of the work the connection between the 0D submodels (intracranial and venous) was performed. To do that, we used the software package Berkeley Madonna (free available version beta 9.0.111 [63]), developed on the Berkeley campus under the sponsorship of National Science Foundation and National Institutes of Health and widely used in biology and biological engineering [35, 42]. Sensitivity analysis and first comparisons with literature and experimental results were also performed with the same software. After that, we moved to the software package MATLAB R2016a (version 9.0.0.341360, [134] developed by The MathWorks Inc., Natick, MA, 2016) to connect 1D and 0D submodels and allow an easier user interface by using the Simulink block diagram environment. To solve the whole system of equations we resort to an algorithmic approach. We chose the iterative method Runge-Kutta 4 to perform all the computations. The stepsize used to solve the system is 0.001 s.

3.2 Experimental MRI and US data

As we said in Chapter 2, the model is validated against experimental and literature results, concerning respiration, tachycardia, jugular stenosis, and the effect of a posture change from supine to upright.

We cannot use animal data taken from the literature since the circulatory system investigated is significantly different in animals compared with humans. In particular, the extracranial venous circulation in humans is specifically adapted to the maintenance of an upright posture, which is the peculiar subject of the present work. For this reason, we dealt with some *ad hoc* measurements on volunteers, using magnetic resonance imaging (MRI) and echo-color Doppler (ECD) technique, to assess blood flow changes in the different portions of the circulatory system and to provide a complete quantitative set for model validation. We took advantage of the availability of both MR imaging and ECD experimental data of blood flow (Tables 2.5 and 2.6) to exploit the different advantages they provide.

MR imaging includes phase contrast (PC) imaging for flow quantification, along with 2D time–of–flight MR Venography (2D TOF MRV) for anatomic assessment [8, 46, 83]. MR imaging based techniques allow the inclusion of information about minor vessels besides the common carotid, internal carotid, and vertebral arteries, internal jugular (IJVs) and vertebral veins.

The ECD technique [75], even if not useful for detecting minor routes, is a cheaper and faster methodology, suitable for measurement of blood flow in both the supine and upright conditions. We used ECD to obtain information about the percentage variation of average flows due to a change of posture.

To validate the model outcomes, we used supine average arterial and venous extracerebral blood flow obtained by using PC MRI data from 49 individuals with stenosis in the acquisition plane at the level of the disc between the second and third vertebrae of the left internal jugular vein IJV (UL-L ST), 20 with stenosis in the acquisition plane at the level of the disc between the fifth and sixth vertebrae of the right IJV (LL-R ST), and 38 healthy controls (NST, without stenosis), as reported in Table 2.5. Average data from a second group of 10 healthy volunteers screened with ECD technique were used to evaluate flow variations due to posture change (Table 2.6).

3.2.1 MRI data for flow quantification

One hundred seven subjects were imaged with 3T MRI scanners at 4 imaging sites by using a 3T Signa HDxt scanner (GE Healthcare, Milwaukee, Wisconsin) with a 12-channel head/neck coil arrangement (site 1, Newport Diagnostic Center, Newport Beach, California), a 3T Trio scanner (Siemens, Erlangen, Germany) (sites 2, Applied fMRI Institute, San Diego, California, and 3, Synergy Health Concepts, Newport Beach, California), and a 3T Verio scanner (Siemens) (site 4, Wayne State University, Detroit Michigan) with a 16-channel head/neck coil arrangement. All data collection studies were HIPAA-compliant and met IRB approval. MRI data were collected with a venous imaging protocol specifically designed to evaluate vessel structure and function [45].

Three-dimensional contrast-enhanced MRV and 2D TOF MRV were used to assess the anatomy of the extracranial vessels. Imaging parameters and inclusion/exclusion criteria have been described in previous literature [45]. Blood flow was quantified with PC-MRI at two different cervical levels: one at the C2-C3 neck level, in which the flow slice is taken above the carotid bifurcation (upper level, at the disc between second and third vertebrae), and one at the C5-C6 neck level (lower level, at the disc between the fifth and sixth vertebrae) [8, 46, 83].

Two raters evaluated MRV to assess stenosis of the IJVs in all samples using established methods [45]. In assessing jugular stenosis, an absolute threshold for the cross sectional area measurement is used. Subjects were classified as stenotic (ST) if the cross sectional area of the IJV was $< 25\ mm^2$ at or caudal to the C3 level and $< 12.5\ mm^2$ cranial to the C3 level [30, 31, 45, 46, 92]. This method contrasts with recent works which use a percentage method [70, 107] typically used in measuring arterial stenosis. The percentage method is flawed due to the variation in IJV size and shape, its venous tributaries, as well as its compliance, sometimes manifesting as pinpoints, elliptical, or crescentic shapes [130].

The whole population was divided into 3 different subgroups:

- 38 subjects classified as nonstenotic (NST);
- 20 subjects with stenosis at the lower level of the right IJV (LL-R ST);
- 49 subjects with stenosis at the upper level of the left IJV (UL-L ST).

Discernable arterial and venous structures that flow to and from the cerebrum were identified and sub-typed using venography and PC flow sequences. Vessel boundaries were delineated automatically by using a full width at half maximum region-growing threshold method [52,54] with manual modification applied when appropriate. Boundaries for each vessel were checked on the PC magnitude and phase maps. Signal Processing In NMR software (SPIN; MR Imaging Institute for Biomedical Research, Detroit, Michigan) [133] was used to evaluate the presence and dimensions of stenosis to IJVs and to quantify blood flows. Data were processed in a blinded manner by analysts trained in MRI signal processing with several years experience each. Flow rates were calculated based on integrated flow velocities within the vessel lumen. A maximum velocity encoding of 50 cm/s was used, and phase unwrapping was performed when the flow velocity exceeded this value.
For all the subjects, we calculated cerebral blood flow Q (the total blood volume entering the cranial cavity per unit time, defined as the sum of flows in the internal carotid and vertebral arteries at the C2/C3 level). The amount of flow drained by the right and left IJV is measured at both the C2/C3 and C5/C6 levels (here referred to as blood flow drained by the upper segment of the right internal jugular vein [Q_{jr3}], blood flow drained by the upper segment of the left internal jugular vein [Q_{jl3}], blood flow drained by the middle segment of the right internal jugular vein [Q_{jr2}], and blood flow drained by the middle segment of the left internal jugular vein [Q_{jl2}], respectively). The fraction of cerebral blood flow exiting the skull from the vertebral system measured at the level of the disc between the second and third vertebrae (Q_{vv}) is the fraction of Q exiting the skull from the vertebral system, measured at the C2/C3 level. Finally, we took into account the flow in the external carotid arteries (Q_{ex}, the amount of extracranial blood to the head and face, measured at the C2/C3 level). We chose to calibrate the model so that it reproduced these experimental flows.
There are some drawbacks to this technique. The resolution of MRI methods is limited and this may affect the prediction of stenosis and flow. Beside that, venography method used have been shown to have lower specificity relative to catheter venography [129], which remains the gold standard for assessing stenosis, although it is invasive and it does not provide global and quantifiable functional information about the venous system. On the other hand, some work reports good agreement with venography methods and contrast venography, even if MRV may have the tendency to overestimate vessel stenosis [117]. Morphological IJV changes may also be due to several other factors: head and neck position, intrathoracic pressure, extrinsic compression from the coil, and changes due to swallowing movements [130]. Small arteries and venules are difficult to measure using PC MRI so it is not certain how the microvasculature is affected by a primary venous stenosis.

3.2.2 ECD data for supine and upright flow comparison

ECD data of 10 healthy volunteers from a recent work [127] were used as a reference for the average blood flow variation from the supine condition to the upright one. We used those experimental data to assess the average percentage flow variation in the upright IJV and vertebral ducts with respect to the supine condition. Unlike other datasets available in literature, these data allowed us to assess the supine/sitting variation for the three segments of both left and right IJVs (J3, J2, and J1, respectively [123]) we chose to simulate.
We chose to calibrate the model so that it reproduced upright-to-supine percentage variation of total jugular (blood flow drained by the upper segment of the internal jugular veins [Q_{j3}] = $Q_{jr3} + Q_{jl3}$, blood flow drained by the middle segment of the internal jugular veins [Q_{j2}] = $Q_{jr2} + Q_{jl2}$, blood flow drained by the lower segment of the internal jugular veins [Q_{j1}] = blood flow drained by the lower segment of the right internal jugular vein [Q_{jr1}] = blood flow drained by the lower segment of the left internal jugular vein [Q_{jl1}]) and vertebral (Q_{vv}) flow.

3.3 Simulation results of blood flows and pressures

In this section we show first results from this new model of the cerebral and extracerebral circulation, to highlight the stability of the outcomes and to provide validation with experimental results.
We show simulations related to relevant phenomena affecting the extracranial arterial and venous system, such as the change in pressure due to respiration, posture changes, movement, changes in heart beating and functionality of the left ventricular valve and the onset of IJV obstructions (stenosis) [120, 128]. Therefore, we focus attention on the response of the cerebral and venous drainage system to the arterial pulse waves produced by the heart (taking also into account the effect of the left ventricular valve) and to other waves generated at legs to simulate the effect of cycling (indeed, muscles contraction in limbs and other organs must also propagate through the system). The present model can provide a quantitative account of the effect of such physical exercise, link it to the effect of respiration on the venous side, and show simulations of venous sinuses pressure P_{vs} and other pressures and flow profiles. In other words, we are able to find out how the cited variations of arterial and venous pressures, eventually coupled with variations due to the gravity field or the occurence of some vascular disease at the arterial (tachycardia) or venous side (IJV blockage), can affect the proper brain drainage. The results may help to define indications of the effect of physical exercise (a recognized prophylactic factor against brain diseases such as ischemia) on both healthy subjects and people with recognized cardiac pathology such as tachycardia or typical venous obstruction patterns [19, 30, 86, 120, 122, 126].
Results show that the system of equations is stable from the mathematical point ov view, whitout any kind of divergent solution. Moreover, the average behavior of simulated flows is in agreement with experimental data.

3.3.1 Simulations with basal parameter values

Simulation results of particular interest are shown in the following. We verified that the model, with basal parameter values, can simulate the main blood flow changes from supine to upright position.
Figure 3.1 summarizes amounts of simulated total inflow Q_{tot}, flow to face and neck Q_{ex}, cerebral blood flow Q, and total jugular (sum of left and right), vertebral, and collateral flows at equilibrium (Q_{j3}, Q_{j2}, Q_{j1}, Q_{vv}, and Q_{c3}), to point out the variation between supine and upright posture.

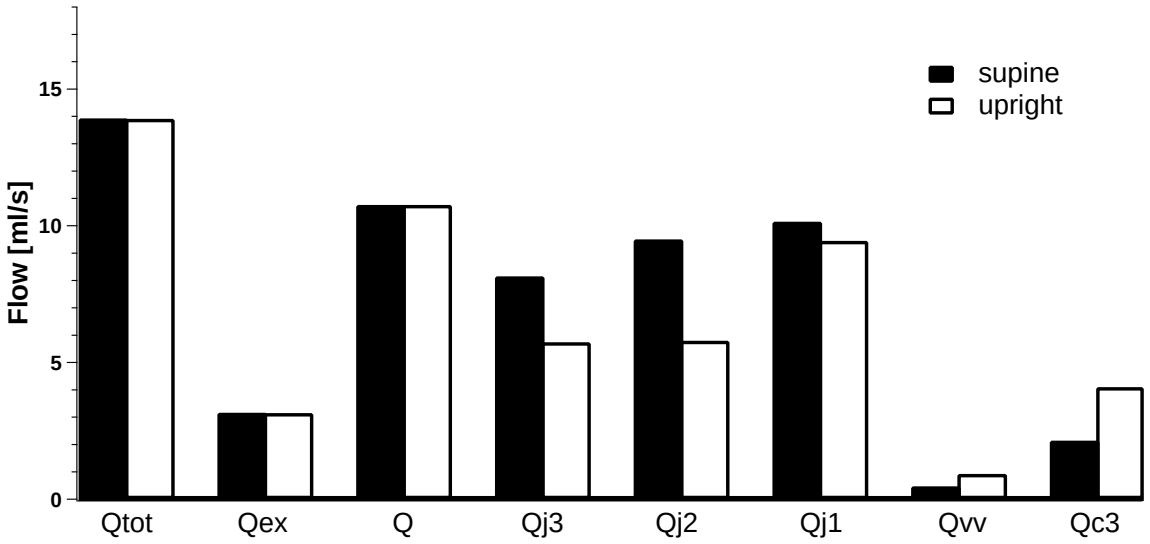

Figure 3.1: Average total inflow Q_{tot}, flow to face and neck Q_{ex}, cerebral blood flow Q, total jugular flows Q_{j3}, Q_{j2}, Q_{j1}, vertebral flow Q_{vv} and collateral flows Q_{c3} at equilibrium, in supine and upright simulations. The percentage changes of Q_{j3}, Q_{j2}, Q_{j1} and Q_{vv} are -29.5%, -39.0%, -6.9%, and $+95.2\%$, which fit those in Table 2.6 very well.

We see that Q_{tot} is the sum of Q_{ex} and Q. Moreover, the histogram shows the different type of drainage Q undergoes in supine and upright position. These different blood distributions are due to the changes in IJV conductances that occur when upright position is simulated (Equation from 2.25 to 2.30). The last portion of the IJVs exhibits a less pronounced collapse in upright condition compared with the first tract, due to a smaller gravitational pressure gradient and due to the effect of the negative intrathoracic pressure. Results can be summarized as follow.
Q remains constant despite the posture change, as a consequence of the action of autoregulatory mechanisms. In fact, the moderate increase in P_{vs} lies well inside the autoregulatory range [108]. Blood flow Q_{j3} in the upper portion of the IJVs exhibits a dramatic fall in the upright state (most of the cerebral blood flow passes through the collateral route $c3$), while blood flow in the vertebral veins Q_{vv} increases by about two times. Furthermore, blood flow in the IJVs (the dominant drainage pathway of the brain) progressively increases from J3 to J1 independent of the posture, since part of blood flow is drawn from the collateral route to the jugular tract via the anastomoses $cj3$ and $cj2$ (see Figure 2.4). When passing to upright, the model simulates a flow decrease in every tract of the IJVs, with increase in the vertebral flow. These results match the experimental evidence of percentage flow variation due to posture change summarized in Table 2.6.

Figure 3.2 shows how the model simulates flows at the equilibrium for the NST group (Table 2.5).

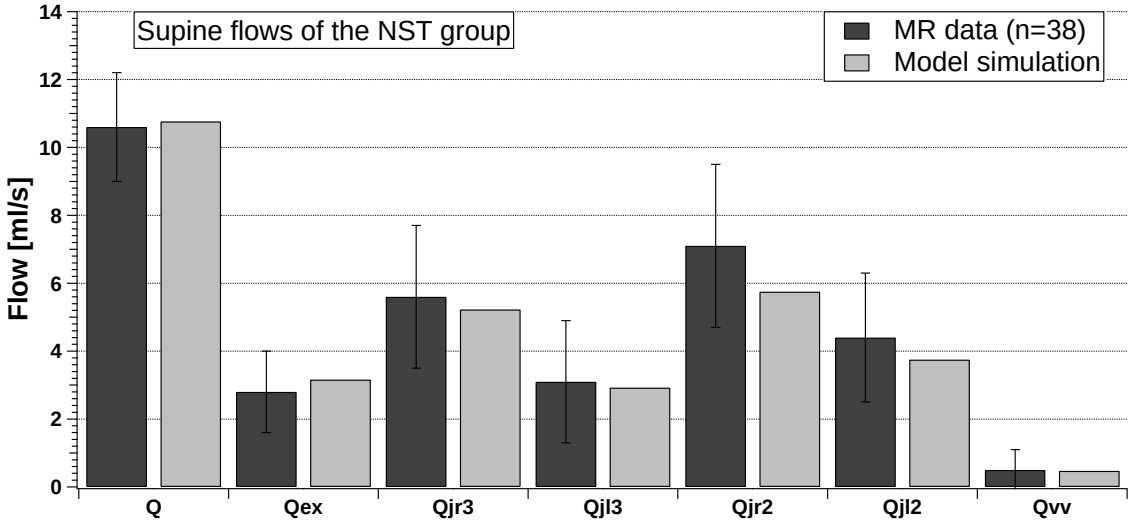

Figure 3.2: Comparison between supine MRI data (dark columns) and model simulation (light columns) of the NST group.

Every IJV segment carries more flow than the vertebral pathway. In addition, average blood flow in the right IJV is greater than in the left one, for both C2/C3 and C5/C6 levels ($Q_{jr3} > Q_{jl3}$ and $Q_{jr2} > Q_{jl2}$). Finally, average jugular flow increases from the upper to lower levels ($Q_{jr2} > Q_{jr3}$ and $Q_{jl2} > Q_{jl3}$). The model (light columns) properly reproduces the behavior of experimental flow (dark columns). Indeed, all the simulations match the average values of the dataset.
Figure 3.3 shows the model outcomes of the cerebral, external, IJVs (left and right), and vertebral average flow in the supine and upright conditions for the NST group.

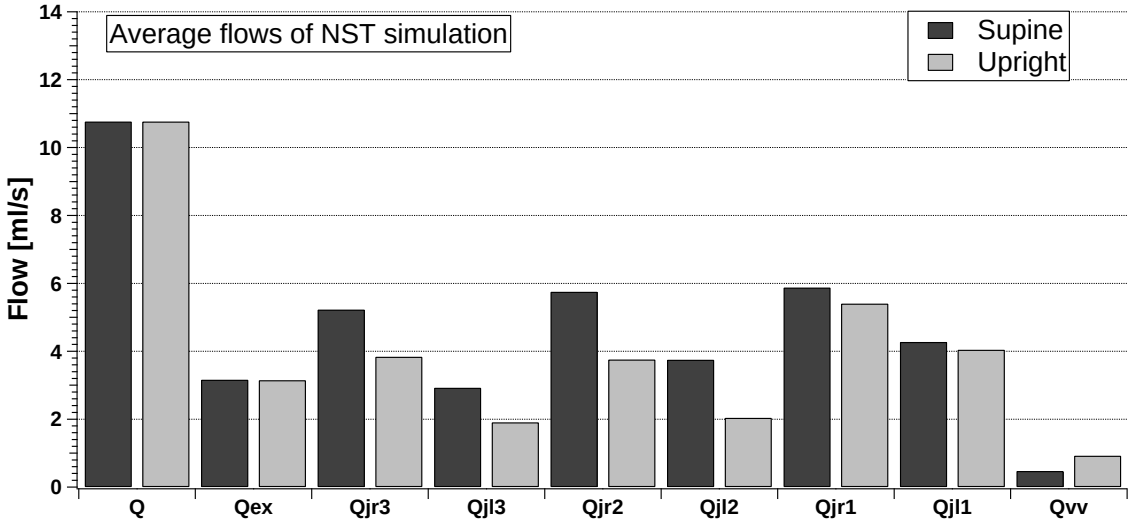

Figure 3.3: Model simulation of the cerebral, external, IJVs (left and right), and vertebral average flows in supine and upright conditions for the NST group.

All jugular flows are reduced when the simulated NST subject is sitting, while the vertebral flow increases. Because this was a simulation of a NST condition, our aim was to

reproduce the left-right dominance of the IJVs ($Q_{jr3} > Q_{jl3}$, $Q_{jr2} > Q_{jl2}$, and $Q_{jr1} > Q_{jl1}$), the prevalence of the IJV pathways with respect to the vertebral one (i.e. Q_{vv} lower than any other flow related to brain drainage), and the increase in jugular flow from J3 to J1 ($Q_{jr1} > Q_{jr2} > Q_{jr3}$ and $Q_{jl1} > Q_{jl2} > Q_{jl3}$). Figure 3.3 shows that simulation results satisfy all these requirements.

Top part of Figure 3.4 shows the waveform of P_{vs}, in response to the standard heart action given in Figure 2.5.

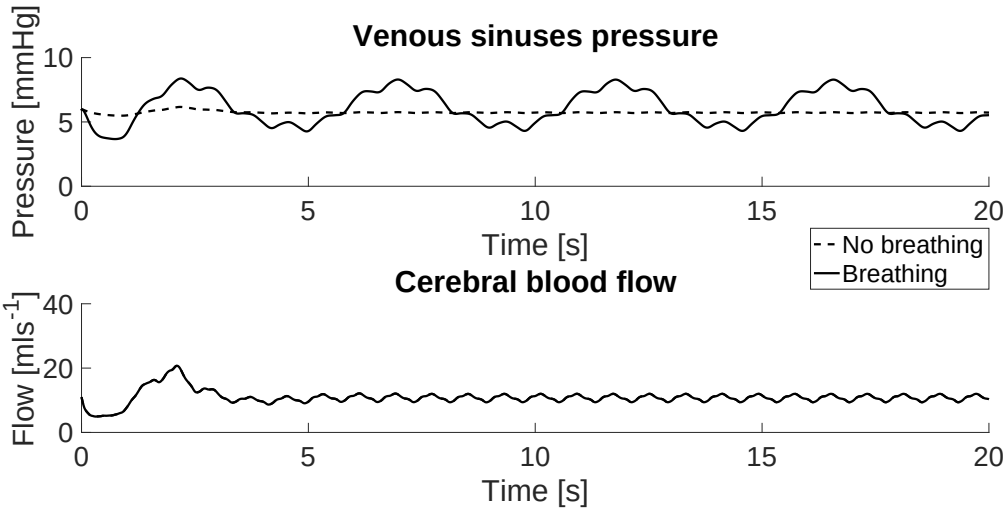

Figure 3.4: Simulations of P_{vs} and Q in supine condition. No exercise, tachycardia or venous obstructions are simulated.

The pressure profile stabilizes after about 7 cardiac cycles ($\sim$ 5 s). When the simulation is performed without the effect of breathing on P_{cv} (Figure 2.3), we see that P_{vs} is constant at 5.7 mmHg (dashed line). The effect of the variation of P_{cv} due to breathing is visible in the solid line of the top plot of Figure 3.4. The average value of P_{vs} slightly increases to the value of 6.2 mmHg, but the remarkable effect is on its variation in time. Indeed, now it oscillates between 4.3 and 8.3 mmHg, with a sinusoidal shape that reflects the respiration waveform of Figure 2.3.

Bottom part of Figure 3.4 shows the waveform of Q, in response to the standard heart action given of Figure 2.5. Q stabilizes after about 7 cardiac cycles ($\sim$ 5 s). The flow profile oscillates between 9.4 and 12.0 ml/s, with an average value of 10.8 ml/s. The complete superposition between the traces of Q related to simulation with and without the breathing effect of Figure 2.3 shows that the cerebral perfusion is not affected by respiration changes, i.e. by changes of P_{vs} till the order of what reported in the top part of Figure 3.4.

Top part of Figure 3.5 shows the waveform of P_{vs}, in response to the standard heart action given in Figure 2.5, coupled with breathing (Figure 2.3) and the simulation of a posture change from supine to upright at $t = 80$ s.

During supine posture (and after about 7 cardiac cycles, corresponding to $\sim$ 5 s, to reach equilibrium), P_{vs} oscillates between 4.3 and 8.3 mmHg (average value of 6.2 mmHg), with a sinusoidal shape that reflects the respiration waveform of Figure 2.3. Then, at $t = 80$ s, we perform the posture change to upright. Now, P_{vs} oscillates between 5.4 and 8.4 mmHg around an average value of 6.8 mmHg, with no remarkable differences in the sinusoidal shape. From bottom part of Figure 3.5 we see that postural change does not affect the behavior of

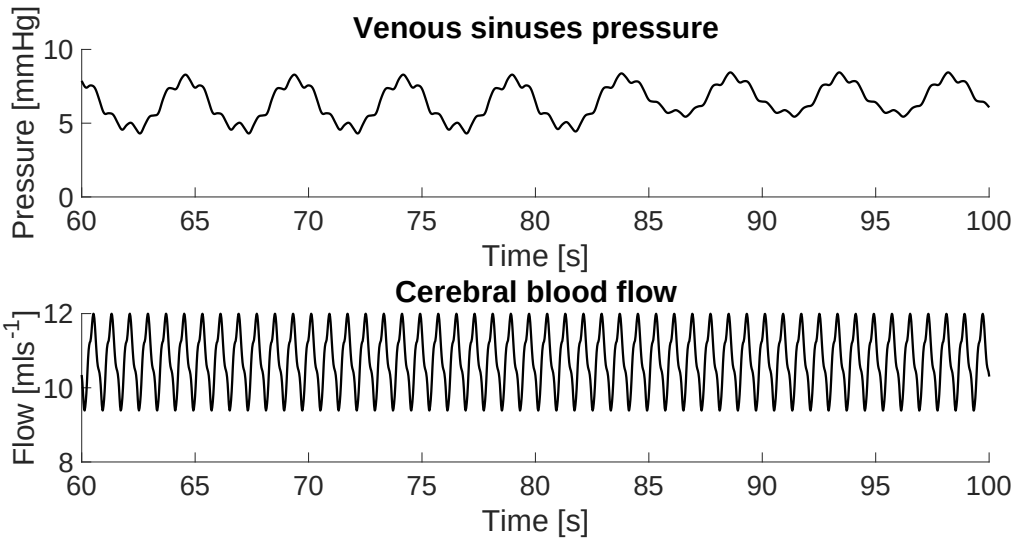

Figure 3.5: P_{vs} and Q during simulation of posture change from supine to upright, while breathing. No exercise, tachycardiac or stenotic effect is simulating.

cerebral blood flow Q. Cerebral blood flow stabilizes after about 7 cardiac cycles ($\sim$ 5 s). It oscillates between 9.4 and 12.0 ml/s, around an average value of 10.8 ml/s, with no variations during the transition from supine to upright.
Top part of Figure 3.6 shows the waveform of P_{vs} while upright, in response to the standard heart action given in Figure 2.5, coupled with breathing (Figure 2.3) and the simulation of cycling exercise (see Figure 2.7) starting at $t = 80$ s till the end of simulation.

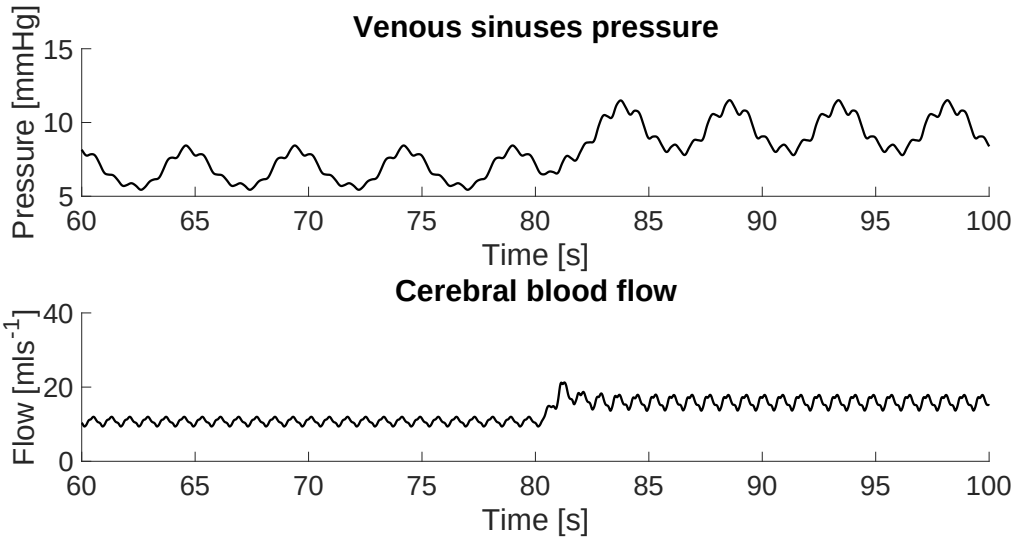

Figure 3.6: P_{vs} and Q during simulation of cycling exercise, while breathing and upright. No tachycardiac or stenotic effect is simulating.

During upright posture (and after about 7 cardiac cycles, corresponding to 5 s, to reach equilibrium), P_{vs} oscillates between 5.4 and 8.4 mmHg around an average value of 6.8 mmHg, with a sinusoidal shape that reflects the respiration waveform of Figure 2.3. Then, at $t = 80$ s, we start to simulate the cycling exercise (see Figure 3.6). Now, P_{vs} oscillates between 7.8 and 11.5 mmHg around an average value of 9.5 mmHg, with little differences in the sinusoidal shape at the level of details.

From bottom part of Figure 3.6 we see that cycling exercise affects the behavior of Q. Cerebral blood flow stabilizes after about 7 cardiac cycles ($\sim$ 5 s). It oscillates between 9.4 and 12.0 ml/s, around an average value of 10.8 ml/s. Then, at $t = 80$ s, we start to simulate the cycling exercise (see Figure 2.7). Q needs another interval time of about 7 cardiac cycles ($\sim$ 5 s) to reach the new equilibrium. In the new equilibrium, Q oscillates between 13.6 and 17.9 ml/s, around an average value of 15.9 ml/s.
Top part of Figure 3.7 shows the waveform of P_{vs} while upright, in response to the standard heart action given in Figure 2.5, coupled with breathing (Figure 2.3). At $t = 80$ s we simulate a tachycardia episode, so that the frequency of the heart action is doubled till the end of simulation.

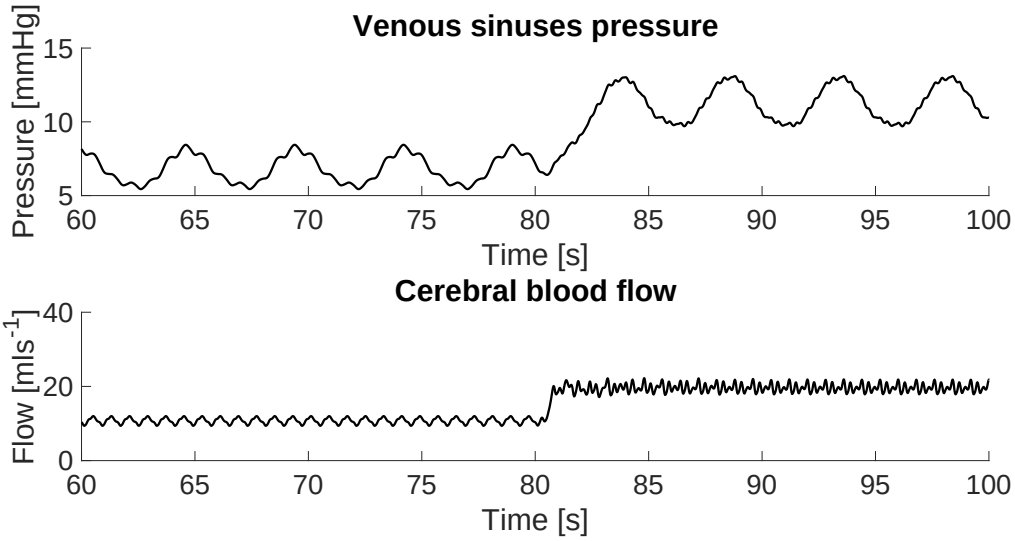

Figure 3.7: P_{vs} and Q during simulation of tachycardia, while breathing and upright. No exercise or stenotic effect is simulating.

During upright posture (and after about 7 cardiac cycles, corresponding to 5 s, to reach equilibrium), P_{vs} oscillates between 5.4 and 8.4 mmHg around an average value of 6.8 mmHg, with a sinusoidal shape that reflects the respiration waveform of Figure 2.3. Then, at $t = 80$ s, we start to simulate the tachycardiac disease. In the new situation, P_{vs} oscillates between 9.7 and 13.1 mmHg around an average value of 11.3 mmHg, with a smoother sinusoidal shape with respect to the condition of absence of tachycardia (i.e. halved heartbeat frequency).
From bottom part of Figure 3.7 we see that tachycardia affects the behavior of Q. Cerebral blood flow stabilizes after about 7 cardiac cycles ($\sim$ 5 s). It oscillates between 9.4 and 12.0 ml/s, around an average value of 10.7 ml/s. Then, at $t = 80$ s, we start to simulate the tachycardia. Q needs another interval time of about 14 cardiac cycles ($\sim$ 5 s) to reach the new equilibrium. In the new equilibrium, Q oscillates between 17.9 and 21.9 ml/s, around an average value of 19.6 ml/s.

3.3.2 Simulations of stenosis

To clarify the role of the main routes involved in cerebral venous outflow, and a possible effect of a pathological alteration, we performed the following simulations:

- interruption of blood flow in a single route by assigning a zero value to the corresponding conductance;

- simulation of four typical pathological alterations already reported in the clinical literature [120] and characterized by a conductance reduction in multiple venous paths.

To simulate patients with stenosis at the lower level of the right IJV (LL-R ST) and stenosis at the upper level of the left IJV (UL-L ST) (i.e. to reproduce the experimental blood flows reported in Table 2.5), some parameters must be changed from the basal value assigned to simulate the NST case of Section 3.3.1. We decided to maintain these parameters to a minimum, to reduce the number of ad hoc assumptions.
Hence, LL-R ST subjects were characterized by a reduction in conductance of the right J2 tract (obtained through a reduction in the parameter for the basal conductance of the middle segment of the right IJV, k_{jr2}), while UL-L ST subjects were characterized by a reduction in conductance of the left J3 tract (obtained through a reduction in parameter for the basal conductance of the upper segment of the left IJV, k_{jl3}). Both parameters were diminished by the same percentage variation, to fit the patient data. Finally, we assumed that the venous vascular bed compensates the chronic stenotic phenomena via an increase in the conductance of the vertebral path (parameter G_{vv1}). Therefore, to properly simulate LL-R ST average flow data, we needed to decrease the conductance of the right J2 segment with respect to the NST case (-86%). The same percentage variation is needed in the left J3 segment to reach good simulations of the UL-L ST cases. In both situations, we also needed to considerably increase the conductance of the upper part of the vertebral system (G_{vv1}).
This step-by-step optimization procedure (assumption of progressive pressure reduction, choice of proper conductances of large vessels to simulate supine NST flows, choice of proper conductances of anastomoses to simulate upright NST flows, variation of NST conductances to simulate vessel blockages and flows of stenotic cases) ensures that model solutions fit both healthy and stenotic flow outcomes with a unique set of parameters. We are aware that the model has many parameters, so the solution may not be unique. However, we introduce some strong constraints to our model, such as physiologic values for pressure or change of conductances only in the vertebral segment and in the IJVs segments affected by stenosis, to reduce the parameter choice. Results are summarized in Figure 3.8, 3.9, and 3.10 with regards to the effect of a single closure on P_{vs}, outflow from the confluence of the two jugular veins Q_{svc1} and vertebral blood flow Q_{vv}, respectively.

Results show that the cerebral venous outflow system is quite robust in response to a single vessel closure, both in supine and upright conditions. This signifies that interruption of a single path can be quite easily replaced by an alternative route.
Venous sinuses pressure P_{vs}, the link between intracranial and jugular-vertebral circuit, increases with change of posture from supine to upright in basal conditions (+0.6 mmHg) as shown in Figure 3.8. In supine posture, total occlusion of right jugular vein ($G_{jr3} = 0$, $G_{jr2} = 0$, and $G_{jr1} = 0$) produces little increases of the value of P_{vs}. Also, changes due to occlusions of collateral network and vertebral veins are not appreciable. Looking at the simulation of upright condition, it is evident that P_{vs} is more influenced by lack of drainage of the collateral and jugular network (with more effect if the stenosis occurs at lower segments), while occlusion at the vertebral system affects P_{vs} with little increases.

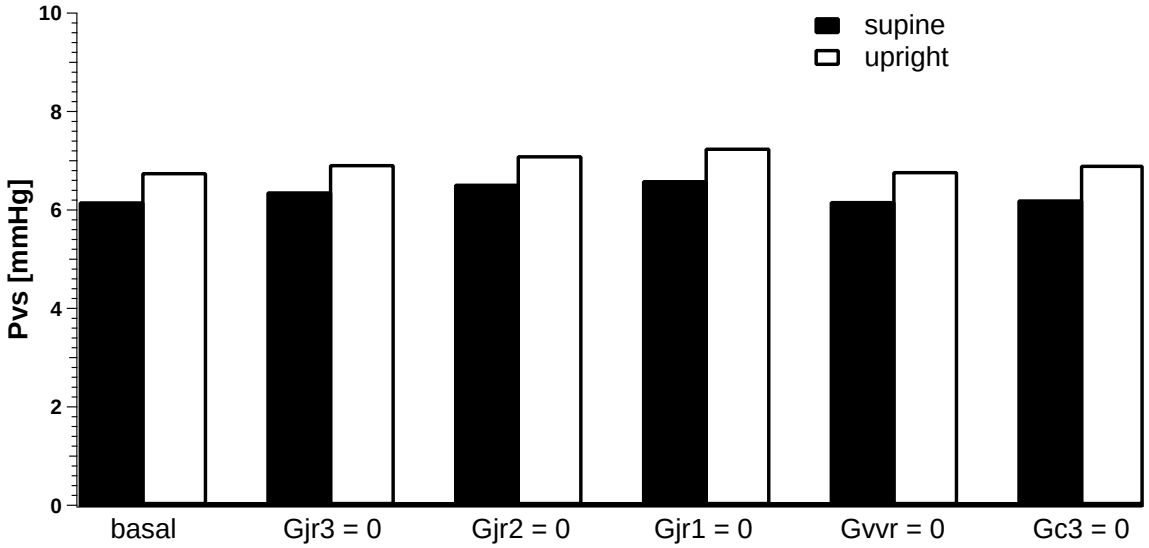

Figure 3.8: Effect of a single closure on venous sinuses pressure (P_{vs}).

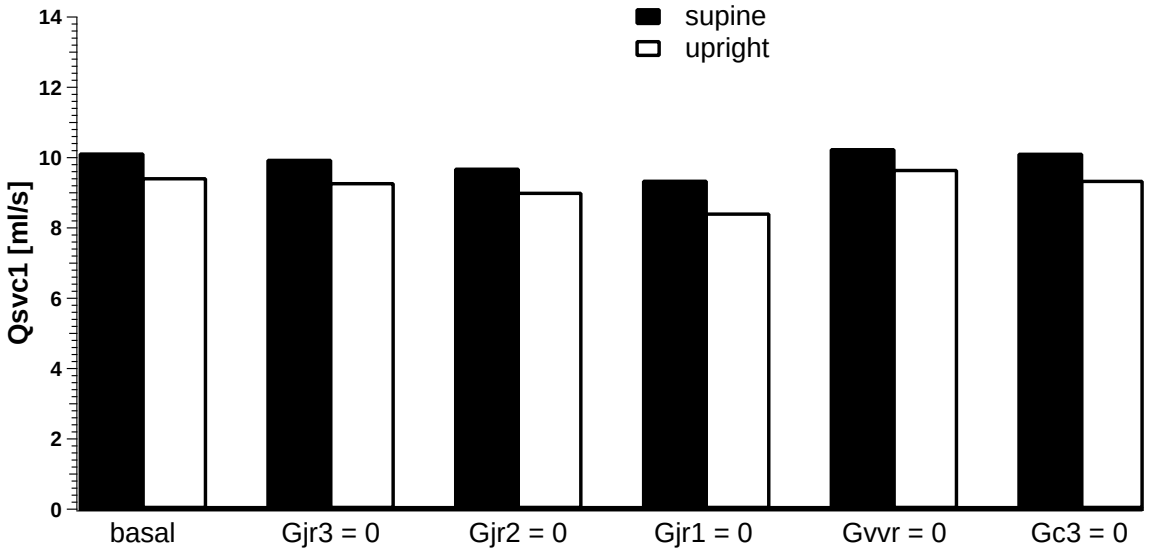

Figure 3.9: Effect of a single closure on outflow from the confluence of the two jugular veins (Q_{svc1}).

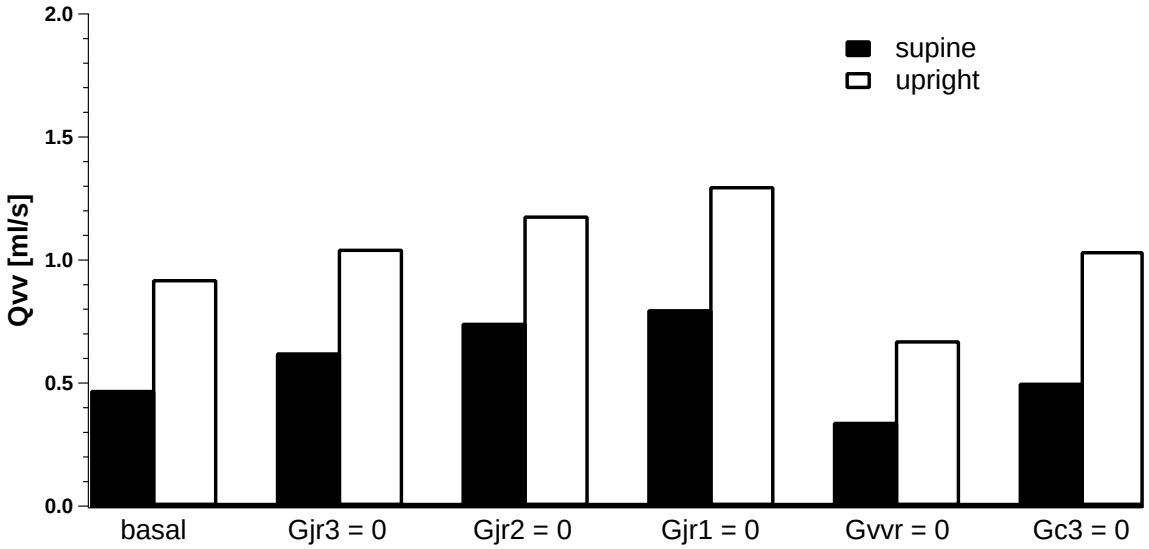

Figure 3.10: Effect of a single closure on vertebral blood flow (Q_{vv}).

Figure 3.9 shows that output flow from the confluence of jugular veins Q_{svc1} decreases of about 0.7 ml/s from the supine to upright condition. In supine condition, every kind of occlusion provokes little or negligible changes of this flow. The same situation also occurs in upright condition.

Output flow from the vertebral veins Q_{vv} rises of 0.5 ml/s during change from supine to upright conditions as reported in Figure 3.10. Little variations from the basal supine value occur when a jugular vein is occluded (with more effect if the stenosis occurs at lower segments). Conversely, basal upright flow is also quite increased by occlusion of the collateral network ($G_{c3} = 0$) and lowered by occlusion of right vertebral vein ($G_{vvr} = 0$). In all cases, the most influential closure is found to be the terminal part of the IJV. Naturally, an obstruction in a vertebral vein causes a significant decline in vertebral blood flow, with a redistribution toward the jugular and collateral circulations.

Finally, we tested the behavior of the external flow Q_{ext} for all the conditions described above. In the present model Q_{ext} diminishes by 0.05 ml/s when venous sinuses pressure increases (for example, when moving from supine to upright condition both in a healthy and a pathological subject). This external flow is not significantly affected by any kind of occlusion we tested.

We also performed the whole sensitivity analysis in the conditions of weak autoregulation reported in Figure 2.8. Results show that for reduced cerebral autoregulation (i.e., by changing the value of G_{aut} till 1/10 of its initial value) every value of pressure and flow reported in the sensitivity analysis does not change significantly. The reason is that, in our simulations, P_{vs} always exhibits a mild change (+1 or +2 mmHg), which is a minimal fraction of cerebral perfusion pressure. Since cerebral blood flow is subjected to regulation mechanisms, the final change in Q is always 1% of basal (even when using a moderate autoregulation gain), which has negligible effects on the final results.

Figures 3.11 and 3.12 compare the same flows of Figure 3.2 for the LL-R ST and UL-L ST groups.

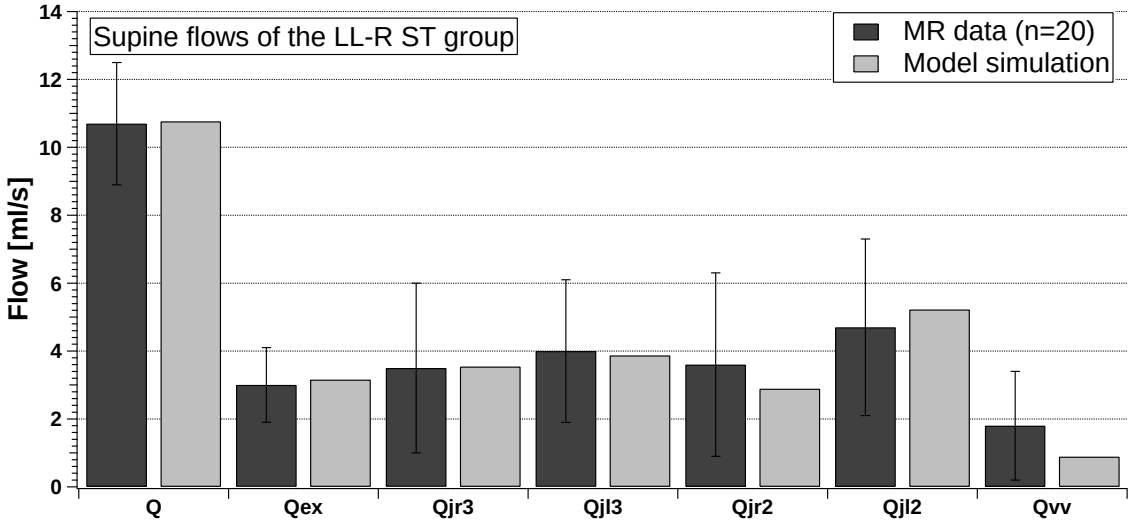

Figure 3.11: Comparison between supine MRI data (dark columns) and model simulation (light columns) of the LL-R ST group.

Average inflows of these stenotic groups (Q and Q_{ex}) are similar to the NST inflows (see Figure 3.2). Conversely, the average outflow behavior described in Fig 3.2 is now modified

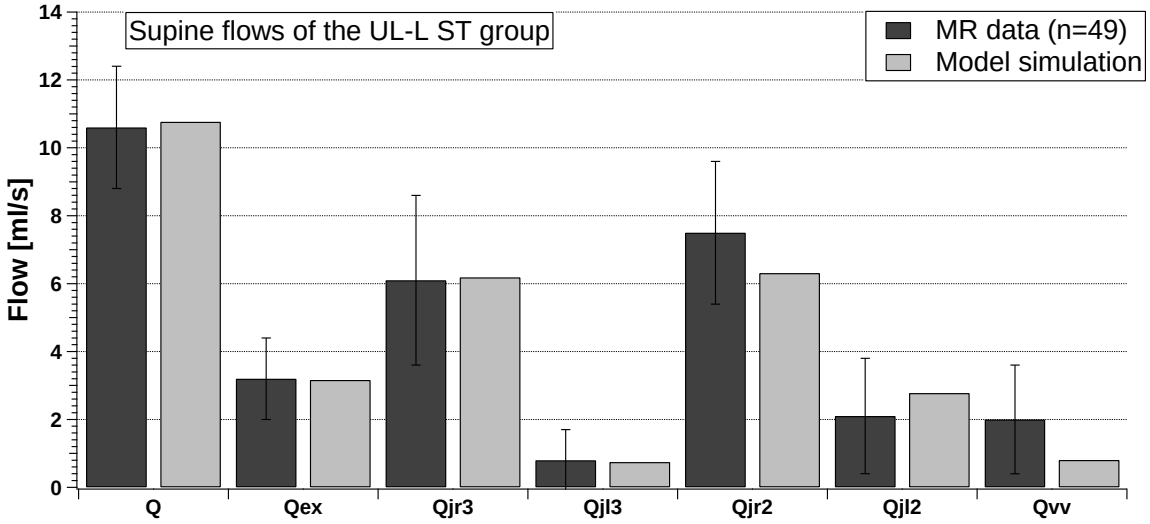

Figure 3.12: Comparison between supine MRI data (dark columns) and model simulation (light columns) of the UL-L ST group.

due to the presence of stenosis. Q_{vv} is increased with respect to the NST case, being also sometimes comparable with the flow in the IJV segments. The right-left IJV dominance is impaired, being the difference between average flows lost for the LL-R ST group ($Q_{jr3} \approx Q_{jl3}$ and $Q_{jr2} \approx Q_{jl2}$) or markedly increased for the UL-L ST group ($Q_{jr3} \gg Q_{jl3}$ and $Q_{jr2} \gg Q_{jl2}$). The light columns in Figures 3.11 and 3.12 show that the model outcomes can also reproduce these situations.

Figures 3.13 and 3.14 compare the same flows of Figure 3.3 for the LL-R ST and UL-L ST groups.

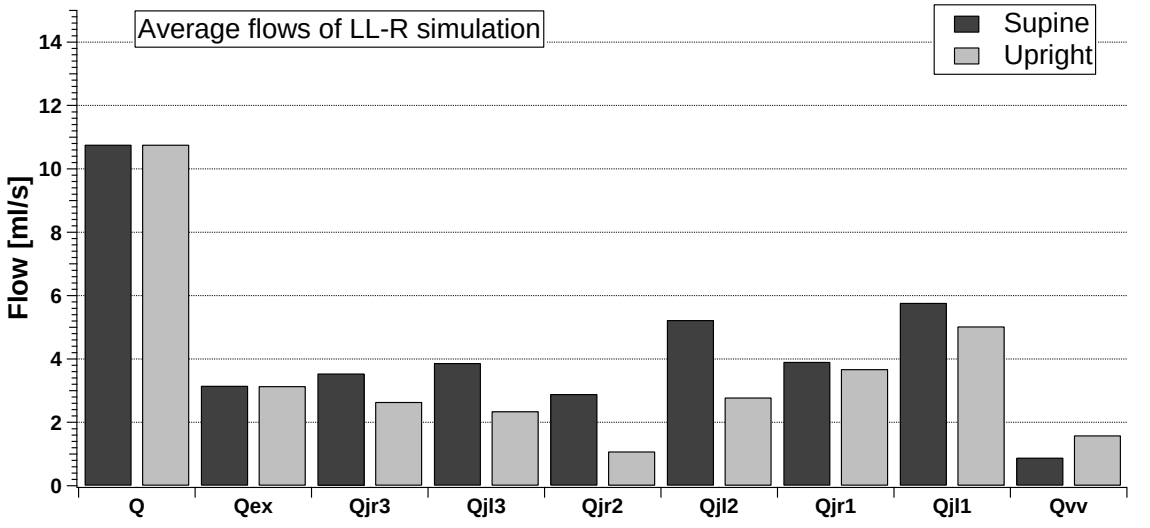

Figure 3.13: Model simulation of the cerebral, external, jugular (left and right), and vertebral average flows in the supine and upright condition for the LL-R ST group.

Q and Q_{ex} are not affected by the presence of stenosis. Thus, the cerebral autoregulatory mechanisms properly overcome the nonphysiologic conditions occurring downstream from the brain. Conversely, both LL-R ST and UL-L ST affect the outflow pathways. The vertebral system carries more blood than in the NST condition, also being comparable with some

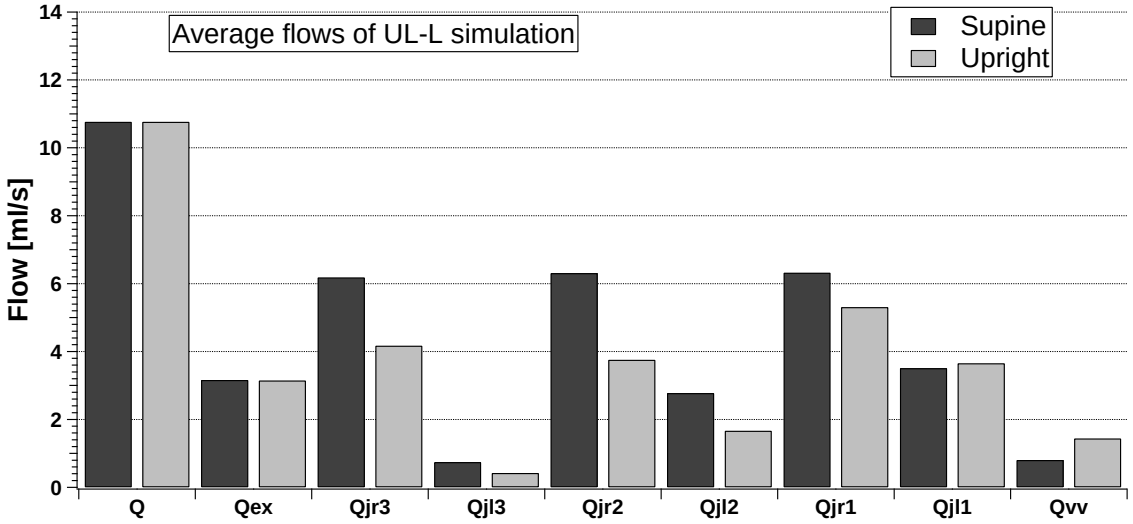

Figure 3.14: Model simulation of the cerebral, external, jugular (left and right), and vertebral average flows in the supine and upright condition for the UL-L ST group.

jugular segments. The left-right dominance is highlighted during simulation of the UL-L ST condition, while it is lost during simulation of the LL-R ST condition. The increase in the IJV average blood flow from J3 to J1 is now lost in the right IJV for a LL-R ST condition, and also for the right IJV of the UL-L ST, when in upright (with Q_{jr2} lower than Q_{jr1} and Q_{jr3}).

The model can simulate the variation of pressure as a function of time in every node of the hemodynamic circuit. One of the main consequences of a stenotic pattern on the intracranial equilibrium is a variation of pressure at the venous sinuses (P_{vs}), the link between the extracranial and intracranial circulation [15]. Changes in this quantity can affect other intracranial parameters and thus the overall brain physiology. Clinical evidence supports the results of increased pressure due to the occurrence of extracranial stenosis [121].

Figure 3.15 shows the temporal variation of P_{vs} due to the change of postural condition in different situations (NST, LL-R ST, UL-L ST, and total occlusion of IJVs at the J1 level, respectively).

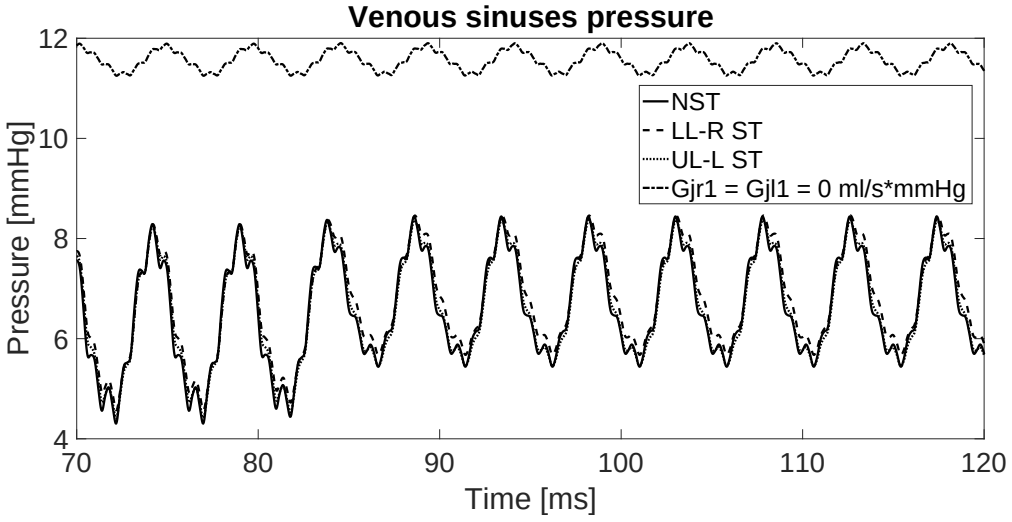

Figure 3.15: P_{vs} behavior over time in supine and upright simulations for different stenotic patterns.

With respect to Figure 3.5, we report here traces of P_{vs} for both simulation of healty and stenotic subjects. We choose to simulate stenosis like the one reported in [38] (see Section 2.3.1 Table 2.5 and 2.6), in order to verify the accordance between average experimental and simulated flow data. Moreover, we simulate a condition of total occlusion of the lower level of both IJVs as extreme stenotic condiion, as in [37].
There is no particular difference in P_{vs} values when a supine simulation is performed for the NST, LL-R ST, and UL-L ST cases (average range from 5.8 to 6.1 mm Hg). When they pass to upright, there is a slight increase in average P_{vs} (+0.7 mmHg). Conversely, P_{vs} markedly increases (from 5.8 to 11.8 mmHg) when a bilateral total obstruction occurs. The settling time for P_{vs} to reach a new equilibrium (not reported in the picture) can be quite different depending on the type of stenosis. In particular, it is shorter for the NST simulation (0.5 seconds), while it is delayed in case of stenosis (1.5 seconds for UL-L ST, 2 seconds for LL-R ST, and 30 seconds for the bilateral total occlusion case simulated).
Figure 3.16 shows the variation of P_{vs} while upright, in response to the standard heart action given in Figure 2.5, coupled with breathing (Figure 2.3) and the simulation of cycling exercise (see Figure 2.7) starting at $t = 80$ s till the end of simulation.

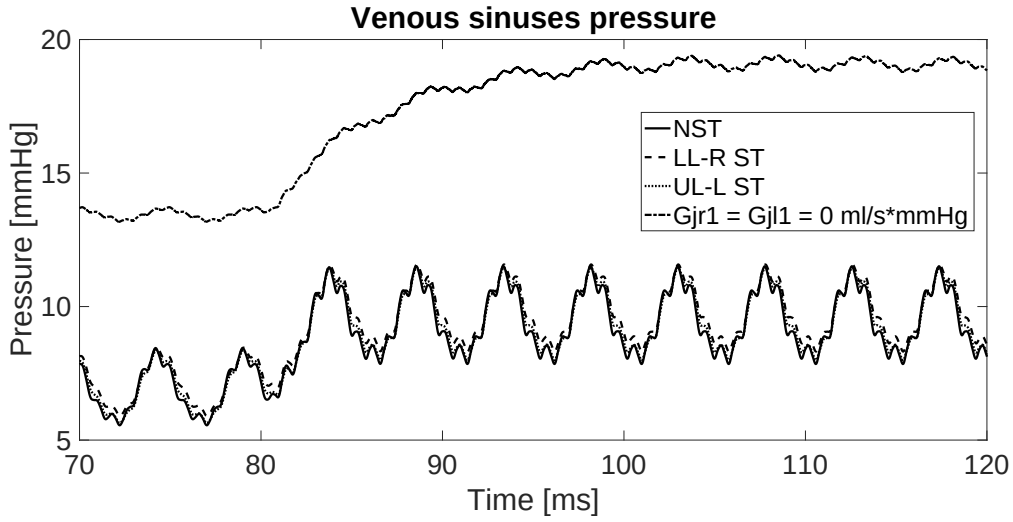

Figure 3.16: Particular of P_{vs} during simulation of cycling exercise, while breathing and upright. No tachycardiac effect is simulating. Various traces refer to P_{vs} when different stenotic patterns occur.

With respect to Figure 3.6, we report here traces of P_{vs} for both simulation of healhty and stenotic subjects. During upright posture (and after about 7 cardiac cycles, corresponding to 5 s, to reach equilibrium), P_{vs} oscillates between 5.4 and 8.4 mmHg around an average value of 6.8 mmHg, with a sinusoidal shape that reflects the respiration waveform of Figure 2.3. No remarkable difference appears for what concern simulations of the stenotic patterns reported in [38], with only a slight increase in the descending part of P_{vs} when obstruction of lower part of right IJV is simulated (LL-R ST simulation). In this case the minimum value of P_{vs} is 0.2 mmHg higher with respect healthy simulation or simulation of obstruction at the upper level of the left IJV (UL-L ST). Simulation of total obstruction at the lower level of both IJVs produces different results. P_{vs} needs around 30 s (not reported in the picture) to reach equilibrium. After that, it oscillates between 13.1 and 13.7 mmHg around an average value of 13.4 mmHg, with a less pronounced amplitude with respect to the previous cases.

Then, at t = 80 s, we start to simulate the cycling exercise (see Figure 2.7). Now, P_{vs} oscillates between 7.8 and 11.5 mmHg around an average value of 9.5 mmHg, with little differences in the sinusoidal shape at the level of details (i.e. change of sign of the first derivative). No remarkable difference appears for what concern simulations of the stenotic patterns reported in [38], with only a slight increase in the descending part of P_{vs} when obstruction of lower part of right IJV is simulated (LL-R ST simulation). In this case the minimum value of P_{vs} is 0.4 mmHg higher with respect healthy simulation or simulation of obstruction at the upper level of the left IJV (UL-L ST). Simulation of total obstruction at the lower level of both IJVs produces different results. P_{vs} needs around 30 cycles (corresponding to 24 s) to reach equilibrium. It oscillates between 18.8 and 19.4 mmHg around an average value of 19.0 mmHg, with a less pronounced amplitude with respect to the previous cases.
Figure 3.17 shows a particular of the waveform of P_{vs} while upright, in response to the standard heart action given in Figure 2.5 coupled with breathing (Figure 2.3).

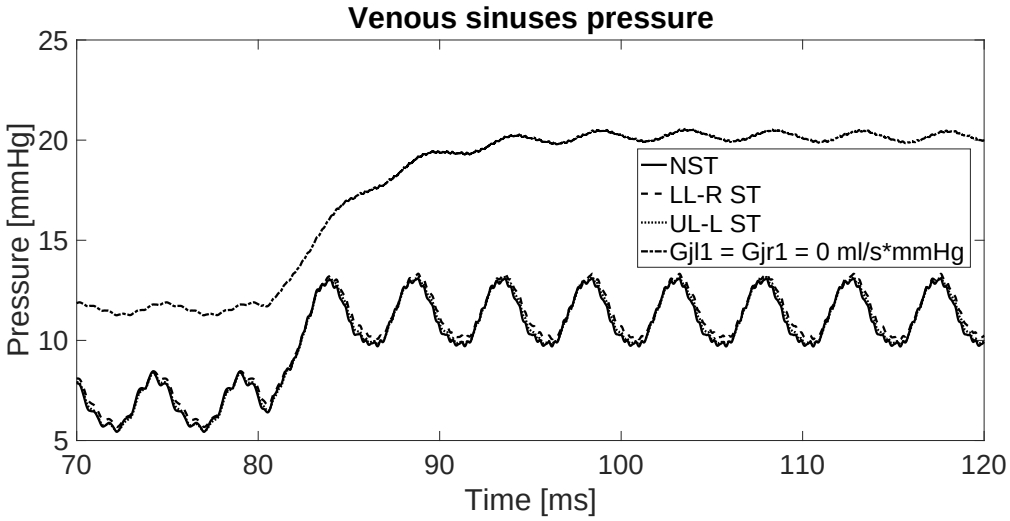

Figure 3.17: Particular of P_{vs} during simulation of tachycardia, while breathing and upright. No exercise effect is simulating. Various traces refer to P_{vs} when different stenotic patterns occur.

At $t = 80$ s we simulate tachycardia by doubling the frequency of the heart action till the end of simulation. With respect to Figure 3.7, here we report traces of P_{vs} for both simulation of healty and stenotic subjects. During upright posture (and after about 7 cardiac cycles, corresponding to 5 s, to reach equilibrium), P_{vs} oscillates between 5.4 and 8.4 mmHg around an average value of 6.8 mmHg, with a sinusoidal shape that reflects the respiration waveform of Figure 2.3. No remarkable difference appears for what concern simulations of the stenotic patterns reported in [38], with only a slight increase in the descending part of P_{vs} when obstruction of lower part of right IJV is simulated (LL-R ST simulation). In this case the minimum value of P_{vs} is 0.2 mmHg higher with respect healthy simulation or simulation of obstruction at the upper level of the left internal jugular vein (UL-L ST). Simulation of total obstruction at the lower level of both IJVs produces different results. P_{vs} needs around 30 cycles (corresponding to 24 s) to reach equilibrium. After that, it oscillates between 11.3 and 11.9 mmHg around an average value of 11.6 mmHg, with a less pronounced amplitude with respect to the previous cases.
Then, at $t = 80$ s, we start to simulate the tachycardia. Now, P_{vs} oscillates between 9.7 and

13.0 mmHg around an average value of 11.4 mmHg, with little differences in the sinusoidal shape at the level of details (i.e. change of sign of the first derivative). No remarkable difference appears for what concern simulations of the stenotic patterns reported in [38], with only a slight increase in the descending part of P_{vs} when obstruction of lower part of right IJV is simulated (LL-R ST simulation). In this case the minimum value of P_{vs} is 0.4 mmHg higher with respect healthy simulation or simulation of obstruction at the upper level of the left IJV (UL-L ST). Simulation of total obstruction at the lower level of both IJVs produces different results. P_{vs} needs around 30 cycles (corresponding to 24 s) to reach equilibrium. It oscillates between 19.8 and 20.4 mmHg around an average value of 20.1 mmHg, with a less pronounced amplitude with respect to the previous cases.
We report in Figure 3.18 a histogram to show how P_{vs} varies when stenotic patterns occur.

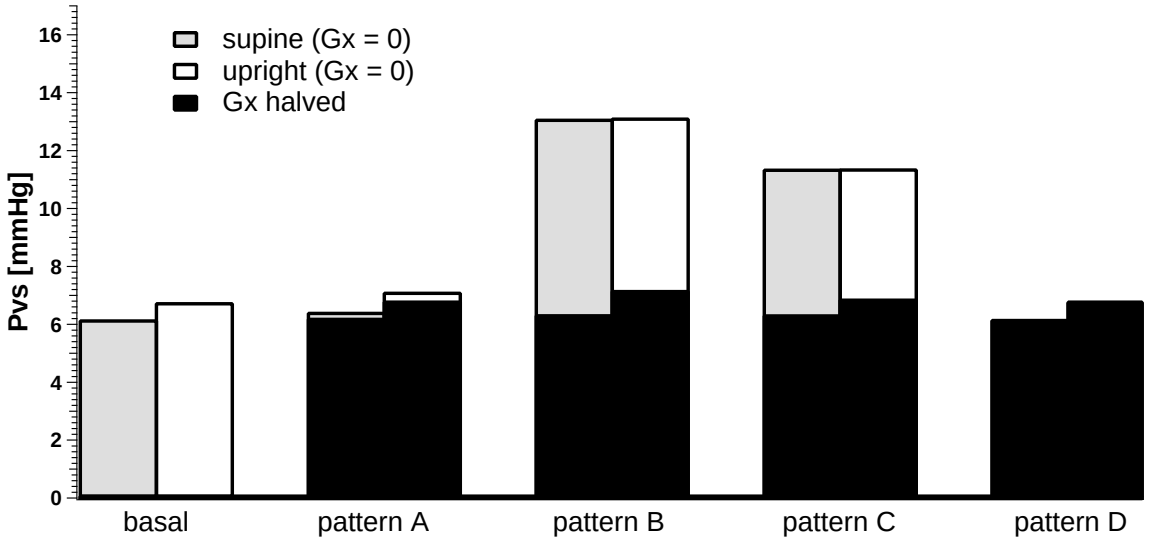

Figure 3.18: P_{vs} for simulations of healthy subject and stenotic patterns described in [120]. The black columns represent the simulation of stenotic patterns with halved conductances with respect to the basal values.

Together with the simulations of null conductance, we reported also the simulations of the same patterns but with halved conductances. We chose to simulate total and halved occlusions of more than one drainage tract at the same time, following the typical patterns reported in literature [120]. Pattern A refers to simulation of obstruction of the proximal azygos $azy2$, associated with a closed stenosis of the left IJV. Pattern B refers to simulation of obstructions of both the IJVs and the proximal azygos. Pattern C refers to simulation of obstructions of both the IJVs but without stenoses in the azygos system. Finally, pattern D refers to simulation of obstructions in different tracts of the azygos vein ($azy1$ and $azy2$) associated with occlusion of the lumbar vein.
Results show that two particular pathological patterns (i.e., patterns B and C) may have a strong effect on P_{vs}, which reaches values as high as 11 - 13 mmHg both in supine and upright positions. Such value may have consequences on intracranial pressure, cerebrospinal fluid circulation, and cerebral tissue. However, this pressure increase occurs only if the stenotic lesions are very severe (conductances close to zero). Moderate levels of conductance changes, although multiple, cause more acceptable pressure rises.
Therefore, the application of the model demonstrates a significant increase in P_{vs} for type B

and C but not in patterns A and D. Such a result appears to be coherent with the clinical severity and/or the topography of multiple sclerosis, the neurological disease associated with the observed patterns of venous obstruction in this cohort of patients. As far as the severity is concerned, patients with type A pattern (characterized by reduced sinusal pressure) demonstrated, with respect to B and C patterns, a significantly reduced probability to worsen to the secondary progressive clinical stage [120]. Regarding the topography of the lesions in the central nervous system, type D pattern exhibits few cerebral lesions and prevalent MRI plaque dissemination in the spinal cord [120]. Speculatively, this result suggests that increased pressure in the cerebral sinuses may clinically influence either the disease progression or the topography of multiple sclerosis plaques and warrants further studies in this direction. The present simulations suggest two important considerations:

- the cerebral venous return system is quite robust: a single occlusion, or even multiple occlusions of moderate entity, can induce only mild changes in P_{vs} and in total blood flow. Indeed, this is the fundamental role of the strong anastomotical connections incorporated in the model;
- pathological states, characterized by multiple severe obstructions, can lead to significant pressure changes in the venous sinuses, hence, in possible alteration in cerebrospinal fluid circulation and brain tissue pressure.

Chapter 4

Development of a device for the study of cerebral venous outflow

The purpose of this chapter is to describe a new plethysmography device for the study of cerebral venous outflow in humans.
Details of the device and the first experimental protocols for data acquisition are reported below, while first experimental data and related analysis of the results are reported and discussed in Chapter 5.

4.1 Introduction

In the human circulatory system, arteries and veins act together to carry blood to and from organs and tissues. With respect to arteries, that are similar to rigid tubes with negligible compliance, veins can exhibit a remarkable elasticity. We can compare veins to a balloon that changes its size and section with respect to the amount of blood filling it and the pressure suffered at the walls [36]. Indeed, this elasticity has a considerable effect with respect to the gravitational gradient suffered during change of posture, or after a generic change of direction of the vein lumen with respect to the gravitational axis. To understand the governing laws of these elastic veins is interesting and can give more insight on the mechanisms at the basis of blood drainage. Focusing on the brain drainage, it is important to analyze the behavior of the internal jugular veins (IJVs), that mainly contribute to the blood outflow from braincase (see Figure 2.1) [7, 19, 89, 91, 111, 116, 119, 128].
The jugular venous pulse (JVP, Figure 4.1) is one of the main parameters of cardiac status and is used by cardiologists as a heart-failure parameter. [9, 20, 27].

It carries information about physiological status of the heart and possible changes due to loss of functionality, and it is also an index of the time variation of the blood volume in the IJV. Blood flow and pressure variations due to to the filling of the right atrium produce pulsations on the main veins, that are trasmitted through peripherals veins [73]. These pulsations at the level of IJV produce the so called JVP, that can be detected in a non invasive way because IJVs are superficial veins, not protected by bone or cartilage tissues [78]. It has been suggested that the JVP can be used to investigate IJV drainage function and to obtain valuable information about cardiac hemodynamics through the analysis of its waveform [98].

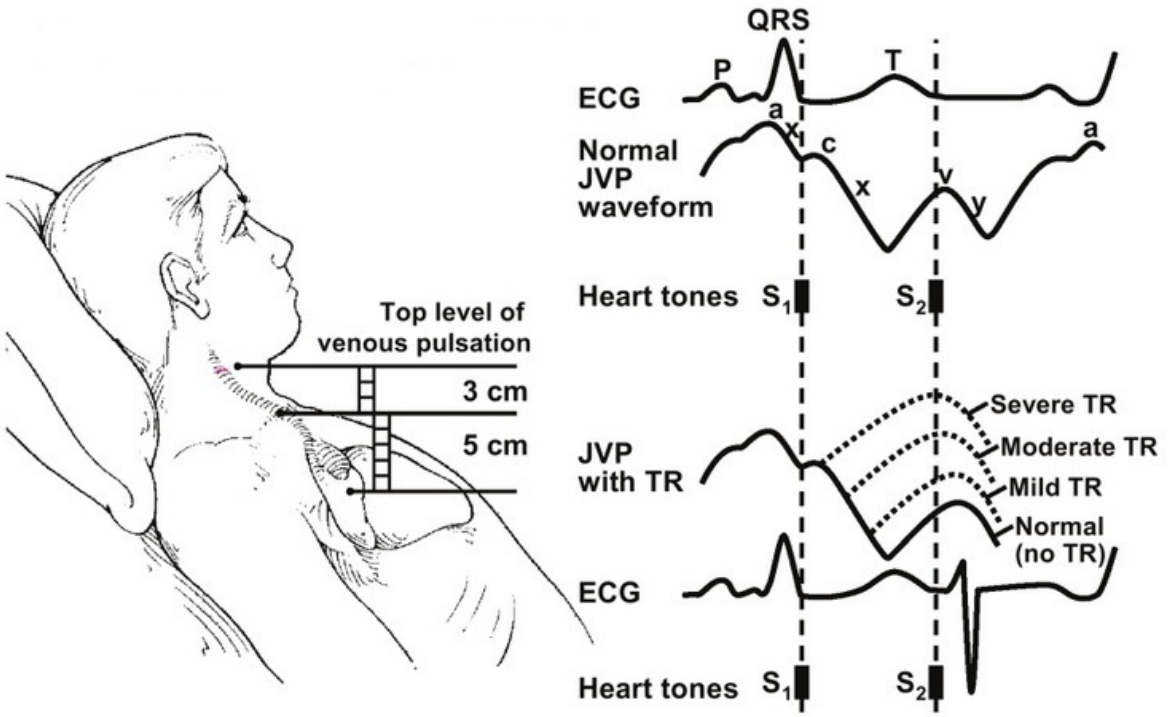

Figure 4.1: Jugular venous pulse (JVP) waveform for healthy (top) and tricuspid regurgitation (TR, bottom) case, with corresponding electrocardiogram (ECG).

The JVP technique was first studied by means of a polygraph to found the presence of three waves known as a, c and v [62] . The JVP diagrams were related to various pathologies and in the study of the relationship between the a, c and v waves and the cerebral venous return (CVR) venous return [61].
In this thesis, the CVR has been non invasively characterized by means of a novel application of strain gauge plethysmography which uses capacitive sensors [124]. Thanks of its easy portability, small footprint, and non invasiveness, the proposed device can be considered as an ideal tool for research on this field. Indeed, we used it on the so called Drain Brain project, a series of experimental sessions both on Earth and aboard the International Space Station (ISS). The aim of the Drain Brain experiment [72], sponsored by the Italian Space Agency (ASI), was to monitor CVR of an astronaut before, during, and after a space mission aboard the ISS, so as to study the compensatory mechanisms that facilitate this essential physiological action in subjects living in a microgravity environment.
Thanks of its low cost of production, easy of use, and effectiveness in detecting time variations of a given cross section of the human body such as neck, wrist or ankle, it can be considered as a useful screening device for vascular diseases.

4.2 Description of the device

The proposed device is a novel application of strain gauge plethysmography useful to characterize CVR [124].
Plethysmography is a well known technique for recording volume changes in a tissue. When the volume change occurs through only a blood volume variation in the tissue, information

regarding the tissue blood flow can be obtained by plethysmography [104]. In our application, such technique measures variations in electrical parameters associated with changes in blood volume, recorded through a sensor encircling any cylindrical segment of the body. Our plethysmography system uses capacitive sensors for which the capacitance increases when stretched (Figure 4.2).

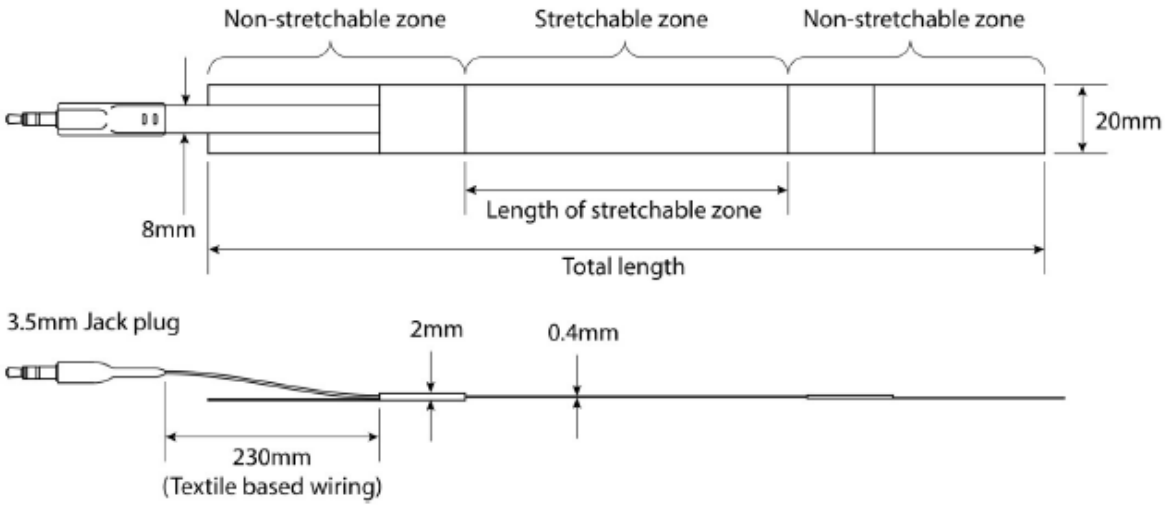

Figure 4.2: Design and outline dimensions of the Danfoss PolyPower capacitive sensor.

We also refer to capacitive sensors as strain gauge, because we use its elongation from a basal value to detect variations in time of the perimeter of a given anatomical section (e.g. the neck).

The strain gauge sensors used here are capacitors charged with constant current, connected to two comparators and a logic port. Comparators generate a signal in time that depends on the received voltage and is stored by the plethysmography sistem. At any elongation corresponds a voltage and so an amount of electric charge stored on the capacitor. The signal is converted in a count number, that is used in calibration equations (see Figure 5.2 and 5.3) to calculate the elongation with respect to time. In this thesis we will show data from measurement performed at the neck level with two sensors of different length (35 and 38 cm). We refer to these sensors as short and long, respectively.

The sensors used are thin and elastic, suited to adhere to the skin and record the perimeter variation of the examined anatomic part. They have non stretchable zones at both ends for attachment and a highly stretchable zone being the active part. The output signal represents the elongation of the stretchable zone. The maximum displacement of a sensor is 80% of the length of its stretchable zone (equivalent to 80 % strain). The construction of the sensor is such that in the stretchable zone, a double layer of sensor material is used to make a capacitor with the 2 inner electrodes in the middle and the two outer electrodes on the outside of the sensor. The single layer PolyPower dielectric electro active polymer (DEAP) material is based on a thin film of elastomer material. The elastomer material is a silicone of the type polydimethylsiloxane (PDMS) which is a soft material having high dielectric field strength. The basic PolyPower material has a special micro structured design on the front surface and a flat back (referred to as single layer film material). This single layer film material is used for electrical isolation or as elastomeric film. To get a DEAP material that can be activated, a thin metal electrode layer is deposited on top of the corrugation on the front surface of the

single layer film material. Given the micro structured surface, the metal electrode is compliant in one direction across the length of the film web while stiff in the perpendicular direction. The area of the laminated film where the elastomer material is between two electrodes is referred to as the active area [25]. The outer coating of the sensor is made of transparent silicone rubber. For mounting purposes, the sensor is supplied with attachment zones in the two opposite ends. The outer 25 mm at the end of each sensor is a layer of non woven textile to be used for sewing velcro stripes useful to close the sensor around a given anatomical section.
The sensor is supplied with a flexible textile based cable with a 3.5 mm jack plug. It is electrically connected to a portable electronic unit (PEU, see Figure 4.3) to record changes of blood volume over time.

Figure 4.3: Portable electronic unit (PEU). This unit allows the connection of three different capacitive sensors, Li-ion battery or external power supply, SD card for data storage and serial cable for the transmission of the acquired data.

The PEU is in a vented container and it can be fixed at the waist of the subject performing the test through a non removable Nomex ® belt as in Figure 4.4, that shows PEU and two of the sensors connected to neck and forearm.

Data acquisition and storage are performed by a custom electronic board that has been developed by the medical physics group at the University of Ferrara in cooperation with the local section of the INFN (Istituto Nazionale di Fisica Nucleare), Italy. The plethysmography system integrates an electronic circuitry that is able to collect data from three strain gauge sensors like the one reported in Figure 4.2. These feature allows the device to collect data on three different anatomical districts at the same time. It is possible to check all the signals in real time by using the LabVIEW interface of Figure 4.5, also developed in our laboratories.

Calibration of the strain gauge sensors was performed before to acquire data, following the protocols described in Section 5.2, to check the linear response of the system to elongations and to calculate the calibration curves so as to convert raw data in unit of length.

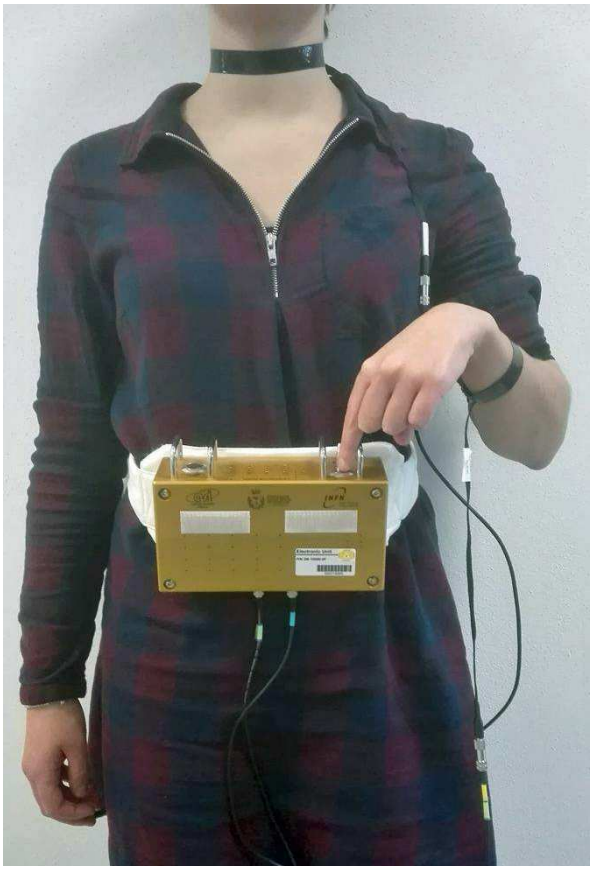

Figure 4.4: Plethysmography system fixed at the waist of the subject. Arm and neck sensors are connected to the PEU.

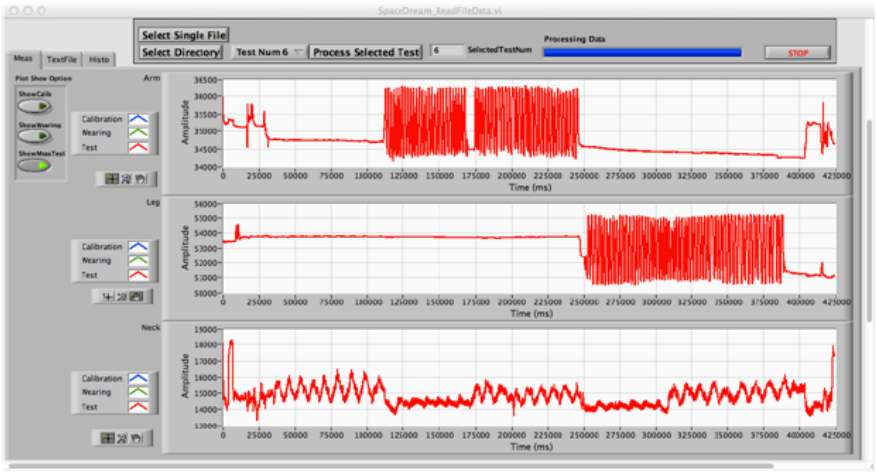

Figure 4.5: LabVIEW interface of the plethysmography device. When PEU is connected to user interface through serial cable, the user can check signal from up to three sensors over time. The same interface allows to save data for further analysis.

4.3 Experimental protocol

The sensors we used are suitable to be applied at arm (close to the wrist), leg (close to the ankle) and neck. Here, we will focus on data recorded by the neck sensor, so as to analyze brain outflow in relation to physiological variations such as respiration and posture.

4.3.1 Laboratory protocol

The plethysmography device dedicated to measurement on Earth has some differences with respect to the one used for the Drain Brain protocol of Section 4.3.2:

- real time acquisitions allowed (serial cable for the transmission of the acquired data);
- possibility of external power supply;
- sampling frequency up to 83 Hz.

Calibration is performed to assess the efficiency of the strain gauge sensors, to find out the range of extension where the response is linear with elongation, and to obtain the equations to convert counts in unit of length (see Figures 5.2 and 5.3).
It is important to properly apply the sensors to the anatomical districts we want to analyze. To acquire reliable data from the neck, sensors must be placed at the same position (e.g. just above the clavicles) and adherent to skin, with the subject sitting. After the application to the selected anatomical district, we connect sensors to the PEU, and all the system to the user interface. Then, the subject lies supine with arms close to the body and straight legs. Four subjects were analyzed by using a protocol consisting in five different postures:

- supine;
- sitting with arms close to the body;
- upright;
- bent with arms pointing the feet;
- simulation of walking.

There is a time interval of several minutes among acquisitions on different postures, in order to allow body fluids and vital parameters of the subjects (heartbeat, breathing) to reach a new equilibrium after the postural change. Subjects were always helped during the postural changes, to minimize muscle tension. After reaching a new posture, we wait around 30 seconds to avoid noise due to swallow, coughing or muscle activity. Beside measurements on different postures, we collected data at different neck sections (i.e. at different points of the IJVs). We repeated the above protocol in different days. Every session was performed in around 1 hour, in order to avoid as much as possible physiological changes not related to the postures under examination.

4.3.2 Drain Brain protocol

Concerning the Drain Brain experiment (performed aboard the ISS and before and after the mission), plethysmography acquisitions were carried out by measuring the variation of the circumference of neck, calf of the leg, and forearm under different respiratory conditions.
Basal spirometry was used to change such respiratory conditions. The Pulmonary Function System (PFS), which is also available on the ISS, was used for the spirometry. Moreover, simple physical exercises, like opening and closing a hand, were performed by the astronaut during such measurements. The experimental protocol performed by the astronaut is summarized by the following steps:

- left arm exercise during normal breathing;
- left arm exercise during forced breathing;
- left leg exercise during normal breathing;
- left leg exercise during forced breathing.

The arm exercise consists of approximately 30 movements of the left hand, i.e. open/close, while the leg exercise consists of approximately 30 movements of the left ankle, i.e. flex/point. Normal and forced breathing are periodic respirations monitored by using the spirometer that is calibrated before starting the protocol. Normal breathing refers to the air flux measured during a standard respiratory cycle of the subject, while forced breathing refers to the air flux when the subject reaches the 70% of own vital capacity. The whole protocol is performed twice for each experimental session, the first one in the morning and the second one in the afternoon (the time interval is in the range 6-8 hours).
Data on Earth before and after the sessions aboard the ISS have been collected with the same subject in both upright and supine positions.
The plethysmography device dedicated to the Drain Brain protocol has some differences with respect to the one used for measurement on Earth of Section 4.3.1:

- data are stored in a SD card for offline analysis;
- non rechargeable Li-ion batteries to provide power supply to the instrument;
- sampling frequency is fixed to 16 Hz.

Chapter 5

Experimental validation of the plethysmography device

5.1 Offline data analysis method

To analyze the plethysmography traces we used both Fourier and Discrete Wavelet Transform (DWT) [22]. The main difference is that results of Fourier transform are only localized in frequency, while results of wavelet transform are localized in both time and frequency [96]. Fourier transform was used to analyze the frequency content of signals provided by the sensors and the contribution of every detected frequency to the amplitude of the whole signal [76]. Wavelet analysis was used to highlight the contribution of a given range of frequencies to the whole signal, by plotting data (filtered in a specific range of frequencies) in amplitude vs. time.
Therefore, a filtered time-scale representation of digital signals from strain gauge sensors is obtained using digital filtering techniques. The frequencies that are most prominent in the Fourier spectra of a given signal will appear as high amplitudes in that region of the DWT signal that includes those particular frequencies. The frequency bands that are not very prominent in the original signal will have very low amplitudes, and that part of the DWT signal can be discarded without any major loss of information. The filtered data are handled in order to highlight the contribution due to heartbeat (expected to have a main frequency at around 1 Hz) and breathing (that contributes at around 1/8 Hz because of the pulmonary function control performed through spirometry).
As an example, two raw plethysmography traces were reported in the top plot of Figure 5.1, together with their Fourier Transform (middle plot) and DWT filtered curves that show the heart and respiratory contribution to the raw signals (bottom plot). Signal processing to remove the respiratory trend from plethysmography data has been applied to all results presented in the following.

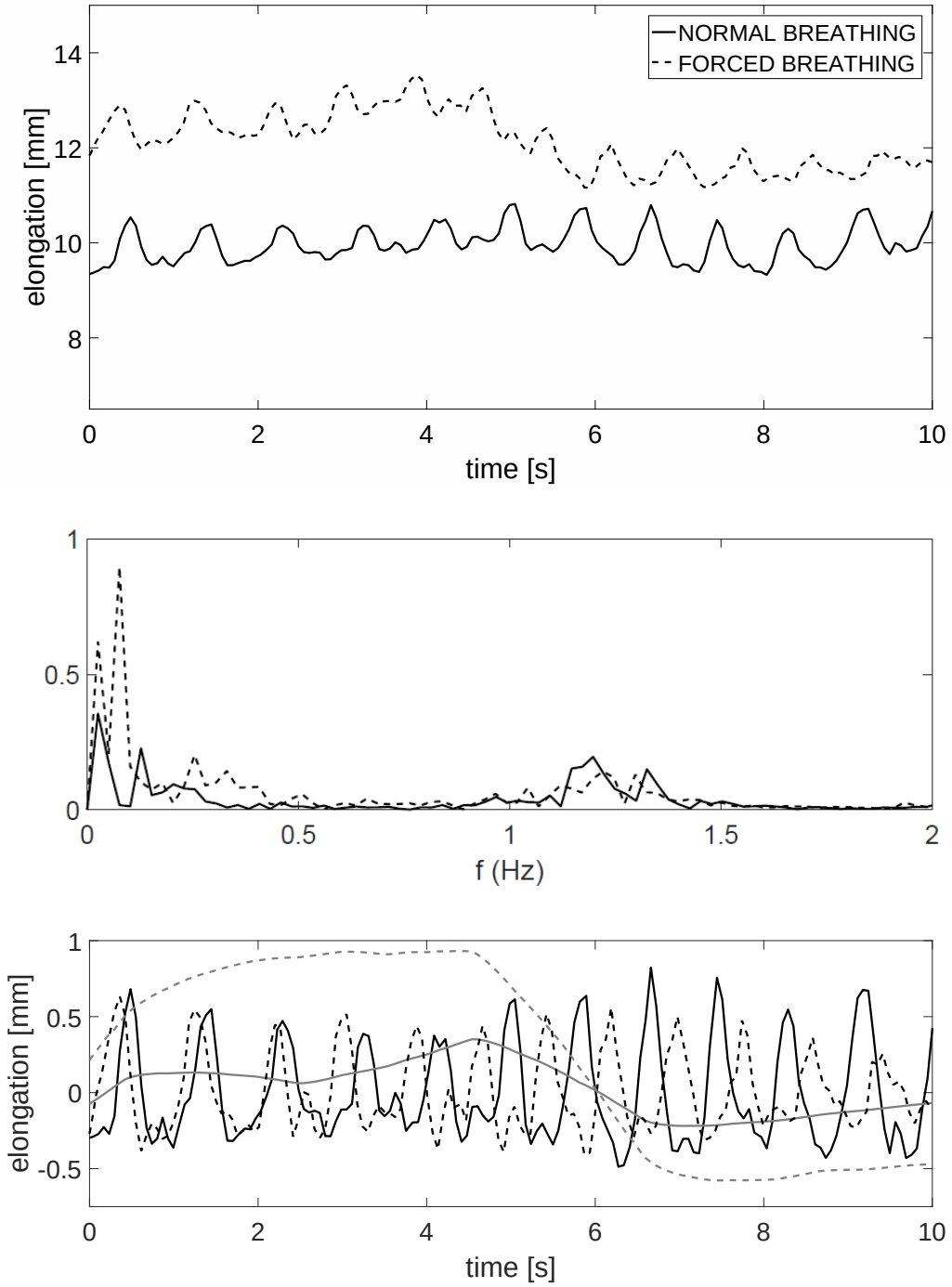

Figure 5.1: Top: Particular of two plethysmography curves acquired with subject breathing normally (solid line) and deeply (dashed line), during an experimental session. Middle: Frequency spectra of the plethysmography curves. Bottom: Particular of the filtered traces to highlight the cardiac (black curves) and respiratory (grey curves) contribution to the original signal.

5.2 Experimental results

Data obtained during the experimental session described in Section 4.3.1 were stored as a .txt file through the LabVIEW interface.
Data from Drain Brain project described in Section 4.3.2 were stored in a SD card. The initial part of all the acquired traces was removed to avoid the noise that eventually occurs during first part of the acquisition.

5.2.1 Experimental results of laboratory protocol

First of all, calibration curves are obtained through a controlled step by step elongation of the strain gauge sensors. For a given elongation, we acquired the corresponding average count with standard devation in time. These values are used to obtain the experimental shown in Figures 5.2 and 5.3, where we reported the count in the y-axis, and the corresponding elongation in the x-axis.

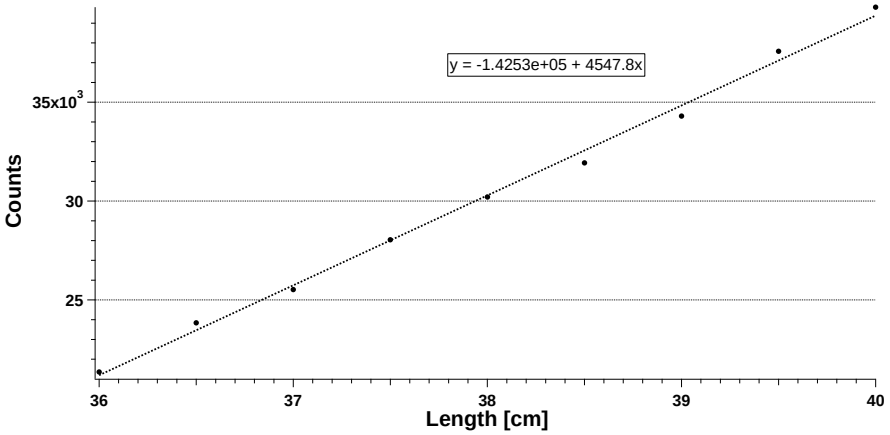

Figure 5.2: Calibration curve for the short sensor. Horizontal axis reports the length of the sensor in cm, vertical axis reports the corresponding response of the device in counts.

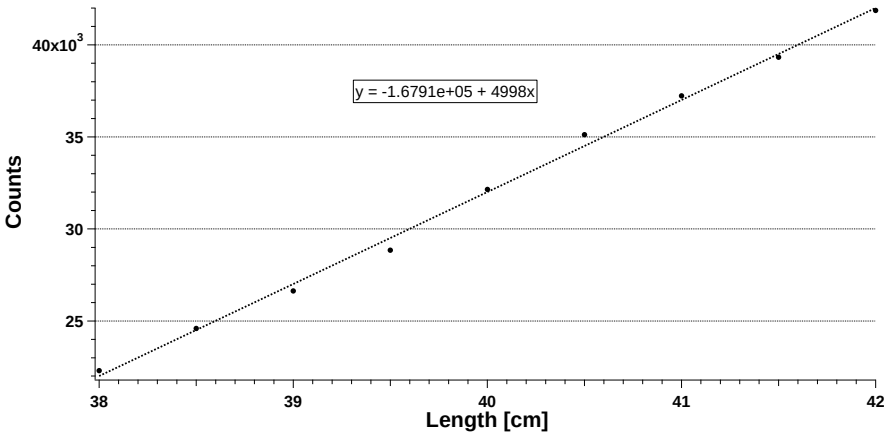

Figure 5.3: Calibration curve for the long sensor. Horizontal axis reports the length of the sensor in cm, vertical axis reports the corresponding response of the device in counts.

We calculate the best linear equation ($y = mx + q$) for every plot, together with the R^2 parameter. R^2 is close to 1 for all the sensors used, so the linear response of the strain gauge sensors is guaranteed.

In this section we present results and comparisons about the following acquisitions:

- comparison between measurement from different subjects with different strain gauge sensors, to check differences in system response due to changes in the setup;
- comparison berween data acquired with one strain gauge sensor in several neck sections of a given subject, in different postures;
- comparison between data acquired on a subject with different strain gauge sensors in several experimental sessions;
- comparison between data acquired on a subject in several postures with one strain gauge sensor, to check the differences on brain drainage system due to postural change.

In general, only a fraction (usually 10 seconds) of the whole plethysmography trace is reported. Fourier spectra presented here range between 0 and 5 Hz only, being the contribution of higher frequencies negligible.

Comparison among different subjects

Figure 5.4 shows two plots, referring to supine (left) and sitting (right) posture of three subjects.

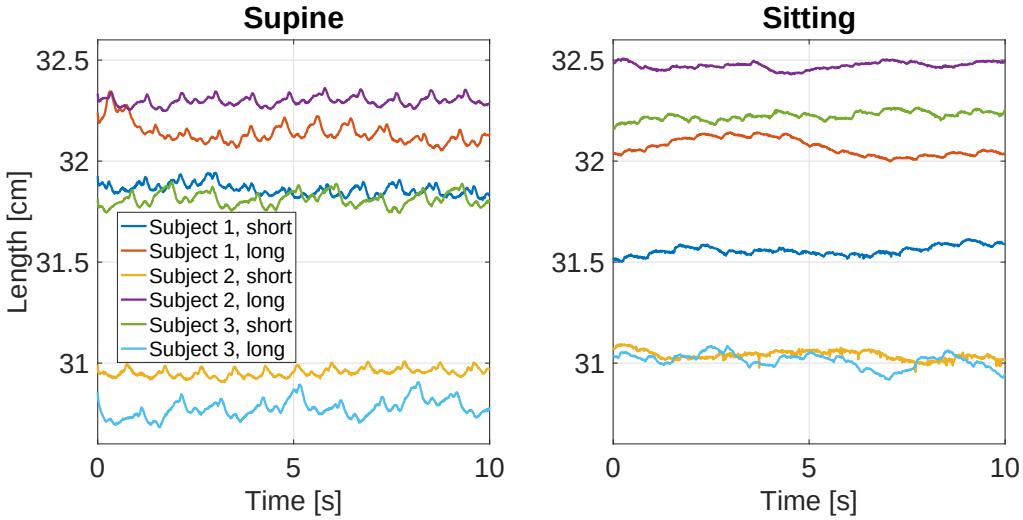

Figure 5.4: Plethysmography traces of subjects 1, 2, and 3, in supine (left) and sitting (right) posture. Data were acquired with both neck sensors.

From left plot of Figure 5.4 we can see six plethysmography traces with marked periodic signals due to cardiac pulsations. Average values of such traces range between 30.8 cm and 32.3 cm, in agreement with the neck perimeter measured before the acquisitions. We also note that:

- amplitude of periodic variations in subject 3 is higher with respect to others;
- there is a trend on traces of subjects 1 and 3, with lower frequency compared to the perturbation due to cardiac activity.

Observation of a marked jugular pulsation could be an effect of a different compliance of veins for subject 3, or perhaps a particular prominence of IJVs of this subject and/or a thinner layer of soft tissues between veins and sensor. Another possible cause of this difference could be a different heart pressure. The linear trend observed on subjects 1 and 3 is due to respiration. Traces of subject 2 does not present such low frequency trend, probably because sensors were applied far from clavicle, and so far from the zone where effect of breathing is preminent. For all the traces the average contribution of the cardiac pulsation is around 1 mm.
The right plot of Figure 5.4 shows traces with different behavior:

- no cardiac waveform is distinguishable;
- all traces (apart from the one referring to subject 2 wearing short sensor) shows average value shifted with respect to the left plots (i.e. different neck perimeter with respect to supine position);
- contributions at high frequencies are discernable.

As already discussed, the sitting position affects the configuration of IJVs. Hydrostatic pressure gradient due to the gravitational field provokes a decrease in jugular compliance. Therefore, the jugular pulsation must change, as reflected in the different beahvior of the plethysmography traces. Being the contributions due to cardiac pulsation almost negligible, small contributions due to electric noise or random muscle activity arise. Muscle contribution may also explain dissimilarity among length of neck perimeter observed in supine and sitting positions.

Figures 5.5 and 5.6 report the Fourier transform of traces reported in Figure 5.4.

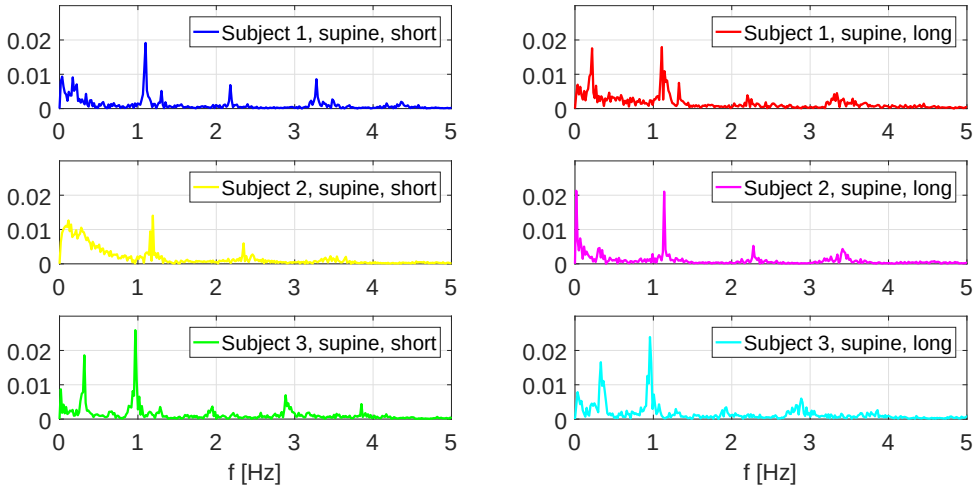

Figure 5.5: Fourier spectra of plethysmography traces reported in Figure 5.4 left (three supine subjects).

In all the spectra we can recognize several peaks of different amplitude:

- the main peak at around 1 – 1.5 Hz;
- a secondary peak below 0.5 Hz;

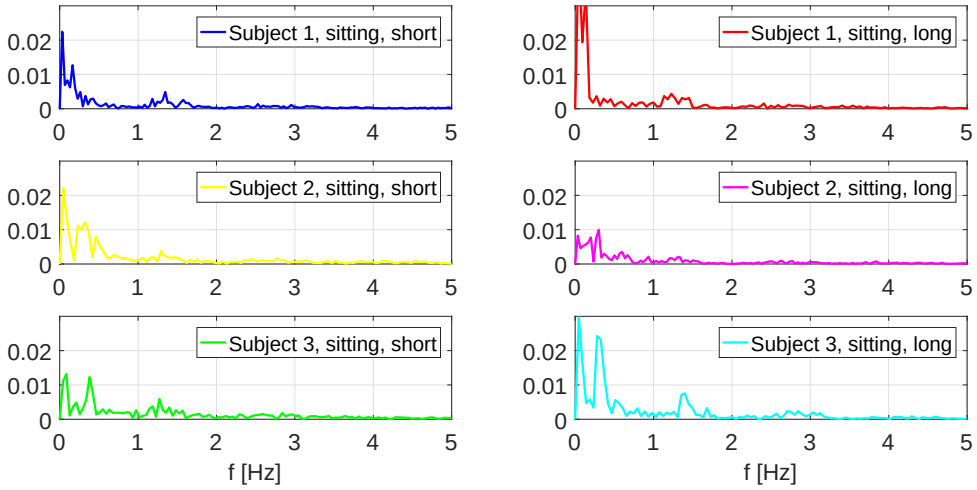

Figure 5.6: Fourier spectra of plethysmography traces reported in Figure 5.4 right (three sitting subjects).

- some minor peaks between 2 Hz and 3 Hz.

The first peak is due the cardiac oscillations and all the related effects (i.e. it can be associated to the jugular venous pulse). The second peak is the breathing contribution, while it seems reasonable to attribute the high-frequency peaks to harmonics of the cardiac oscillations because they occur almost exactly at the multiples of the fundamental frequency. Therefore, we can see from experimental data reported in Figure 5.4 that the plethysmography device is an useful system to detect in a non invasive way variations in neck perimeter due to phenomena related to circulation in general, and CVR in particular. Moreover, being the supine and sitting wafeform markedly different, it is an useful tool to recognize the effect on circulation due to change of posture.

Comparison among different jugular segments

Figure 5.7 shows plethysmography traces of subject 2 in supine (left plot) and sitting (right plot) position, collected at different sections of the neck.

Looking at the left plot (supine acquisition), we can see differences in the average value of the neck perimeter at different levels. In particular for this subject we have a neck perimeter equal to:

- 36.6 cm at the J1 level;
- 35.8 cm at the J2 level;
- 36.8 cm at the J3 level.

Plethysmography trace collected at the lower level (J1) shows a respiratory component, as we expected because of the proximity to the pulmonary system. All the acquisition shows a waveform related to the cardiac effects. In addition, we notice a contribution from higher frequencies in the acquisition at the middle level (J2).
The right plot of Figure 5.7 shows that in sitting position the average value of neck perimeter is equal to:

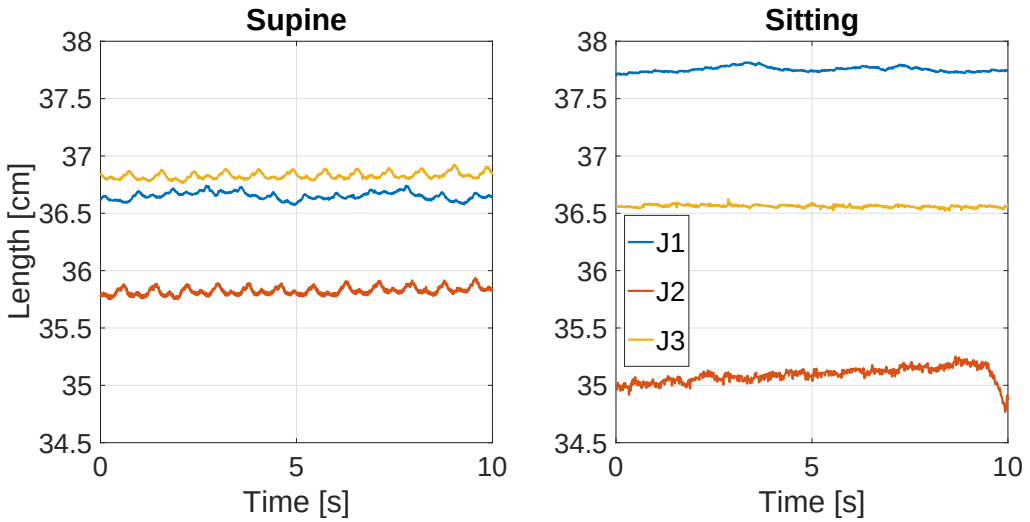

Figure 5.7: Plethysmography traces of subject 2 in supine (left plot) and sitting (right plot) position. Blue line (J1) refers to the acquisition at the lower level, close to the clavicle bones, while red and yellow lines refer to the acquisition at the middle (J2) and upper (J3) level, respectively.

- 37.7 cm at the J1 level;
- 35.0 cm at the J2 level;
- 36.6 cm at the J3 level.

With respect to the supine acquisitions (left plot, where upper level J3 is the neck level with the larger perimeter), in sitting position the lower level J1 has the largest circumference. This unexpected result is a side effect of the non invasive measurement we are performing, that takes into account all the variations in the muscle tone, other than vascular changes. In this plot the amplitude of the waveform associated to cardiac contribution is negligible with respect to acquisitions in supine. Figure 5.8 shows 60 seconds of the same plethysmography traces already reported in Figure 5.7.

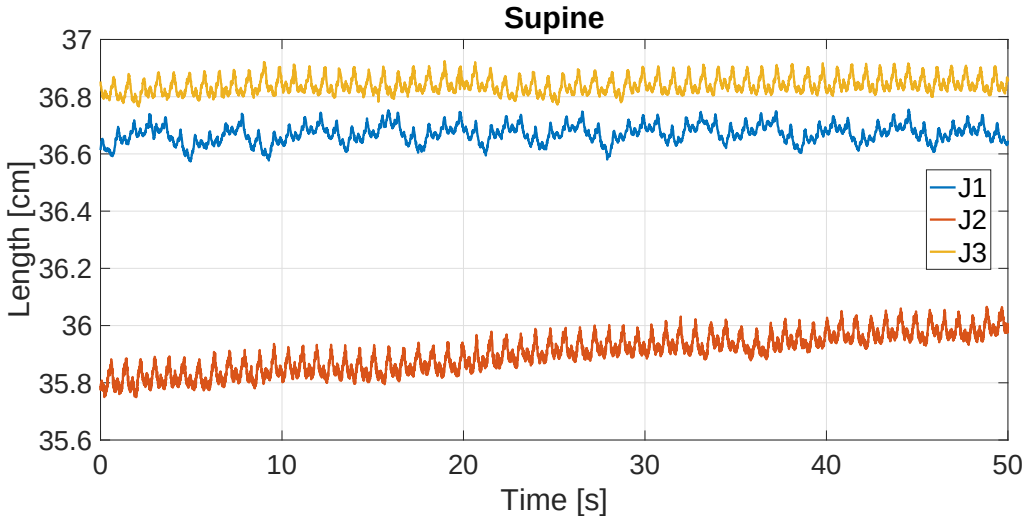

Figure 5.8: Plethysmography traces of subject 2 in supine position. Blue line (J1) refers to the acquisition at the lower level, close to the clavicle bones, while red and yellow lines refer to the acquisition at the middle (J2) and upper (J3) level, respectively.

Looking at this plot,we recognize a linear trend inside the acquisition at the J2 level, probably due to some temporary electronic or mechanical disturbance of the device.
Figure 5.9 shows the Fourier transform of the traces reported in Figure 5.8.

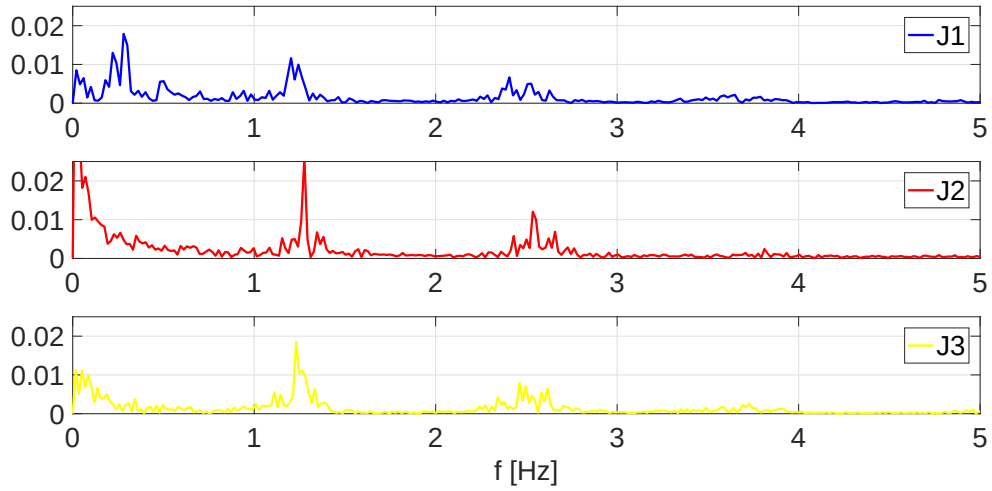

Figure 5.9: Fourier spectra of plethysmography traces reported in Figure 5.8 (subject 2 in supine position). Blue line (J1) refers to the acquisition at the lower level, close to the clavicle bones, while red and yellow lines refer to the acquisition at the middle (J2) and upper (J3) level, respectively.

All the spectra show a main peak at around 1.2 Hz associated to cardiac pulsation. Such peak is more prominent for the acquisition at the middle (J2) level. Minor peaks are detectable at around 2.5 Hz and close to 0 Hz.
Figure 5.10 shows data of subject 2 when supine, filtered by using wavelet transform.

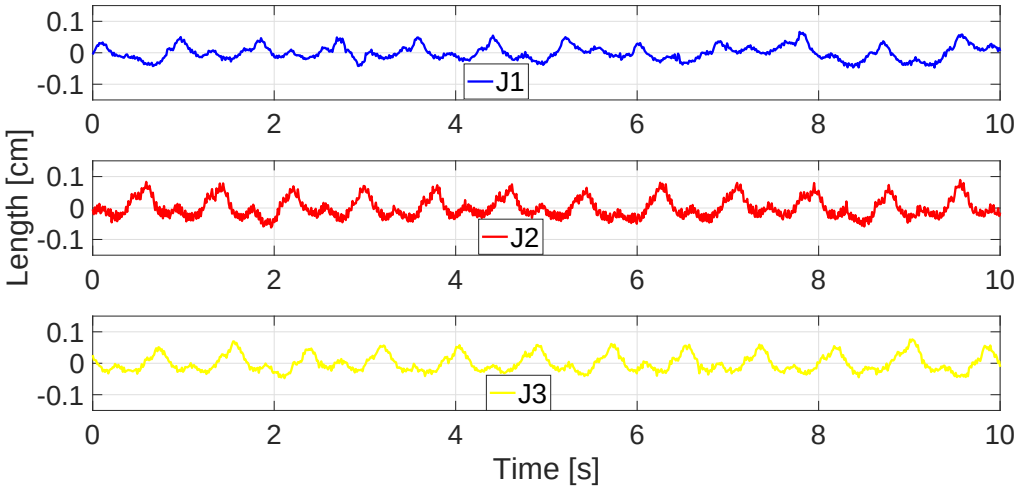

Figure 5.10: Filtered plethysmography traces of three neck sections (J1 in blue, J2 in red, J3 in yellow) of subject 2 in supine position. Data filtering removed the average value of every acquisition and all the contribution below 0.3 Hz.

We notice that filtering the data with a high-pass filter (all frequencies below 0.3 Hz are removed), the linear trend of the J2 trace disappears, together with all the contributions due to breathing. In Figure 5.11 we can see the Fourier spectra of experimental data reported in Figure 5.10.

Data filtering removed all the contribution below 0.3 Hz detectable in Figure 5.9.

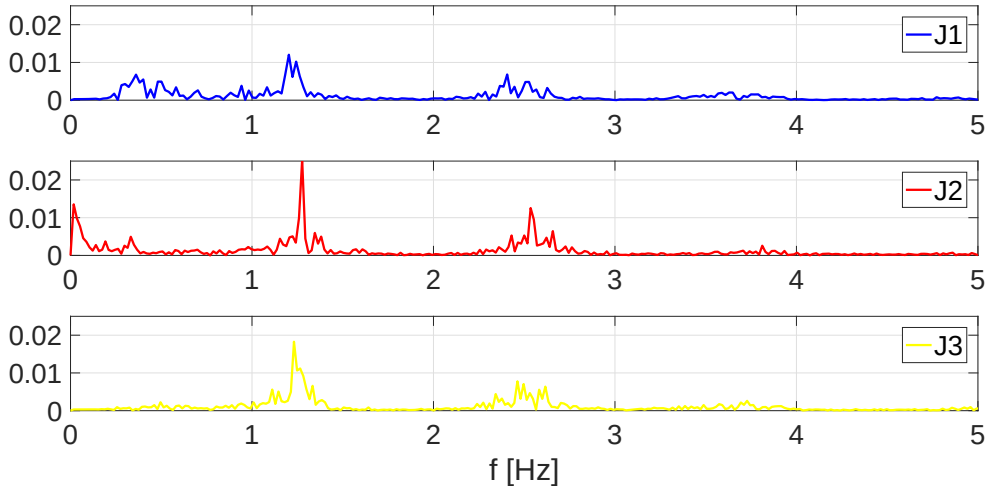

Figure 5.11: Fourier spectra of filtered plethysmography traces reported in Figure 5.10 (subject 2 in supine position). Blue line (J1) refers to the acquisition at the lower level, close to the clavicle bones, while red and yellow lines refer to the acquisition at the middle (J2) and upper (J3) level, respectively. All the contribution below 0.3 Hz is removed.

Data presented in this Sections prove that the plethysmography device is able to detect differences in the jugular behavior at different neck levels.

Comparison among different experimental sessions

Figure 5.12 shows plethysmography traces of subject 3 with short and long strain gauge sensor, in different experimental sessions.

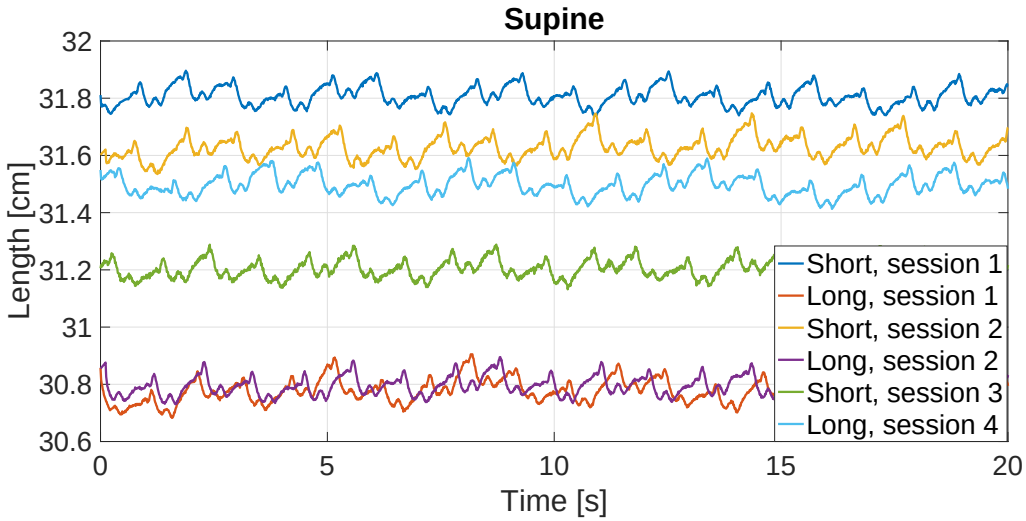

Figure 5.12: Plethysmography traces of subject 3 supine during different experimental sessions. Blue and red lines refer to short and long sensor for the first acquisition, yellow and purple lines refer to short and long sensor for the second acquisition, green line refers to third acquisition with short sensor, and light blue line refers to forth acquisition with long sensor.

Figure 5.13 shows the corresponding Fourier spectra.

From Figure 5.12 we can notice that the same subject seems to have different average values of the neck perimeter at every new acquisition. We can justify this behavior supposing that the strain gauge sensor was not exactly placed at the same level during repetitions of

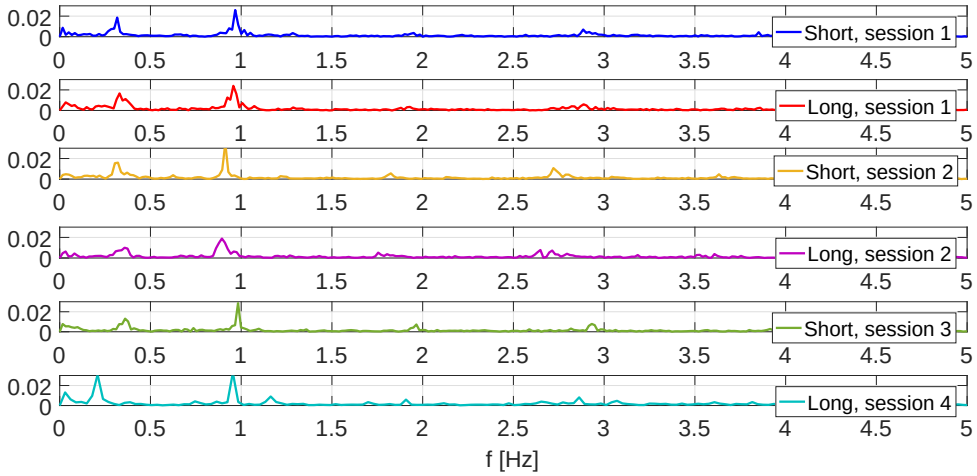

Figure 5.13: Fourier spectra of the plethysmography traces of Figure 5.12 (subject 3 supine during different experimental sessions). Blue and red lines refer to short and long sensor for the first acquisition, yellow and purple lines refer to short and long sensor for the second acquisition, green line refers to third acquisition with short sensor, and light blue line refers to forth acquisition with long sensor.

the protocol. Moreover, we can suppose that muscle condition and hydration of the subject changes in time, and so affecting the neck perimeter. Proof of the variation of physiological status of the subject among the days are given by the slight changes observed in caridac and respiratory peaks of the Fourier spectra These results suggest that, even if the quality of the acquired data does not change and the system is stable and not affected by any external change, it is a good practice to perform acquisitions without stop and restart the protocol, to avoid changes in the physiological status of the subject. One of the main reason is the difficulty to exactly encircle the same anatomical section with a given strain gauge sensor, once it is removed.

Comparison among different postures

Figure 5.14 show plethysmography data acquired from subject 3 (short strain gauge sensor was used) in 5 different postures: supine, sitting, upright, forward bend, and during simulation of walking:

- blue plot refers to subject supine. Its average value is 31.2 cm and it presents marked pulsations both in terms of JVP and of breathing;
- red and yellow plots refer to subject sitting and upright. The average value is around 31.5 cm for both the traces, with a strong decrease in pulsations with respect to the supine trace;
- purple and green plots refer to subject forward bend and walking. The average value is around 31.7 cm and pulsations are not damped.

Differences on neck perimeter is probably due to the change in muscle configuration the subject has in the examined postures. Trace acquired with the subject head down (purple) presents a positive linear trend. That could be an effect of the increase in the blood volume

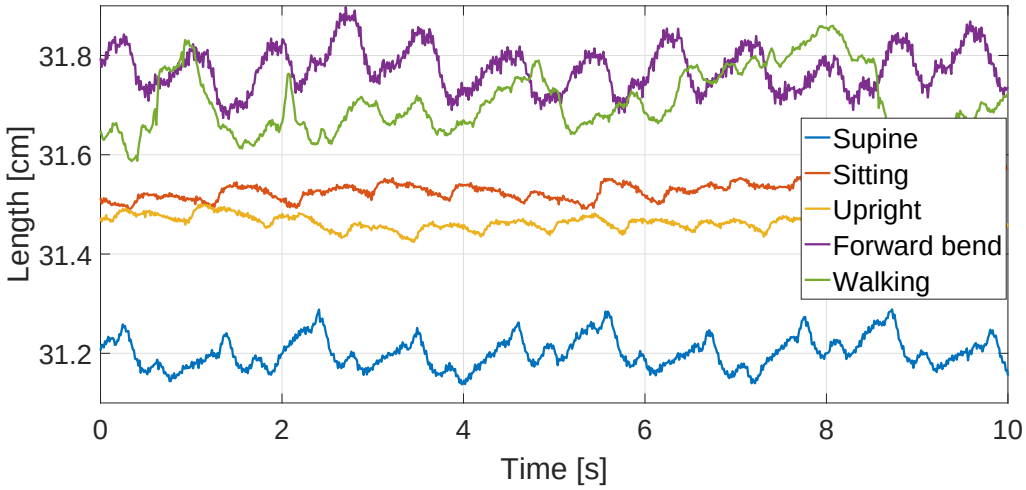

Figure 5.14: Plethysmography traces of subject 3 in different positions. Blue line refers to subject supine, red line refers to subject sitting, yellow line refers to subject upright, purple line refers to subject forward bend, green line refers to the simulation of walking. Ten seconds of acquisition are reported to highlight differences on waveforms due to the posture variation.

in IJVs (subject is tilted down and this carries blood back to the cervical district. Figure 5.15 shows plethysmography traces reported in Figure 5.14 filtered by using DWT.

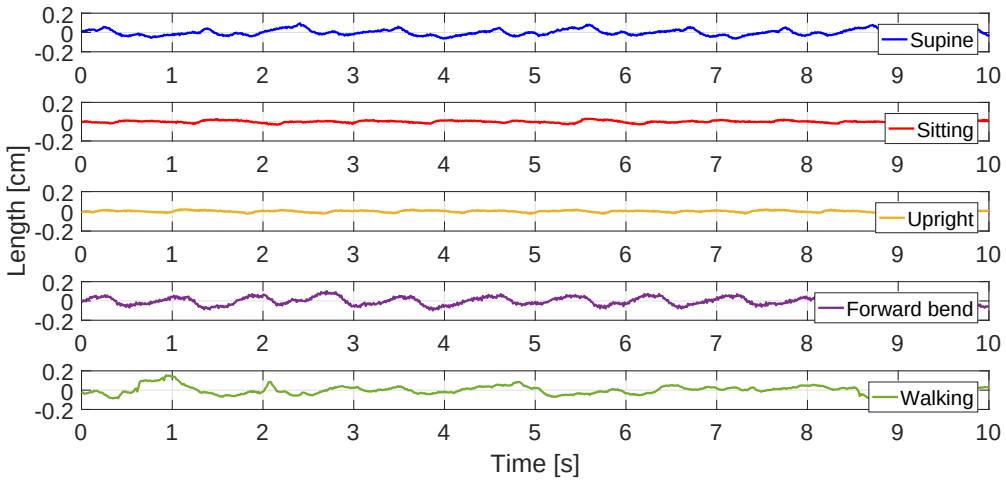

Figure 5.15: Plethysmography traces of subject 3 in different positions. Blue line refers to subject supine, red line refers to subject sitting, yellow line refers to subject upright, purple line refers to subject forward bend, green line refers to the simulation of walking. Ten seconds of acquisition are reported to highlight differences on waveforms due to the posture variation. Data are filtered by using DWT.

Figure 5.16 shows the Fourier spectra of the filtered data presented in Figure 5.15. Looking at the filtered data, we can notice that:

- when the subject is supine (blue plot) the plethysmography trace presents a main peak at around 1 Hz and a second peak at around 0.4 Hz. These peaks are due to the cardiac and respiratory effect, respectively. Some other peaks are visible at around 2 – 3 Hz, probably due to some secondary effects of the cardiac beating to the vessel walls;
- when the subject is sitting or upright (red and orange plots) a broad peak at around

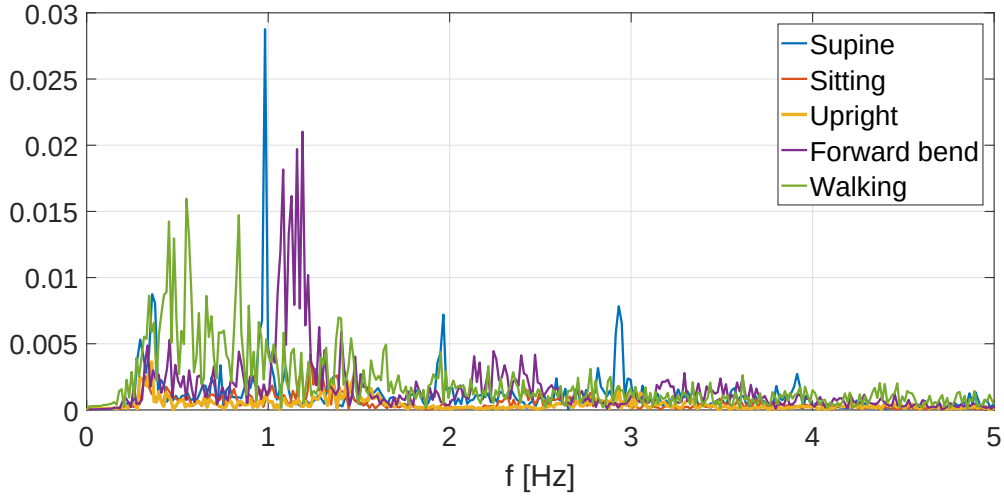

Figure 5.16: Fourier transform of the plethysmography traces of subject 3 in different positions, filtered by using DWT. Blue line refers to subject supine, red line refers to subject sitting, yellow line refers to subject upright, purple line refers to subject forward bend, green line refers to the simulation of walking.

1.4 Hz is detectable;

- when the subject is head down (purple plot) the cardiac peak is broad;
- when the subject is walking, the cardiac peak is negligible.

From these results it is evident that the plethysmography is able to detect the cardiac contribution, mainly when the subject lies in supine position. Indeed, in these situation a marked peak corresponding to the cardiac frequency is detectable in the Fourier spectra of the filtered data.

5.2.2 Experimental results of Drain Brain protocol

Preliminary results of the investigation are presented below. We report in Figure 5.17 an example of the raw data of the three plethysmography sensors, recorded during an experimental session on the ISS.

The solid trace refers to the neck sensor, while the dashed and dot-dashed traces refer to leg and arm sensor, respectively. Raw data are reported in count vs. time. Any change from the baseline value on the vertical axis refers to the output of the sensors after a stimulus (i.e. an elongation). However, the response curve is different for each sensor. Therefore, in order to compare the traces, we converted these data in unit of length by using the (linear) calibration curves. Plethysmography data related to variations of neck perimeter and recorded during different experimental sessions are here reported. Data are presented and compared according to a specific parameter.

Therefore, we will show traces recorded during normal breathing and during a forced respiration at 70 % of the vital capacity; traces recorded with the subject supine and upright; and comparison of traces recorded before, during, and after the permanence of the subject aboard the ISS. In each Figure, 10 seconds of raw data, converted in unit of length, are reported in the top plots. The same time interval is reported in the bottom plots, where filters are applied in order to remove low frequencies from the whole signal and to highlight the cardiac

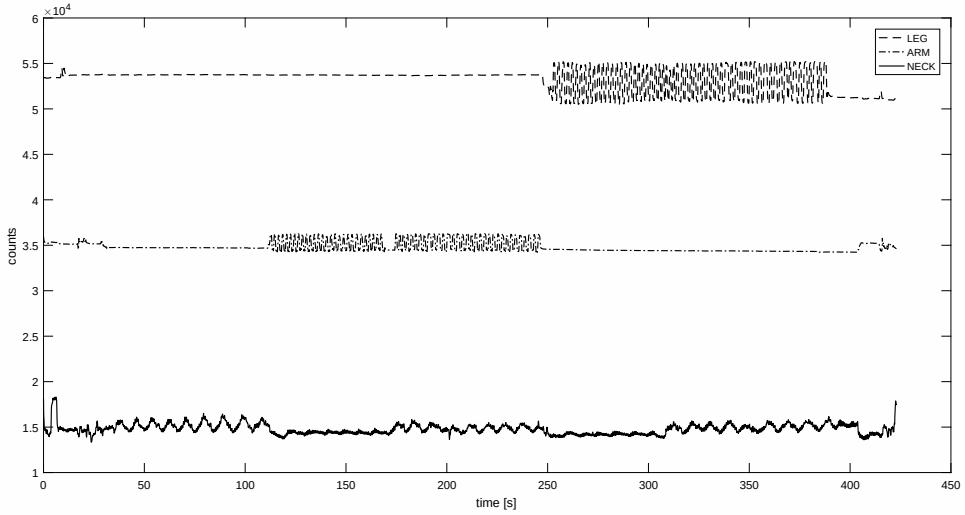

Figure 5.17: Raw data of the plethysmography sensors recorded during an experimental session on the ISS. Top, middle, and bottom curves refer to leg, arm, and neck signals, respectively.

contribution. All the reported data refer to acquisition during left arm exercise, i.e. we show only data from the time interval where the arm sensor is oscillating around its baseline (for instance, in the range 100 - 250 s of Figure 5.17). Such choice is representative of all the neck signals we are interested in.

Breathing variations

In the plots of this section we can see comparison of plethysmography traces of the neck perimeter in the two different conditions of normal and forced breathing. We refer to forced breathing when, during a complete inhalation, the subject reaches a pulmonary filling that is 70% of the measured vital capacity. Figure 5.18 compares such plethysmography traces during upright (left column) and supine (right column) posture.

Top plots of Figure 5.18 show that forcing the respiration produces a general increase in the neck perimeter. When upright, the perimeter increases of 1.3 mm (+18%) and when supine it increases of 2.2 mm (+22%).
Bottom plots of Figure 5.18 show that the average amplitude of the oscillations due to the cardiac contribution arises from 0.10 mm to 0.14 mm in the upright condition. When supine, the oscillations decrease from 0.91 mm to 0.81 mm. Both the increase during upright posture and the decrease during supine posture are not statistically significant ($p = 0.15$ and $p = 0.02$, respectively).

Posture variations

In the plots of this section we can see comparison of plethysmography traces of the neck perimeter in the two different conditions of upright and supine posture. In both the situations the subject is relaxed, with arms close to the body and not moving. Figure 5.19 shows such comparison during normal (left column) and forced breathing (right column).

From the top plots of Figure 5.19 we see that a posture change from upright to supine produces a general increase in the neck perimeter. When breathing normally, the perimeter

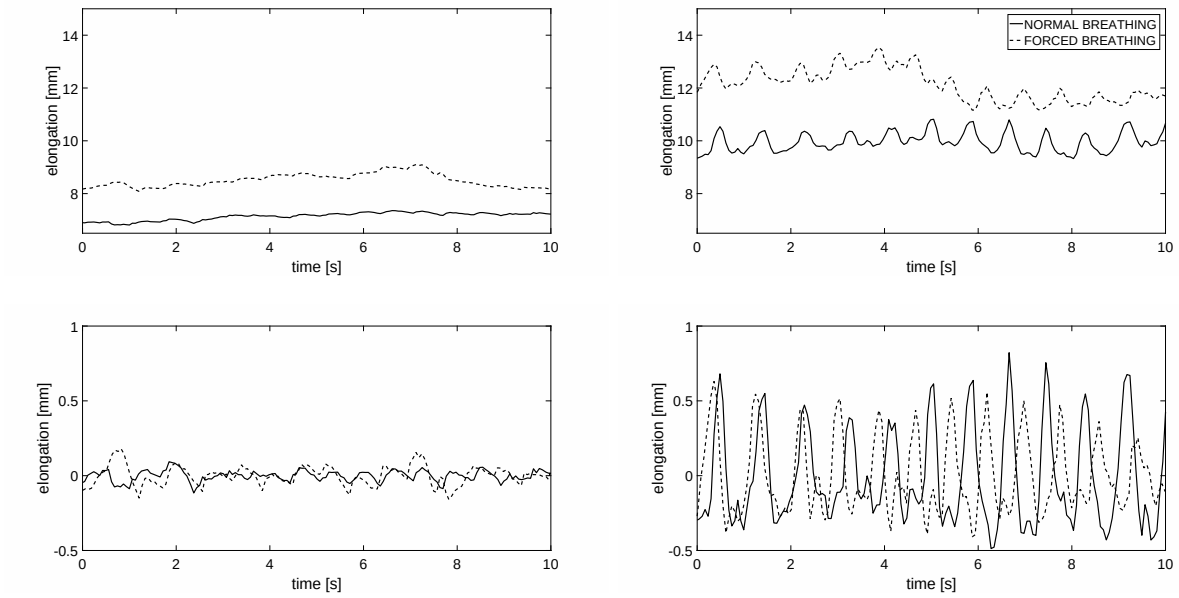

Figure 5.18: Top: Particular of the plethysmography curves recorded with subject upright (left) and supine (right), during left hand exercise (preflight session). Bottom: Particular of the filtered traces to highlight the cardiac contribution to the signal.

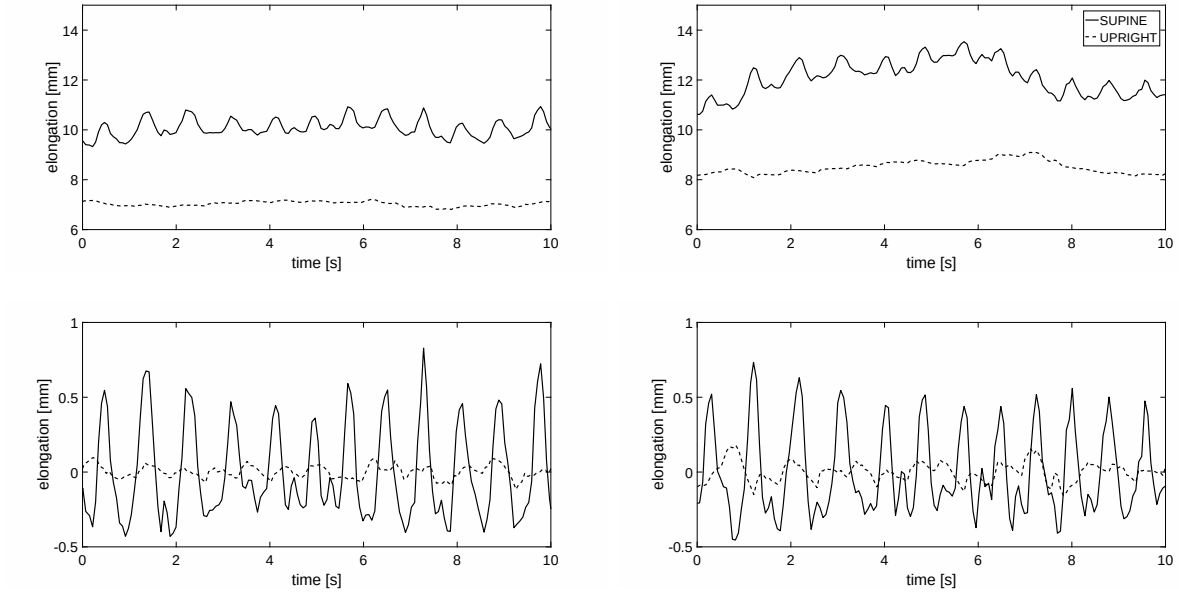

Figure 5.19: Top: Particular of the plethysmography curves recorded with subject breathing normally (left) and deeply (right), during left hand exercise (preflight session). Bottom: Particular of the filtered traces to highlight the cardiac contribution to the signal.

increases of 2.9 mm (+40%), when breathing at 70% of the measured vital capacity it increases of 3.8 mm (+45%).
From the bottom plots of Figure 5.19 we see that the average amplitude of the oscillations due to the cardiac contribution arises from 0.10 mm to 0.91 mm when breathing normally. During forced breathing, the oscillations increase from 0.14 mm to 0.81 mm. Both the increases described are statistically significant ($p < 0.01$).

Gravity field variations

In the plots of this section we can see comparison of plethysmography traces of the neck perimeter in two different conditions of gravitational gradient, i.e. gravity vs. microgravity. Concerning the acquisitions on Earth, we have selected the traces with the subject in supine, in order to reduce the effects of gravity (hydrostatic pressure). In both the situations the subject is breathing normally while performing the left-hand exercise. Figure 5.20 compares plethysmography traces of the neck perimeter in the two different conditions of gravity and microgravity.

From the bottom plot of Figure 5.20 we see that microgravity causes a reduction of the average amplitude of the cardiac oscillations. Moving from Earth to ISS, such oscillations reduce from 0.91 mm to 0.39 mm. This reduction is statistically significant ($p < 0.01$). Figure 5.21 compares plethysmography traces of the neck perimeter during the mission aboard the ISS.

From the bottom part of Figure 5.21 we see that the average amplitude of the oscillations due to the cardiac contribution changes from 0.39 mm to 0.60 mm and and then to 0.66 mm when breathing normally. Therefore, there is a considerable rise in the amplitude of the oscillations measured between the first acquisition (inflight 1) and the others (+54% and +69% respectively), with only a slight increase between the second and the third one.
Figure 5.22 compares plethysmography traces of the neck perimeter before and after the mission aboard the ISS.

From the bottom plot of Figure 5.22 we see that the average amplitude of the oscillations due to the cardiac contribution are similar (0.91 mm and 0.84 mm). The decrease in the amplitude of the measured oscillations (-8%) is not statistically significant ($p = 0.08$).

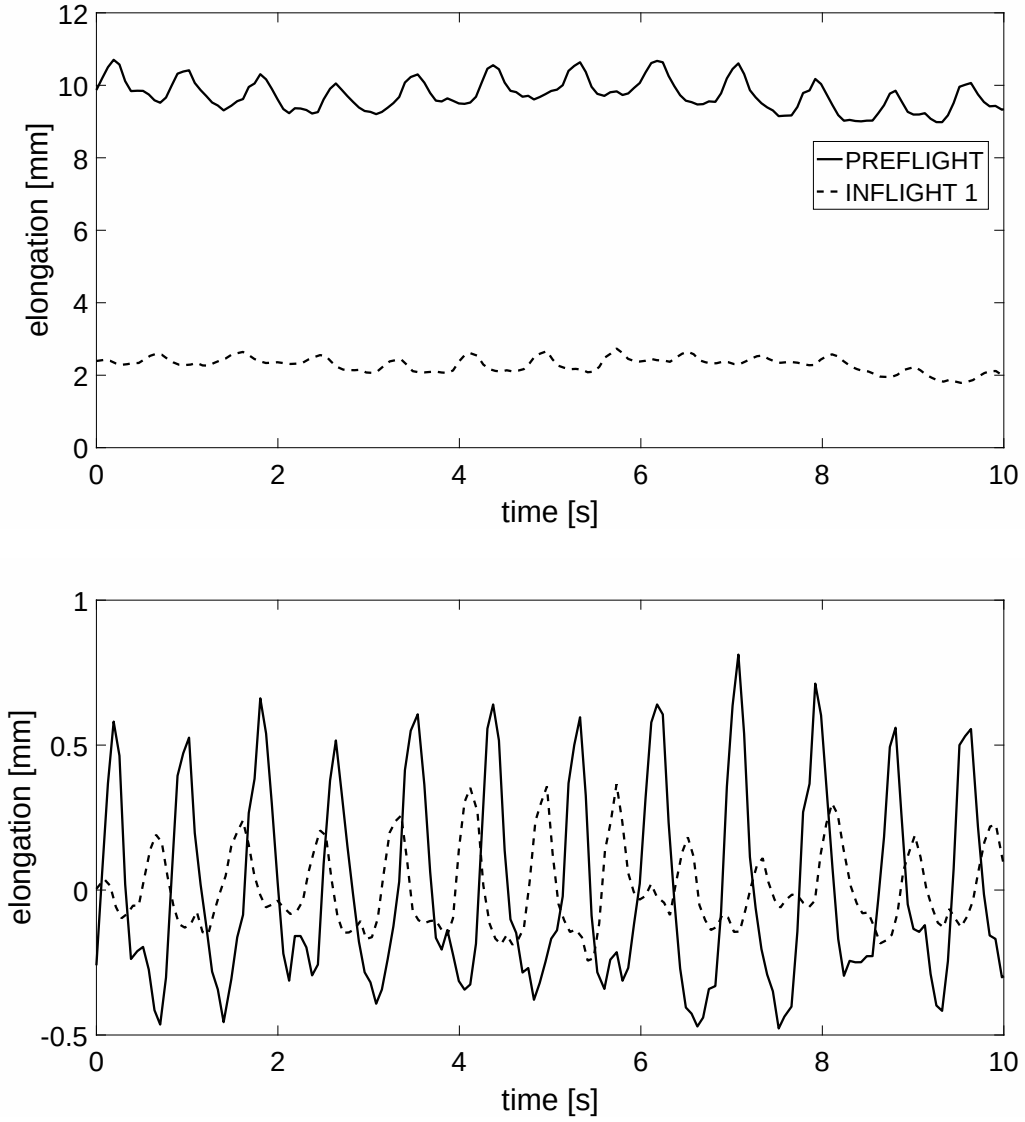

Figure 5.20: Top: Particular of the plethysmography curves acquired with subject breathing normally (left hand exercise). Bottom: Particular of the filtered traces to highlight the cardiac contribution to the signal.

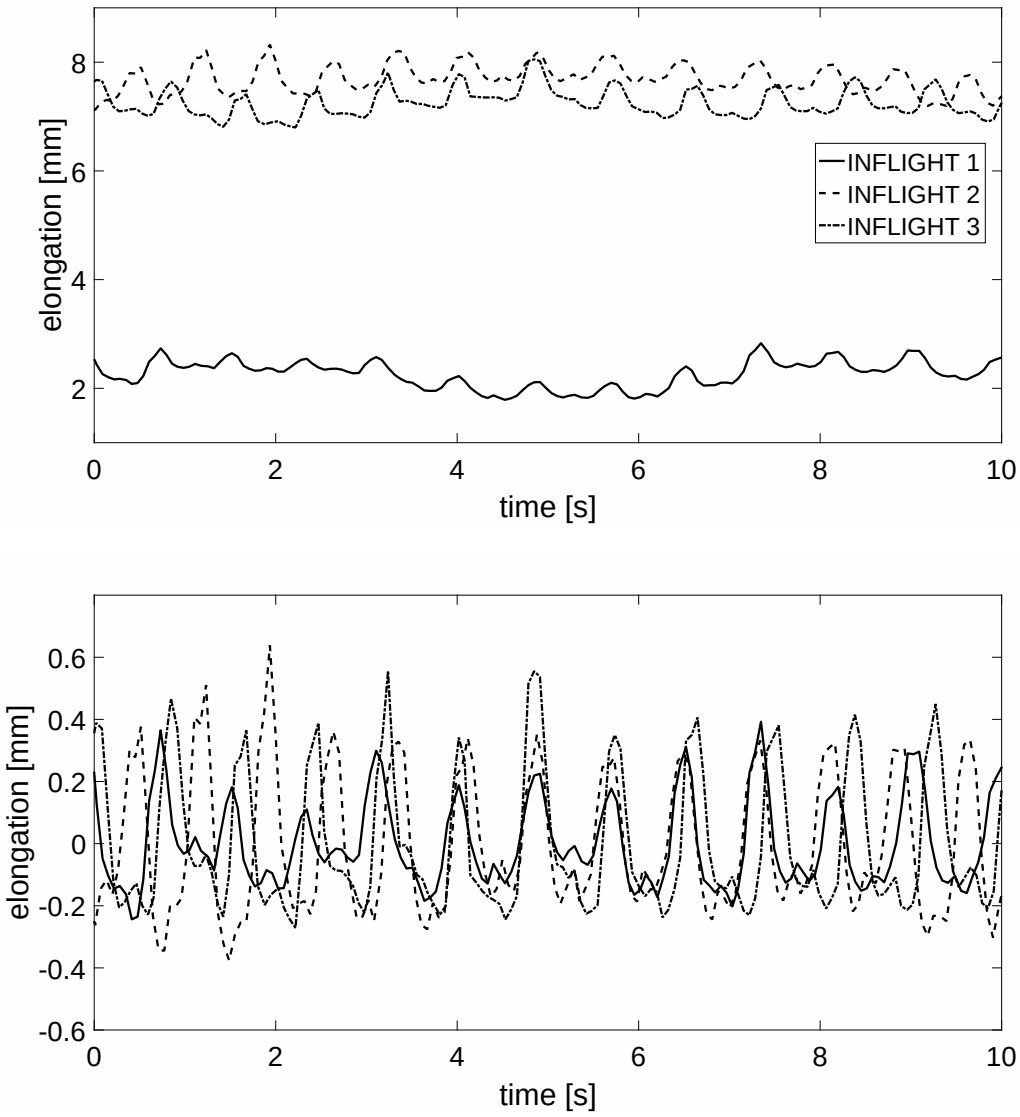

Figure 5.21: Top: Particular of the plethysmography curves acquired with subject breathing normally (left hand exercise). Bottom: Particular of the filtered traces to highlight the cardiac contribution to the signal.

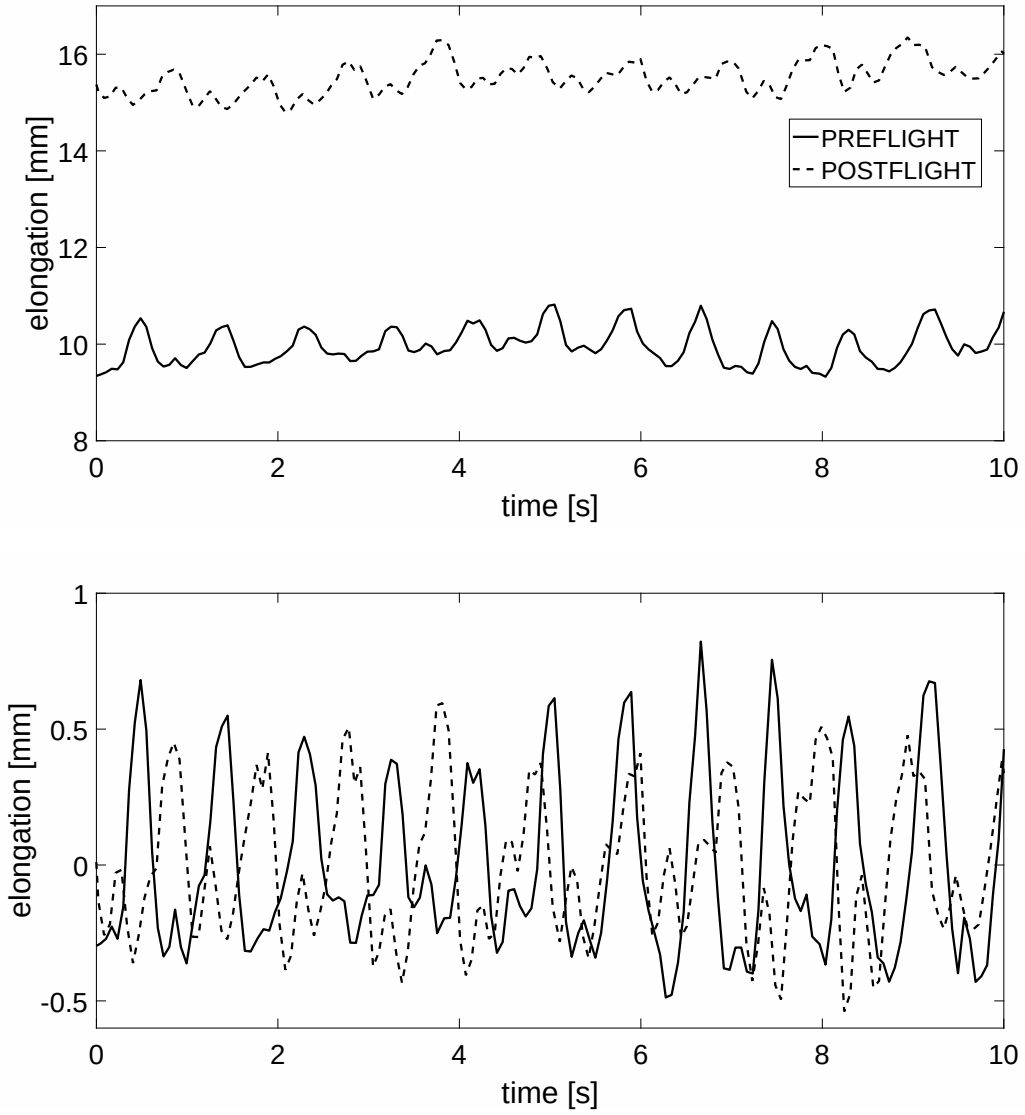

Figure 5.22: Top: Particular of the plethysmography curves recorded with subject breathing normally (left hand exercise). Bottom: Particular of the filtered traces to highlight the cardiac contribution to the signal.

Chapter 6

Conclusions

Due to the complexity of the relationships involved, and the large variability in the anatomical parameters, it is extremely difficult to understand in simple qualitative terms the effect of alterations in the extracranial arterial and venous circulation on the brain functionality. Therefore, the study of the cerebral inflow and outflow, and the relations between the loss of healthy physiologic equilibrium and the onset of diseased conditions, can largely benefit from the use of computational models.

The aim to link a 1 dimensional (1D) model of the arterial vascular tree with a 0 dimensional (0D) model of the drainage of blood flow from the brain and skull through another 0D model of the intracranial circulation is to simulate the cranial and extracranial inflow and outflow vessel pathway behavior and the mechanisms involved in the feeding and drainage process together with the intracranial circulation and the action of cerebrovascular regulation mechanisms. The model represents a new tool for improving our understanding of the whole system.

It is difficult to have a complete and detailed overview of the blood flows circulating to and from the braincase. Several researchers have studied the cerebral hemodynamics and its relationship with extracranial anatomic and posture changes [41, 69]. First, average absolute values of blood flow could be considerably different among subjects because of physiologic variability. Second, due to the complex network of vessels and their variable interconnections, it is difficult to have a map of the circulation able to describe any specific case in detail. Third, there is insufficient knowledge of the relationships between flow alterations and the degree of occurrence of events such as postural changes or stenosis. Finally, even in a situation that does not have variability factors, the assessment of blood flow values can be difficult for several reasons.

A comprehensive model was developed to investigate correlations between cerebral hemodynamics and alterations in the extracranial venous circulation due to posture changes and/or extracranial venous obstructions (stenosis). The model summarizes the different segments of the vascular system and reproduces experimental flows with a finite and easily tunable number of parameters. This model is an attempt to summarize a complex system in a simple picture, taking into account all the available data for obtaining information not directly achievable with experimental noninvasive measurements, such as venous sinuses pressure P_{vs} or intracranial pressure, very important for checking the status of the intracranial environ-

ment and, hopefully, for preventing neurologic diseases. The purpose of this work was to validate the simulation results by using magnetic resonance imaging (MRI) and echo-color Doppler (ECD) experimental blood flow data in humans. The model presented here is tuned by using large datasets of subjects, to be more confident about the average hemodynamic condition of a given type of stenotic pattern. We benefited from the use of MRI techniques to have a detailed map of the vessels and of the blood circulating in them. The drawback of MRI for this work is that only supine data are available, whereas ECD allows both supine and upright assessment. However, ECD does not allow the evaluation of minor vessels, and it has a bias related to the operator dependence that can lead to incorrect evaluations. Such flows are the average of experimental measurements on several subjects (Tables 2.5 and 2.6), so we are confident that the model parameters reproduce a statistically significant circulatory behavior, including different clinical conditions (healthy controls or subjects with stenotic patterns).

The convergence of the model presented in this work has been investigated with all the experimental flows reported in Tables 2.5 and 2.6. We checked that average flows reported in such tables are the mean value of Gaussian-like datasets, so we are confident that the model simulates the average condition of normal distributions of flow.

The two main features of the model are that it accounts for the dependence of the hydraulic properties of the internal jugular veins (IJVs) with respect to the gravity field and that it includes a validated model for the simulation of the intracranial circulation. That makes it an useful tool for the study of the correlations between extracranial blood redistributions and changes in the intracranial environment.

We performed simulations of the effect of posture change from supine to upright on pressures and blood flows, first with basal drainage and then assuming a lack of conductance of some particular vessel tract.

The model allows simulating the change of posture from supine to upright. IJVs are divided into different segments to properly simulate the differences measured along the jugular length. In particular, we chose to divide IJVs into the 3 segments as recently established in an international scientific consensus [123] to make the model easily comparable with the most recent and validated experimental results.

The model reproduces average physiologic behavior of the jugular, vertebral, and cerebral ducts in terms of pressures and flows. Simulations of average jugular and vertebral blood flow variations due to a change of posture from supine to upright also matched the experimental data. Every simulated CBF fell inside the standard error from the corresponding average experimental value, as well as the simulated extracerebral arterial flow.

The model outcomes, after parameter tuning, are in excellent agreement with experimental supine average flow of the non stenotic (NST) group (Figure 3.2). Indeed, all the main arterial and venous flows supplying the brain that we modeled fall inside the standard error from the corresponding experimental value. Moreover, model results satisfactorily match the supine/upright percentage variation in jugular and extrajugular pathways observed in a second group of 10 healthy controls (Figure 3.1). Therefore, we achieved the objective of tuning the model to reproduce an average healthy subject, from the point of view of the circulation. Starting from the NST-tuned model, it is easy to reproduce pathologic conditions like the situations reported in Table 2.3. Such new simulations are obtained by changing some of

the conductances to reproduce the MRI experimental flow data (Table 2.5). Results show that conductances are greatly reduced in the IJV stenotic area and increased in the vertebral pathway. This aspect could be an index of how the whole venous pattern is affected by the presence of a jugular stenosis. Indeed, the increase in the vertebral conductance may represent a chronic compensatory change performed to maintain adequate brain drainage to prevent cranial hypertension. This aspect is highlighted in Figure 3.15, where the temporal behavior of simulated P_{vs} with time is reported for different stenotic conditions. Intracranial autoregulatory mechanisms maintain cerebral blood flow at a physiologic value, both in supine and upright conditions (Figures 3.3, 3.13 and 3.14). P_{vs} achieves a new equilibrium in a few seconds after the posture change. The situation is very different when IJVs are totally occluded, for example, at the lower part.
The model is able to give information about the average flows in different points of the jugular ducts, so taking into account the amount of blood coming from the anastomotic connections. A fundamental model assumption is the existence of anastomotic connections between left and right IJV. These vessels are not measured, but they are necessary to explain the increase in flow along every nonstenotic IJV (Tables 2.5 and 2.6).
The model may represent an useful tool for the study of the correlation among posture variations, vessel conductances (normal or abnormal), and the consequent pressure and flow changes. Moreover, we can easily use it to verify how the blood redistribution due to change of posture affects the pressures in specific points of the system. This model takes into account intracerebral mechanisms such as CSF circulation and the onset of IJV obstacles. Furthermore, a peculiar aspect of the model is the description of intracranial blood flow autoregulatory mechanisms that play a pivotal role in maintaining an adequate cerebral perfusion in the different simulated conditions. The study of venous blood flow changes in patients with partial or total impairment in cerebral autoregulation may be the subject of future model applications. We modeled intra- and extracranial circulation, so that the whole system can predict whether and how the occurrence of extracerebral stenotic patterns affect the pressure equilibrium in the braincase during most of the human lifetime (sitting or standing), potentially leading to long-term diseases due to pressure imbalance.
A limitation of the model is related to the assessment of venous compliances (Table 2.7). We need experimental measurements to properly assess vessel compliances and give more effectiveness to the time dependence results of pressures (Figure 3.15).
From the point of view of the study of venous insufficiency, the present simulations suggest two important considerations:

- the cerebral venous return system is quite robust. A single occlusion, or even multiple occlusions of moderate entity, can induce only mild changes in venous sinuses pressure and in total blood flow Indeed, this is the fundamental role of the strong anastomotical connections incorporated in the model;

- pathological states, characterized by multiple severe obstructions, can lead to significant pressure changes in the venous sinuses, hence, in possible alteration in cerebrospinal fluid circulation and brain tissue pressure. Which adjustments may be produced in these cases (either the opening of new collaterals, a reset of the autoregulation set point, or a permanent pressure increase) remains to be investigated.

The plethysmography device we developed is able to detect variations of some anatomical cross section of the human being. In this work we focused on changes of neck perimeter, that is related to the jugular veins pulsation (JVP). The device detects physiological variations of this pulsation due to the different postures of the subject, other than the expected differences among subjects. Moreover, we see that the signal is dependent on the position of the strain gauge sensor along the neck length. That could be intersting to study the details of the cerebral drainage system, instead of considering IJVs as tubes with fixed properties.
A copy of this plethysmography device, adapted to operate aboard the International Space Station (ISS), was used in the so called Drain Brain project. Following a dedicated protocol, we checked variations of neck perimeter, and so on the functionality of cerebral venous drainage, through the detection of IJV pulsation and its changes in different postural and gravity conditions.
The increase in neck perimeter due to forced breathing on Earth is around 20% independently from the posture (see Figure 5.18). The same maneuver seems not to affect the cardiac status (i.e. the amplitude of the oscillations at around 1 Hz), since there is no significant difference of this parameter when the respiratory condition is varied both in supine and in upright posture. Concerning the change of posture under usual gravitational conditions, the increase in neck perimeter is more than 40%, indipendently from the respiratory status (see Figure 5.19). Even the cardiac status is affected by the posture, being the amplitude of the oscillations at around 1 Hz much higher when the subject changes from upright to supine [41]. The respiration seems not to provide a strong contribution to the behavior of this parameter. Anyway, we can notice from Figure 5.18 that the amplitude of the cardiac oscillations during forced breathing is sligthly higher in upright condition but slightly lower when in supine condition. We may conclude that the exercise to force the respiration leads to a reduction of the compliance of collapsible vessels which in turn reduces the amplitude of the collected signal.
The first finding which arises from the comparison between preflight and inflight data is the significant reduction of the signal amplitude due to cardiac oscillations (see Figure 5.20) that may suggests a reduction of the cardiac status. Such situation could be directly associated with blood redistribution and hypovolemia, as observed in previous space flight studies [43].
The second finding is the significant difference between cardiac oscillations recorded over the ISS experimental sessions acquired during the first ISS session in order of time, and the two subsequent sessions (see Figure 5.21). Figure 5.21 shows that oscillations measured during second and third sessions are considerably higher than the first one. This may suggest that some kind of regulatory mechanism is acting in order to adapt to microgravity condition. Indeed, it has been reported that substantial dilation of IJVs is typical in microgravity and starts from the initial days of space flight [43]. From our findings it seems that the venous system is trying to recover the preflight equilibrium, or to find a new state to adapt to the new gravitational load. The final observation is related to the cardiac oscillations measured before and after the space flight (see Figure 5.22). We may hypotesize that, if something happened at the heart or circulatory level when the subject was aboard the ISS so that the cardiac status was lowered, the same or different regulation mechanisms acted in order to restore the preflight condition. Such oscillations are not statistically different, with the postflight quite lower in absolute value. This means that regulatory mechanisms acted in order to restore the preflight conditions. Comparison of plethysmography data confirmed that long

duration spaceflights lead to a redistribution of venous blood flow and showed interesting differences in the amplitude of cardiac oscillations measured at the level of the neck veins. Future work will include a comparison between plethysmography data and US data so as to complete the investigation on the drainage function of the IJV in microgravity. Preliminary clinical results suggest that cervical plethysmography has great potential both as inexpensive screening device and a postoperative monitoring tool [124].

This work demonstrates the feasibility to use the plethysmography device as a diagnostic tool. First of all, data acquisition is non invasive. Then, the device is useful to be used in more complex protocols, allowing the subject to move during the exam, to check the effect on drainage due to any kind of movement. It is desirable that the next step for the development of the device will be the upgrade of the connection between strain gauge sensors and electronic apparatus through a wireless connection instead of wires. In this way movements of the analyzed subject will be more comfortable.

Plethysmography is a powerful method since it does not affect the subject parameter such as cross sectional area of the IJVs, that is recognized as the main problem when some acquisition protocol (e.g. flow acquisition) is performed by using ultrasound technique. Moreover, the apparatus is easily configurable to collect data to more than one anatomical district at the same time.

We showed that the apparatus is suitable for further studies concerning the cerebral venous system, but it is possible to think about a different use like, for example, the study of the effect of movements on circulation through the application of other strain gauge sensors on arms and legs, other than at the neck level. Beside the cardiac pulsation, the device collect also effects on vasculature due to breathing, other than changes of the muscular tone of the zone encircled by the sensors. This means, for example, that protocols can be performed to study the effect of breathing on blood circulation. By using the discrete wavelet transform together with the Fourier transform, is recognized as a very useful method to properly filter and analyze plethysmography signals. Contribution to the whole signal from different recognized sources, such as heart or respiration, can be easily extracted and analyzed.

Bibliography

[1] Aaslid R, Lindegaard KF, Sorteberg W, Nornes H (1989), "Cerebral autoregulation dynamics in humans," *Stroke*, Vol. 20(1), pp. 45–52.

[2] Alastruey J, Parker KH, Peir J, Byrd SM, Sherwin SJ (2007), "Modelling the circle of Willis to assess the effects of anatomical variations and occlusions on cerebral flows," *J Biomech*, Vol. 40(8), pp. 1794–1805.

[3] Alastruey J, Parker KH, Peir J, Sherwin SJ (2008), "Lumped Parameter outflow models for 1-D blood flow simulations: effect on pulse waves and parameter estimation," *Commun Comput Phys*.

[4] Alastruey J, Parker KH, Peir J, Sherwin SJ (2009), "Analysing the pattern of pulse waves in arterial networks: a time-domain study," *J Eng Math*, Vol. 64(4), pp. 331–351.

[5] Alastruey J, Khir AW, Peir J (2011), "Pulse wave propagation in a model human arterial network: Assessment of 1-D visco-elastic simulations against in vitro measurements," *J Biomech*, Vol. 44(12), pp. 2250–2258.

[6] Alastruey J, Parker KH, Sherwin SJ (2012), "Arterial pulse wave haemodynamics," *11th International Conference on Pressure Surges*, pp. 401–442.

[7] Alperin N, Lee SH, Sivaramakrishnan A, Hushek SG (2005), "Quantifying the effect of posture on intracranial physiology in humans by MRI flow studies," *J Magn Reson Imaging*, Vol. 22, pp. 591–596.

[8] Anderson CM, Edelman RR, Turski PA (1993), "Clinical magnetic resonance angiography," *New York:Raven Press*.

[9] Applefeld MM (1990), "The Jugular Venous Pressure and Pulse Contour. In: Walker HK, Hall WD, Hurst JW, editors. Source Clinical Methods: The History, Physical, and Laboratory Examinations, Chapter 19. 3rd edition," *Boston: Butterworths*.

[10] Arbeille P, Provost R, Zuji K, Vincent N (2015), "Measurements of jugular, portal, femoral, and calf vein cross-sectional area for the assessment of venous blood redistribution with long duration spaceflight," *Eur J Appl Physiol*, Vol. 115(10), pp. 2099–2106.

[11] Armentano RL, Barra JG, Levenson J, Simon A, Pichel RH (1995), "Arterial wall mechanics in conscious dogs. Assessment of viscous, inertial, and elastic moduli to characterize aortic wall behavior," *Circ Res*, Vol. 76(3), pp. 468–478.

[12] Armentano R, Megnien JL, Simon A, Bellenfant F, Barra J, Levenson J (1995), "Effects of hypertension on viscoelasticity of carotid and femoral arteries in humans," *Hypertension*, Vol. 26, pp. 48–54.

[13] Avolio AP (1980), "Multi-branched model of the human arterial system," *Med Biol Eng Comput*, Vol. 18(6), pp. 709–718.

[14] Bassez S, Flaud P, Chauveau M (2005), "Modeling of the deformation of flexible tubes using a single law: application to veins of the lower limb in man," *J Biomech Eng*, Vol. 123(1), pp. 58–65.

[15] Beggs CB (2013), "Venous hemodynamics in neurological disorders: an analytical review with hydrodynamic analysis," *BMC Med*, Vol. 11, pp. 142.

[16] Braakman R, Sipkema P, Westerhof N (1989), "A dynamic nonlinear lumped parameter model for skeletal muscle circulation," *Ann Biomed Eng*, Vol. 17(6), pp. 593–616.

[17] Canic S, Kim EH (2003), "Mathematical analysis of the quasilinear effects in a hyperbolic model blood flow through compliant axi-symmetric vessels," *Math Meth Appl Sci*, Vol. 26, pp. 1161–1186.

[18] Canic S, Tambaca J, Guidoboni G, Mikelic A, Hartley CJ, Rosenstrauch D (2006), "Modeling viscoelastic behavior of arterial walls and their interaction with pulsatile blood flow," *SIAM J Appl Math*, Vol. 67(1), pp. 164–193.

[19] Chambers B, Chambers J, Churilov L, Cameron H, Macdonell R (2014), "Internal jugular and vertebral vein volume flow in patients with clinically isolated syndrome or mild multiple sclerosis and healthy controls: results from a prospective sonographer-blinded study," *Phlebology*, Vol. 29(8), pp. 528–535.

[20] Chua Chiaco JM, Parikh NI, Fergusson DJ (2013), "The jugular venous pressure revisited," *Cleve Clin J Med*, Vol. 80(10), pp. 638–644.

[21] Cirovic S, Walsh C, Fraser WD, Gulino A (2003), "The effect of posture and positive pressure breathing on the hemodynamics of the internal jugular vein," *Aviat Space Environ Med*, Vol. 74(2), pp. 125–131.

[22] Cohen A, Ryan RD (1995), "Wavelets and multiscale signal processing," *Dordrecht: Springer*.

[23] Compston A, Coles A (2008), "Multiple sclerosis," *Lancet*, Vol. 372(9648), pp. 1502–1517.

[24] Craiem D, Graf S, Pessana F, Grignola JC, Bia D, Gins F, Armentano R (2005), "Cardiovascular engineering: modelization of ventricular-arterial interaction in systemic and pulmonary circulation," *Lat Am appl res*, Vol. 35(2), pp. 111–114.

[25] Danfoss Stretch sensor data sheet 094F3070 REV02.

[26] Doepp F, Paul F, Valdueza JM, Schmierer K, Schreiber SJ (2010), "No cerebrocervical venous congestion in patients with multiple sclerosis," *Ann Neurol*, Vol. 68(2), pp. 173–183.

[27] Drazner MH, Rame JE, Stevenson LW, Dries DL (2001), "Prognostic importance of elevated jugular venous pressure and a third heart sound in patients with heart failure," *N Engl J Med*, Vol. 345(8), pp. 574–581.

[28] Drochon A (2015), "Sinusodal flow of blood in a cylindrical deformable vessel exposed to an external magnetic field," *Eur Phys J Appl Phys*, Vol. 73.

[29] Epstein HM, Linde HW, Crampton AR, Ciric IS, Eckenhoff JE (1970), "The vertebral venous plexus as a major cerebral venous outflow tract," *Anesthesiology*, Vol. 32(4), pp. 332–337.

[30] Feng W, Utriainen D, Trifan G, Elias S, Sethi S, Hewett J, Haacke EM (2012), "Characteristics of flow through the internal jugular veins at cervical C2/C3 and C5/C6 levels for multiple sclerosis patients using MR phase contrast imaging," *Neurol Res*, Vol. 34(8), pp. 802–809.

[31] Feng W, Utriainen D, Trifan G, Haacke EM (2012), "Quantitative Flow Measurements in the Internal Jugular Veins of Multiple Sclerosis Patients Using Magnetic Resonance Imaging," *Rev Recent Clin Trials*, Vol. 7(2), pp. 117–126.

[32] Ferreira AJM (2009), "MATLAB Codes for Finite Element Analysis," *:Springer*.

[33] Folkow B, Neil E (1973), "Circulation," *New York: Oxford University Press*.

[34] Formaggia L, Lamponi D, Quarteroni A (2003), "One dimensional models for blood flow in arteries," *J Eng Math*, Vol. 47, pp. 251–276.

[35] Fontecave-Jallon J, Baconnier P (2007), "Berkeley-Madonna implementation of Ikedas model," *Conf Proc IEEE Eng Med Biol Soc*, pp. 582–585.

[36] Fung YC (1997), "Biomechanics Circulation," *New York: Springer Science & Business Media*.

[37] Gadda G, Taibi A, Sisini F, Gambaccini M, Zamboni P, Ursino M (2015), "A new hemodynamic model for the study of cerebral venous outflow," *Am J Physiol Heart Circ Physiol*, Vol. 308(3), pp. H217–H231.

[38] Gadda G, Taibi A, Sisini F, Gambaccini M, Sethi SK, Utriainen DT, Haacke EM, Zamboni P, Ursino M (2016), "Validation of a hemodynamic model for the study of the cerebral venous outflow system using MR imaging and echo-color Doppler data," *AJNR Am J Neuroradiol*, [Epub ahead of print].

[39] Giannessi M, Ursino M, Murray WB (2008), "The design of a digital cerebrovascular simulation model for teaching and research," *Anesth Analg*, Vol. 107(6), pp. 1997–2008.

[40] Gilat A (2004), "An Introduction with Applications 2nd Edition," *:John Wiley & Sons*.

[41] Gisolf J, van Lieshout JJ, van Heusden K, Pott F, Stok WJ, Karemaker JM (2004), "Human cerebral venous outflow pathway depends on posture and central venous pressure," *J Physiol*, Vol. 560(Pt 1), pp. 317–327.

[42] Grabe M, Oster G (2001), "Regulation of organelle acidity," *J Gen Physiol*, Vol. 117, pp. 329–344.

[43] Grigoriev AI, Kotovskaya AR, Fomina GA (2011), "The human cardiovascular system during space flight," *Acta Astronaut*, Vol. 68, pp. 1495–1500.

[44] Guyton AC (1963), "Circulatory physiology Cardiac output and its regulation," *:W. B. Saunders Company.*

[45] Haacke EM, Feng W, Utriainen D, Trifan G, Wu Z, Latif Z, Katkuri Y, Hewett J, Hubbard D (2012), "Patients with multiple sclerosis with structural venous abnormalities on MR imaging exhibit an abnormal flow distribution of the internal jugular veins," *J Vasc Interv Radiol*, Vol. 23(1) pp. 60–68.

[46] Haacke EM, Sethi SK, Jiang J, Wang Y, Utriainen DT (2015), "The role of magnetic resonance imaging in assessing venous vascular abnormalities in the head and neck: a demonstration of cerebrospinal venous insufficiency in a subset of multiple sclerosis patients," *Veins and Lymphatics*, Vol. 4(2).

[47] Hargens AR, Bhattacharya R, Schneider R (2013), "Space physiology VI: exercise, artificial gravity, and countermeasure development for prolonged space flight," *Eur J Appl Physiol*, Vol. 113(9), pp. 2183–2192.

[48] Holzapfel GA, Gasser TC, Ogden RW (2000), "A new constitutive framework for arterial wall mechanics and a comparative study of material models," *Journal of Elasticity and the Physical Science of Solids*, Vol. 61(1), pp. 1–48.

[49] Hughes T, Lubliner J (1973), "On the one–dimensional theory of blood flow in the larger vessels," *Math Biosci*, Vol. 18(1–2), pp. 161–170.

[50] Hughes TJ (1974), "A study of the one-dimensional theory of arterial pulse propagation," *University of California, Berkeley:Thesis (Ph. D. in Engineering Science).*

[51] Jagielska K, Trzupek D, Lepers M, Pelc A, Zieliski P (2007), "Effect of surrounding tissue on propagation of axisymmetric waves in arteries," *Phys Rev E Stat Nonlin Soft Matter Phys*, Vol. 76(6 Pt 2).

[52] Jiang J, Kokeny P, Ying W, Magnano C, Zivadinov R, Mark Haacke E (2015), "Quantifying errors in flow measurement using phase contrast magnetic resonance imaging: comparison of several boundary detection methods," *Magn Reson Imaging*, Vol. 33(2), pp. 185–193.

[53] Karmon Y, Zivadinov R, Weinstock-Guttman B, Marr K, Valnarov V, Dolic K, Kennedy CL, Hojnacki D, Carl EM, Hagemeier J, Hopkins LN, Levy EI, Siddiqui AH (2013), "Comparison of intravascular ultrasound with conventional venography for detection of extracranial venous abnormalities indicative of chronic cerebrospinal venous insufficiency," *J Vasc Interv Radiol*, Vol. 24(10), pp. 1487–1498.e1.

[54] Kokeny P, Jiang J, Haacke EM (2013), "Assessing the effects of vessel segmentation boundary size on flow quantification error and comparing multiple automatic segmentation Aagorithms ," *Proc Intl Soc Mag Reson Med*, Vol. 21, pp. 1338.

[55] Kozlovsky P, Zaretsky U, Jaffa AJ, Elad D (2014), "General tube law for collapsible thin and thick-wall tubes," *J Biomech*, Vol. 47(10), pp. 2378–2384.

[56] Kresch E (1979), "Compliance of flexible tubes," *J Biomech*, Vol. 12(11), pp. 825–839.

[57] Lennox PH, Umedaly HS, Grant RP, White SA, Fitzmaurice BG, Evans KG (2006), "A pulsatile pressure waveform is a sensitive marker for confirming the location of the thoracic epidural space," *J Cardiothorac Vasc Anesth*, Vol. 20(5), pp. 659–663.

[58] Lynch S (2004), "Dynamical Systems with Applications using MATLAB," *Birkhauser*.

[59] Maarten J (2000), "Wavelet thresholding and noise reduction," *Heverlee*.

[60] Maas JJ (2015), "Mean systemic filling pressure: its measurement and meaning," *Neth J Crit Care*, Vol. 19(1), pp. 6–11.

[61] Mackay IF (1947), "An experimental analysis of the jugular pulse in man," *J Physiol*, Vol. 106(2), pp. 113–118.

[62] Mackenzie J (1902), "The study of the pulse, arterial, venous, and hepatic, and of the movements of the heart," *Edinburgh: Young J. Pentland*

[63] Macye RI, Oster GF (2001), "Berkeley Madonna," *Univ. of California, Berkeley, CA.*, http://www.berkeleymadonna.com/jmadonna/jmadrelease.html

[64] Majka M, Gadda G, Taibi A, Gazka M, Zieliski P (2016), "Protective properties of the arterial system against peripherally generated waves," *Math Biosci*, Accepted for publication.

[65] Magosso E, Cavalcanti S, Ursino M (2002), "Theoretical analysis of rest and exercise hemodynamics in patients with total cavopulmonary connection," *Am J Physiol Heart Circ Physiol*, Vol. 282(3), pp. H1018–H1034.

[66] Malagoni AM, Galeotti R, Menegatti E, Manfredini F, Basaglia N, Salvi F, Zamboni P (2010), "Is chronic fatigue the symptom of venous insufficiency associated with multiple sclerosis? A longitudinal pilot study," *Int Angiol*, Vol. 29(2), pp. 176–182.

[67] Mallat S (1998), "A wavelet tour of signal processing," *Academic Press*.

[68] Mancini M, Lanzillo R, Liuzzi R, Di Donato O, Ragucci M, Monti S, Salvatore E, Brescia Morra V, Salvatore M (2014), "Internal jugular vein blood flow in multiple sclerosis patients and matched controls," *Plos One*, Vol. 9(3), pp. e92730.

[69] Marcotti S, Marchetti L, Cecconi P, Votta E, Fiore GB, Barberio A, Viotti S, Redaelli A, Lagan MM (2015), "An anatomy-based lumped parameter model of cerebrospinal venous circulation: can an extracranial anatomical change impact intracranial hemodynamics?," *BMC Neurol*, Vol. 15(95).

[70] Martin N, Traboulsee AL, Machan L, Klass D, Ellchuk T, Zhao Y, Knox KB, Kopriva D, Lala S, Nickel D, Otani R, Perera WR, Rauscher A, Sadovnick AD, Szkup P, Li DK (2016), "Prevalence of Extracranial Venous Narrowing on Magnetic Resonance Venography is Similar in People With Multiple Sclerosis, Their Siblings, and Unrelated Healthy Controls: A Blinded, Case-Control Study," *Can Assoc Radiol J.*

[71] McTaggart RA, Fischbein NJ, Elkins CJ, Hsiao A, Cutalo MJ, Rosenberg J, Dake MD, Zaharchuk G (2012), "Extracranial Venous Drainage Patterns in Patients with Multiple Sclerosis and Healthy Controls," *AJNR Am J Neuroradiol*, Vol. 33, 1615–1620.

[72] NASA website $http://www.nasa.gov/mission_pages/station/research/experiments/1278.html$

[73] Naveen G, Nitish G (2000), "Jugular venous pulse: an appraisal," *J Indian Acad Clin Med*, Vol. 1, pp. 260–269.

[74] Nichols W, O'Rourke M, Vlachopoulos C (2011), "McDonald's blood flow in arteries, sixth edition: theoretical, experimental and clinical principles," *Boca Raton: CRC Press.*

[75] Novario R, Goddi A, Tanzi F, Conte L, Nicolini G (2003), "Physics and technology of medical diagnostic ultrasound," *La Rivista del Nuovo Cimento (2003)*, Vol. 26(2).

[76] Nowak JA, Ocon A, Taneja I, Medow MS, Stewart JM (2009), "Multiresolution wavelet analysis of time-dependent physiological responses in syncopal youths," *Am J Physiol Heart Circ Physiol*, Vol. 296(1), pp. H171–H179.

[77] Olufsen MS, Ottesen JT, Tran HT, Ellwein LM, Lipsitz LA, Novak V (2005), "Blood pressure and blood flow variation during postural change from sitting to standing: model development and validation," *J Appl Physiol (1985)*, Vol. 99(4), pp. 1523–1537.

[78] Patton KT, Thibodeau GA (2011), "Anatomia e Fisiologia," *Elsevier.*

[79] Paulson OB, Strandgaard S, Edvinsson L (1990), "Cerebral autoregulation," *Cerebrovasc Brain Metab Rev*, Vol. 2(2), pp. 161–192.

[80] Peiro J, Veneziani A (2009), "Reduced models of the cardiovascular system," *Cardiovascular Mathematics*, Vol. 1, pp. 347–394.

[81] Peters J, Fraser C, Stuart RS, Baumgartner W, Robotham JL (1989), "Negative intrathoracic pressure decreases independently left ventricular filling and emptying," *Am J Physiol*, Vol. 257(1 Pt 2), pp. H120–H131.

[82] Piechnik SK, Czosnyka M, Harris NG, Minhas PS, Pickard JD (2001), "A model of the cerebral and cerebrospinal fluid circulations to examine asymmetry in cerebrovascular reactivity," *J Cereb Blood Flow Metab*, Vol. 21(2), pp. 182–192.

[83] Potchen EJ, Haacke EM, Siebert JE, Gottschalk A (eds) (1993), "Magnetic resonance angiography Concepts and applications," *St Louis:Mosby Year Book.*

[84] Quarteroni A, Formaggia L (2002), "Mathematical modelling and numerical simulation of the cardiovascular system. In: Modelling of living systems, Handbook of numerical analysis series," *Amsterdam:Elsevier.*

[85] Quarteroni A, Fausto S (2006), "Scientific Computing with MATLAB and Octave," *Springer.*

[86] Radak D, Kolar J, Tanaskovic S, Sagic D, Antonic Z, Mitrasinovic A, Babic S, Nenezic D, Ilijevski N (2012), "Morphological and haemodynamic abnormalities in the jugular veins of patients with multiple sclerosis," *Phlebology*, Vol. 27(4), pp. 168–172.

[87] Reymond P, Merenda F, Perren F, Rfenacht D, Stergiopulos N (2009), "Validation of a one-dimensional model of the systemic arterial tree," *Am J Physiol Heart Circ Physiol*, Vol. 297(1), pp. H208–H222.

[88] Saito M, Ikenaga Y, Matsukawa M, Watanabe Y, Asada T, Lagre PY (2011), "One-dimensional model for propagation of a pressure wave in a model of the human arterial network: comparison of theoretical and experimental results," *J Biomech Eng*, Vol. 133(12), pp. 121005.

[89] San Millan Ruiz D, Gailloud P, Rfenacht DA, Delavelle J, Henry F, Fasel JH (2002), "The craniocervical venous system in relation to cerebral venous drainage," *AJNR Am J Neuroradiol*, Vol. 23(9), pp. 1500–1508.

[90] Schaller B (2004), "Physiology of cerebral venous blood flow: from experimental data in animals to normal function in humans," *Brain Res Brain Res Rev*, Vol. 46(3), pp. 243–260.

[91] Schreiber SJ, Lurtzing F, Gotze R, Doepp F, Klingebiel R, Valdueza JM (1985), "Extrajugular pathways of human cerebral venous blood drainage assessed by duplex ultrasound," *J Appl Physiol*, Vol. 94(5), pp. 1802–1805.

[92] Sethi SK, Utriainen DT, Daugherty AM, Feng W, Hewett JJ, Raz N, Haacke EM (2015), "Jugular Venous Flow Abnormalities in Multiple Sclerosis Patients Compared to Normal Controls," *J Neuroimaging*, Vol. 25(4), pp. 600–607.

[93] Sethi SK, Daugherty AM, Gadda G, Utriainen DT, Jiang J, Raz N, Haacke EM (2017), "Jugular Anomalies in Multiple Sclerosis are Associated with Increased Collateral Venous Flow," submitted to *AJNR Am J Neuroradiol*.

[94] Sherwin SJ, Franke V, Peiro J, Parker K (2003), "One-dimensional modelling of a vascular network in space-time variables," *J Eng Maths*, Vol. 47, pp. 217–250.

[95] Shoeb A, Clifford G (2005), "Biomedical signal and image processing, cap. 16: Wavelets; multiscale activity in physiological signals," *Spring*.

[96] Sifuzzaman M, Islam MR, Ali MZ (2009), "Application of wavelet transform and its advantages compared to Fourier transform," *J Phys Sci*, Vol. 13, pp. 121–134.

[97] Singh AV, Zamboni P (2009), "Anomalous venous blood flow and iron deposition in multiple sclerosis," *J Cereb Blood Flow Metab*, Vol. 29(12), pp. 1867–1878.

[98] Sisini F, Tessari M, Gadda G, Di Domenico G, Taibi A, Menegatti E, Gambaccini M, Zamboni P (2015), "An ultrasonographic technique to assess the jugular venous pulse: a proof of concept," *Ultrasound Med Biol*, Vol. 41(5), pp. 1334–1341.

[99] Smith NP, Pullan AJ, Hunter PJ (2002), "An anatomically based model of transient coronary blood flow in the heart," *Society for Industrial and Applied Mathematics*, Vol. 62(3), pp. 990–1018.

[100] Sorek S, Bear J, Karni Z (1989), "Resistances and compliances of a compartmental model of the cerebrovascular system," *Ann Biomed Eng*, Vol. 17(1), pp. 1–12.

[101] Steele BN, Taylor CA (2003), "Simulation of blood flow in the abdominal aorta at rest and during exercise using a 1-D finite element method with impedance boundary conditions derived from a fractal tree," *Summer Bioengineering Conference*.

[102] Steele BN, Olufsen MS, Taylor CA (2007), "Computer simulation of arterial flow with applications to arterial and aortic stenoses," *J Biomech*, Vol. 25(12), pp. 1477–1488.

[103] Stergiopulos N, Young DF, Rogge TR (1992), "Computer simulation of arterial flow with applications to arterial and aortic stenoses," *J Biomech*, Vol. 25(12), pp. 1477–1488.

[104] Tamura T (2014), "Comprehensive biomedical physics," *Amsterdam:Elsevier*.

[105] Thibault P, Lewis W, Niblett S (2015), "Objective duplex ultrasound evaluation of the extracranial circulation in multiple sclerosis patients undergoing venoplasty of internal jugular vein stenoses: a pilot study," *Phlebology*, Vol. 30(2), pp. 98–104.

[106] Torres C, Hogan M, Patro S, Chakraborty S, Nguyen T, Thornhill R, Freedman M, Bussiere M, Dabirzadeh H, Schwarz BA, Belanger S, Legault-Kingstone L, Schweitzer M, Lum C (2016), "Extracranial Venous abnormalities: A true pathological finding in patients with multiple sclerosis or an anatomical variant?," *Eur Radiol*, Vol. 27(1), pp. 239–246.

[107] Traboulsee AL, Knox KB, Machan L, Zhao Y, Yee I, Rauscher A, Klass D, Szkup P, Otani R, Kopriva D, Lala S, Li DK, Sadovnick D (2014), "Prevalence of extracranial venous narrowing on catheter venography in people with multiple sclerosis, their siblings, and unrelated healthy controls: a blinded, case-control study," *Lancet*, Vol. 383(9912), pp. 138–145.

[108] Ursino M, Lodi CA (1997), "A simple mathematical model of the interaction between intracranial pressure and cerebral hemodynamics," *J Appl Physiol (1985)*, Vol. 82(4), pp. 1256–1269.

[109] Ursino M, Magosso E (2000), "Acute cardiovascular response to isocapnic hypoxia. I. A mathematical model," *Am J Physiol Heart Circ Physiol*, Vol. 279(1), pp. H149–H165.

[110] Ursino M, Ter Minassian A, Lodi CA, Beydon L (2000), "Cerebral hemodynamics during arterial and CO(2) pressure changes: in vivo prediction by a mathematical model," *Am J Physiol Heart Circ Physiol*, Vol. 279(5), pp. H2439–H2455.

[111] Valdueza JM, von Mnster T, Hoffman O, Schreiber S, Einhupl KM (2000), "Postural dependency of the cerebral venous outflow," *Lancet*, Vol. 355(9199), pp. 200–201.

[112] van de Vosse FN, Stergiopulos N (2011), "Pulse wave propagation in the arterial tree," *Annu Rev Fluid Mech*, Vol. 43, pp. 467–499.

[113] Veroux P, Giaquinta A, Perricone D, Lupo L, Gentile F, Virgilio C, Carbonaro A, De Pasquale C, Veroux M (2013), "Internal jugular veins out flow in patients with multiple sclerosis:a catheter venography study," *J Vasc Interv Radiol*, Vol. 24(12), pp. 1790–1797.

[114] Waite L (2006), "Biofluid mechanics in cardiovascular systems," *New York:McGraw-Hill*.

[115] Wang JJ, Parker KH (2004), "Wave propagation in a model of the arterial circulation," *J Biomech*, Vol. 37(4), pp. 457–470.

[116] Werner JD, Siskin GP, Mandato K, Englander M, Herr A (2011), "Review of venous anatomy for venographic interpretation in chronic cerebrospinal venous insufficiency," *J Vasc Interv Radiol*, Vol. 22(12), pp. 1681–1690.

[117] Zaharchuk G, Fischbein NJ, Rosenberg J, Herfkens RJ, Dake MD (2011), "Comparison of MR and Contrast Venography of the Cervical Venous System in Multiple Sclerosis," *AJNR Am J Neuroradiol*, Vol. 32, pp. 1482–1489.

[118] Zamboni P (2006), "The Big Idea: Iron-dependent inflammation in venous disease and proposed parallels in multiple sclerosis," *J R Soc Med*, Vol. 99(11), pp. 589–593.

[119] Zamboni P, Consorti G, Galeotti R, Gianesini S, Menegatti E, Tacconi G, Carinci F (2009), "Venous collateral circulation of the extracranial cerebrospinal outflow routes," *Curr Neurovasc Res*, Vol. 6(3), pp. 204–212.

[120] Zamboni P, Galeotti R, Menegatti E, Malagoni AM, Tacconi G, DallAra S, Bartolomei I, Salvi F (2009), "Chronic cerebrospinal venous insufficiency in patients with multiple sclerosis," *J Neurol Neurosurg Psychiatry*, Vol. 80, pp. 392–399.

[121] Zamboni P, Galeotti R (2010), "The chronic cerebrospinal venous insufficiency syndrome," *Phlebology*, Vol. 25(6), pp. 269–279.

[122] Zamboni P, Menegatti E, Weinstock-Guttman B, Schirda C, Cox JL, Malagoni AM, Hojnacki D, Kennedy C, Carl E, Dwyer MG, Bergsland N, Galeotti R, Hussein S, Bartolomei I, Salvi F, Ramanathan M, Zivadinov R (2010), "CSF dynamics and brain volume in multiple sclerosis are associated with extracranial venous flow anomalies: a pilot study," *Int Angiol*, Vol. 29(2), pp. 140–148.

[123] Zamboni P, Morovic S, Menegatti E, Viselner G, Nicolaides AN (2011), "Screening for chronic cerebrospinal venous insufficiency (CCSVI) using ultrasound–recommendations for a protocol," *Int Angiol*, Vol. 30(6), pp. 571–597.

[124] Zamboni P, Menegatti E, Conforti P, Shepherd S, Tessari M, Beggs C (2012), "Assessment of cerebral venous return by a novel plethysmography method," *J Vasc Surg*, Vol. 56(3), pp. 677–685.

[125] Zamboni P, Menegatti E, Pomidori L, Morovic S, Taibi A, Malagoni AM, Cogo AL, Gambaccini M (2012), "Does thoracic pump influence the cerebral venous return?," *J Appl Physiol*, Vol. 112(5), pp. 904–910.

[126] Zamboni P, Menegatti E, Occhionorelli S, Salvi F (2013), "The controversy on chronic cerebrospinal venous insufficiency," *Veins and Lymphatics*, Vol. 2(2).

[127] Zamboni P, Sisini F, Menegatti E, Taibi A, Malagoni AM, Morovic S, Gambaccini M (2013), "An ultrasound model to calculate the brain blood outflow through collateral vessels: a pilot study," *BMC Neurol*, Vol. 13(81).

[128] Zaniewski M, Simka M (2012), "Biophysics of venous return from the brain from the perspective of the pathophysiology of chronic cerebrospinal venous insufficiency," *Rev Recent Clin Trials*, Vol. 7(2) pp. 88–92.

[129] Zivadinov R, Galeotti R, Hojnacki D, Menegatti E, Dwyer MG, Schirda C, Malagoni AM, Marr K, Kennedy C, Bartolomei I, Magnano C, Salvi F, Weinstock-Guttman B, Zamboni P (2011), Value of MR Venography for Detection of Internal Jugular Vein Anomalies in Multiple Sclerosis: A Pilot Longitudinal Study"," *AJNR Am J Neuroradiol*, Vol. 32 pp. 938–946.

[130] Zivadinov R, Lopez-Soriano A, Weinstock-Guttman B, Schirda CV, Magnano CR, Dolic K, Kennedy CL, Brooks CL, Reuther JA, Hunt K, Andrews M, Dwyer MG, Hojnacki DW (2011), "Use of MR venography for characterization of the extracranial venous system in patients with multiple sclerosis and healthy control subjects," *Radiology*, Vol. 258(2) pp. 562–570.

[131] Zivadinov R, Chung CP (2013), "Potential involvement of the extracranial venous system in central nervous system disorders and aging," *BMC Med*, Vol. 11(260).

[132] Zivadinov R, Bastianello S, Dake MD, Ferral H, Haacke EM, Haskal ZJ, Hubbard D, Liasis N, Mandato K, Sclafani S, Siddiqui AH, Simka M, Zamboni P; International Society for Neurovascular Disease (2014), "Recommendations for multimodal noninvasive and invasive screening for detection of extracranial venous abnormalities indicative of chronic cerebrospinal venous insufficiency: a position statement of the International Society for Neurovascular Disease.," *J Vasc Interv Radiol*, Vol. 25(11) pp. 1785–1794.

[133] The Magnetic Resonance Institute for Biomedical Reasearch. http://www.mrimaging.com/category.103.html. Accessed January 11, 2016.

[134] The MathWorks Inc. https://it.mathworks.com/products/matlab.html. Accessed December 28, 2016.

Ringraziamenti

Grazie a tutti quelli che in tanti anni hanno condiviso con me la vita in Dipartimento. Ferrara è un'isola meravigliosa, sono felice ed orgoglioso di farne parte. Grazie soprattutto al Prof. Angelo Taibi, al Prof. Mauro Gambaccini, e a tutto il gruppo di Fisica Medica, un microcosmo a cui sono grato ogni giorno per le opportunità, la fiducia, e le responsabilità che mi sta dando. Cercherò di essere sempre all'altezza.
A Francesca del duo comico "GiacomoFrancesca" (non piangere), e a Sara, Marco, Valentina, Adriano, Simona, Giovanni, Micael, Nicola, Gaia, Paolo, Elisabetta e Simone, tutti indimenticabili per mille motivi diversi.
A tutto il gruppo FSF (per me esserci è un orgoglio esagerato), in particolar modo a Susanna, per la sua mail da oltreoceano, la cravattona a pallini, e l'avermi fatto capire cosa sono in grado di fare.
Grazie ad Antonella, Gianni e Federico, che mi supportano (e mi sopportano) sempre.
Grazie alla famiglia Partiti, nella sua versione allargata che comprende pizzaiole, wookiee, piloti del Tourist Trophy, fiorai (che vendono fiori di prosciutto), e un sacco di altra umanità. Posso stare lontano mesi, ma vi ritrovo sempre.
Grazie a Cin per le mani e per gli occhi, a Larvino per il rumore, a Fiaba per il silenzio, a Kalmo per il weekend più bello della mia vita, a Lo Hacker per la pasta, a Serafino per le foto, a Braciola per gli aneddoti, a Logica per il mare, a Sommo per i disegni, a J per la risata, a Coccola per gli abbracci, a Tenerina per il naso nello smirr. Vi voglio un bene dell'anima.